Università degli Studi di Milano
Facoltà di Scienze Matematiche, Fisiche e Naturali
Dipartimento di Scienze della Terra "*Ardito Desio*"

Scuola di Dottorato "*Terra, Ambiente e Biodiversità*"
Dottorato di Ricerca in Scienze della Terra - Ciclo XXV

Sanitary-ware: from the industrial macro characterization to the atomic scale analysis

Tesi di dottorato

Andrea Bernasconi

N. Matricola R08692

Dott.ssa Monica Dapiaggi
Tutor
Prof. Alessandro Pavese
Co-Tutor

Anno Accademico
2011-2012

Prof.ssa Elisabetta Erba
Coordinatore

To my family

Contents

Research Aim

Sanitary-ware products are one of the most diffused ceramic materials which can be found as bathroom furniture in every building. They are formed by two distinct parts: the ceramic body and the covering material (glaze), fired together at about 1200°C in order to develop the phase reactions which finally fix the mineralogical composition, the microstructure and consequently, the technical and aestethical properties of the material. In the present thesis, a wide exploration of these materials will be presented: it starts from a wide characterization of industrial interest (Part I) and goes deeper and deeper to the atomic scale analysis (Part III), passing through the study of the parameters which can affect the accuracy in glaze quantitative phase analysis (Part II).

1. Part I is aimed at the evaluation of the influence of compositional and procedural parameters on the evolution of ceramic body and glaze. So, different grids of samples were prepared within typical industrial ranges to highlight differences, if present, by means of some conventional industrial measurements (i.e. Water Absorption, Dilatometry, Hot Stage Microscope) and other more detailed techniques (X-ray Powder Diffraction, Scanning Electron Microscope and also Synchrotron X-ray Tomography). In Chapter 1, the effects of firing time and temperature, and of particle size have been observed on the glass phase formation and on the some technological properties like the porosity and the thermal expansion, which may affect, in turn, the quality of the product. On the other hand, in Chapter 2, glaze, which is a quite different from the ceramic body, was studied by varying its composition in order to look at its behavior during and after the firing process because adhesion on the ceramic support is required. Moreover, some effective tools have been defined to characterize glaze microstructure, especially by means of Synchrotron X-ray Tomography.

2. Part II looks at the methodological parameters which may affect the quantification of the main crystalline phase within glaze (i.e. zircon), in case of large amorphous content, with X-ray Powder Diffraction technique. The presence of abundant glass phase comes from the typical composition of sanitary-glaze and may be problematic if an accurate quantitative phase analysis is looked for. Different internal standard, corrections, data treatment and sample preparation procedures were used in order to find the protocol that provides the most accurate results on artificial samples of known composition. Furthermore, some Scanning Electron Microscope images and Laser Scattering measurements were carried out as complementary data to clarify some aspects inaccessible to X-ray Powder Diffraction.

3. Part III moves the attention to the atomic scale of the sanitary-ware, in particular to the amorphous part of sanitary-glaze, which strongly model some technological properties of the material (i.e. glass transition temperature). To access the structure of the amorphous material, total scattering is one of the most accurate techniques; thus, three significatively different glasses were prepared and collected by coupling neutron and X-ray total scattering. Data modeling was performed to get the structural model and consequently to extract some interesting information like the distances between atom pairs, their coordination number and bond angles, and also the type of oxygen sharing.

Part I

Sanitary-ware production: influence of firing process and composition

Ceramic can be defined as an inorganic material that results from a firing process which confers it rigidity and aestethical properties. A high temperature process is essential and links all kind of ceramic materials whilst other parameters, like peak temperature and raw materials, are characteristic of the different ceramic products and of their final applications. This is well known to production companies which always monitor firing apparatus state and the composition and particle size of raw materials, and which encourage the research of new conditions to improve ceramic properties and/or to abate production costs, recently also using waste materials. Sanitary-ware materials are an example of ceramic materials which are characterized by cohexistence between a rigid body and a covering material. Their production involves different steps: from the appropriate mixing of raw materials to the firing (and cooling) process. A slip is initially prepared by mixing water, different raw materials (i.e. clay minerals, feldspars and quartz) and deflocculating agents. When the desired viscosity and thixotropy properties are achieved, the slip is ready to be casted into a porous mold. Slip particles adhere to the walls and the water is gradually removed through the pores, then the resultant shape, called "green body", can be easily removed from the mold due to a slight shrinkage. Water is still present in the body and an additional drying step is required; it can be achieved, for example, by properly recycle part of the furnace heat. At this point, a suspension (the raw glaze) can be manually or automatically applied upon the product and left to dry and to adhere on it. Firing process is the last step in the industrial practice and it is the most important, and delicate, of all; in general, for sanitary-ware production, peak temperature lies between 1150 and 1250°C. Substantially, in this step, raw materials react producing a sintered and densified object while the raw glaze melts; in this way, the technological and aestethical properties are finally conferred to the manufact.

Chapter 1

Sanitary-ware vitreous body

1.1 Introduction

Sanitary-ware vitreous bodies belong to the wider category "China" whiteware that are defined as "glazed or unglazed vitreous ceramic whiteware made by the china process, and used for nontechnical purposes, designating such products as dinnerware, sanitaryware, and artware when they are vitreous", following the traditional scheme [Carty & Senapati, 1998]. Like the other whiteware products (porcelain, stoneware, earthenware), "China" are commonly "white and of fine texture, formed from natural raw materials with a dominant portion of clay" [American Society for testing materials]. In general, they are obtained from three ingredients (a clay, a filler and a flux) and for this reason are commonly named "triaxial porcelain".

Clays, containing minerals such as kaolinite, smectite and illite, provide plasticity to the green body during the formation procedure. Their plately morphology and their high specific surface area (18-30 $\frac{m^2}{g}$) are responsible of this effect, favored by the correct amount of water. In the industrial practice, a mix of different clay minerals is adopted; the two most common groups are kaolin and ball clay. They are formed by a dominant kaolinite fraction with lower amount of smectite, montmorillonite, illite and also quartz; in general, ball clays contain an higher level of quartz impurities and also organic matter.

Fillers, such as quartz, are generally the coarsest particles in the green body; they are (partially) still present after the firing process and, therefore, the final product is strongly influenced by their nature and volume fraction. In sanitary-ware body, quartz sustains the ceramic body, but great attention must be paid to the possible deterioration of mechanical properties (microcrack, shrinkage) during cooling process at 573°C, in correspondence to the displacive β-α quartz transition.

Fluxes are substances which promote the fusion of raw materials upon heating. Feldspars are the most adopted fluxes: they are commonly introduced as a mix of different feldspars (albite and microcline); the typology of adopted feldspar influences the resultant eutectic temperature of raw "China" mixture [Reifenstein et al., 1999].

The typical compositions for manufacturing sanitary-ware products (SiO_2-Al_2O_3-K_2O ternary system) are shown in Figure 1.1. In the industrial practice, such compositions are obtained with a 2:1:1 ratio between clays (50 wt.% kaolin, 50 wt.% ball clay), fluxes (feldspar) and filler (quartz). Some modification can be present depending on impurities within clays and feldspars.

Once raw materials have been selected, they have to be mixed in humid condition with the addition of additive to adjust viscosity and control the formation of agglomerates. This process is influenced by interaction between particles, particle concentration, particle morphology and particle size distribution [Bergstrom, 1994].

Subsequently, once the desired rheology is obtained, the suspension is ready to be casted by means of filter

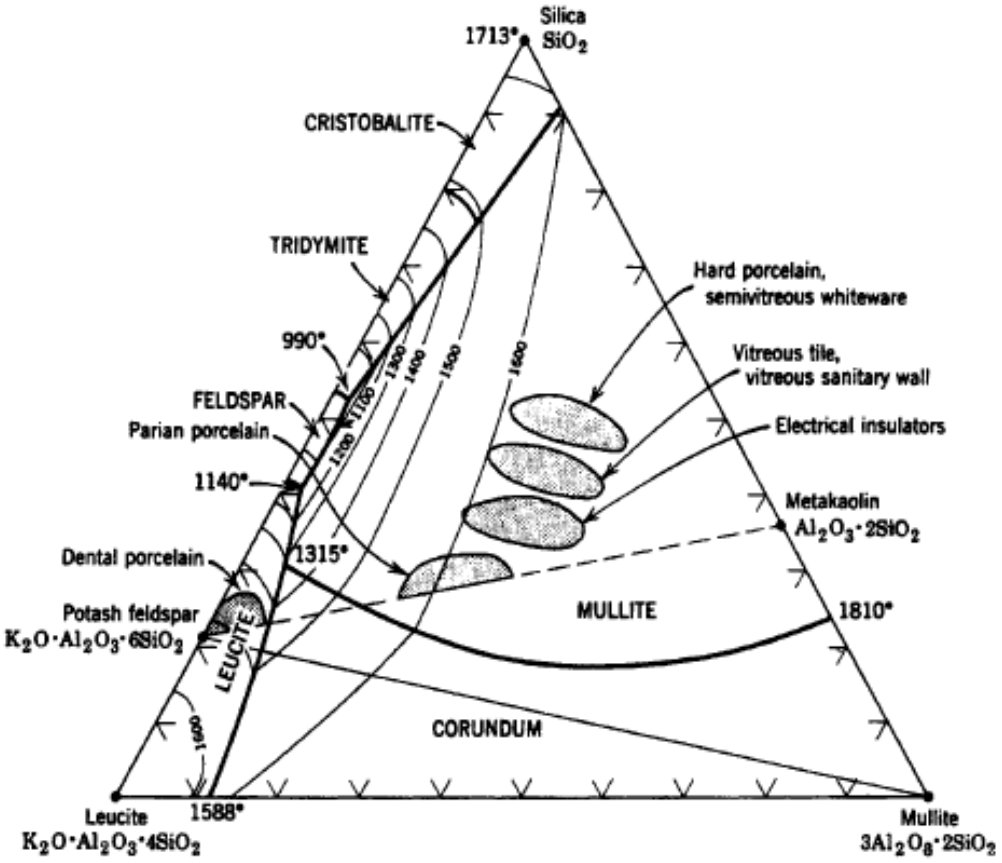

Figure 1.1: Portion of the SiO_2-Al_2O_3-K_2O phase diagram. Potash feldspar incongruently melts at 990℃ . Figure was taken from [Carty & Senapati, 1998].

press procedure [Aksay & Schilling, 1984], dried and finally processed at high temperature. In general, firing temperature ranges from 1150 to 1280°C even if peak temperature is selected considering other parameters, such as firing time, heating rate, green body composition and particle size. The first reaction upon heating concerns kaolinite that transforms into metakaolinite at about 450-600°C after dehydroxylation reaction [Brindley & Nakahira, 1959; Gualtieri & Bellotto, 1998]. In this interval, α-β quartz transition happens at 573°C without relevant consequence on the structure. In the 500-800°C range microcline and albite go into sanidine and high-albite, respectively [Brown & Parsons, 1989]. At about 950°C, a cubic spinel-type phase forms from metakaolinite with liberation of silica [Brindley & Nakahira, 1959], followed by crystallization of primary mullite. Feldspar starts melting in the range 990-1050°C depending on the type of feldspar and gives rise to interaction between the whiteware components: a glassy phase starts to bind crystals together and secondary mullite forms from clay relicts and liquid phase. Quartz is prevalently inert to these process but it partially dissolves from 1000°C until melt becomes saturated in silica. At the same time, mullite continues to form until about 1250°C [Martin-Marquez et al., 2009]. Cristobalite formation may occur when quartz dissolution is stopped. When cooling starts, the different shrinkage behavior of glass, quartz, mullite and cristobalite (if present) may produce some residual stress and therefore cracking phenomena. These problem, may be emphasized when the β forms of quartz and cristobalite (if present) invert into α form at about 573 and about 250°C, respectively, due to the large volumetric change. Things are more complex if a glaze is present upon the sanitary-ware body because its shrinkage must be comparable with the behavior of the sanitary-ware vitreous body.

In the last decade, many papers aimed at the characterization of whiteware have been published, highlighting the interest surrounding these materials. In 2004, G.Stathis et al. prepared sanitary-ware porcelain with different starting quartz amount and particle size, firing time and temperature: the role of quartz particle size resulted very important in residual quartz amount, open and total porosity and bending strength. Best properties were achieved for the 5-20 μm quartz particle size: a coarser particle size produces a very porous microstructure with consequent loss of mechanical properties, while, on the opposite, a finer particle size results in a low bending strength due to limited pre-stressing effect. Studies like the one of Sthatis et al. are very important because they give way to optimization of sintering procedure in order to save part of firing energy by grinding raw materials. From 2005 to 2008, T.Tarvornpanich et al. published three different papers in which the introduction of a silica-lime-soda waste glass was (partially) introduced as flux, providing better technological properties (water absorption and bulk density, overall) at lower firing temperatures, if compared with the traditional commercial formulation. With this formulation, a wider variety of crystalline phases have been detected (i.e. plagioclase, wollastonite, cristobalite) favored by the relevant amounts of sodium and calcium from the silica-lime-soda glass portion. These study are important because they lead to a cost reduction of the firing process, due to a lower the firing temperature. Additionally, a further cost reduction is given by the lower cost of these waste glasses compared with the one of the common fluxes (feldspar, nepheline syenite). In 2009, J.Martin-Marquez et al. studied the evolution of a triaxial porcelain tile (50 wt.% clay, 40wt. % feldspar, 10 wt.% quartz) at 45°C/min heating rate by means of X-ray powder diffraction and Scanning Electron Microscope. The resultant reaction temperatures are moved to higher values because of the higher heating rate: quartz starts to dissolve at 1230°C without transforming into cristobalite, mullite is first detected above 1000°C and is present up to 1230°C , amorphous phase continuously increases up to 1400°C.

This part of the present thesis is aimed at understanding the effects of peak firing temperatures (T_f), firing time (t_f) and quartz particle size (d_{50}) on the evolution of phases and on some technological properties in an ordinary sanitary-ware mixture (50 wt.% clay, 25 wt.% quartz and 25 wt.% feldspar). This intent was achieved by performing X-ray Powder Diffraction (for phase qualitative and quantitative analysis), Scanning Electron Microscope (for microstructural investigation), water absorption (for interconnected porosity) and thermal expansion (to evaluate product behavior upon cooling) measurements.

1.2 Experimental Procedure

1.2.1 Samples

Two bulk commercial mixtures have been prepared. They are identical in raw material composition (27 wt.% kaolin, 23 wt.% ball clay, 25 wt.% quartz and 25 wt.% feldspar) and different in quartz particle size (d_{50}): it is 50 μm for series S1 and 18 μm for series S2. The chemical composition of raw materials is shown in Table 1.1; therefore, the resultant bulk chemical composition is: SiO_2 70.12 wt.%, Al_2O_3 25.00 wt.%, Fe_2O_3 0.65 wt.%, MgO 0.17 wt.%, TiO_2 0.27 wt.%, CaO 0.13 wt.%, K_2O 1.05 wt.% and Na_2O 2.62 wt.%. Both mixtures were mixed in wet condition within a flunger, aged for 24 hours and then casted into cylinders with a diameter of 0.8 cm and length of 6 cm. Each cylinder has been treated in a static kiln combining three firing temperature T_f (1200, 1240 and 1280°C) and five firing time t_f (0, 20, 40, 60 and 80 min) maintaining a heating rate of 10°C/min. Thus, a total of 30 samples have been prepared.

wt.%	Raw material	SiO_2	Al_2O_3	Fe_2O_3	MgO	TiO_2	CaO	K_2O	Na_2O
27	Kaolin	54.24	41.81	1.07	0.33	0.05	0.08	2.26	0.16
23	Ball clay	55.65	39.52	1.37	0.23	1.04	0.23	1.73	0.23
25	Quartz	99.42	0.4	0.05	0	0	0.02	0.05	0.06
25	Feldspar	71.29	18.07	0.13	0.1	0.06	0.2	0.1	10.05

Table 1.1: Elemental composition of the raw materials used for the initial slip composition. Data have been provided by supplier (Sibelco, UK) with a declared average uncertainly of about 0.5%.

1.2.2 Water Absorption

The water absorption coefficient (WA) was determined using the following procedure:

1. the sample was dried for 12 hours at 110°C and its weight (m_d) was measured using an analytical balance;
2. the sample was then immersed in water and boiled for 2 hours, cooled in situ for 12 hours and re-weighed (m_w);
3. the water absorption (W.A.) calculated following the Equation 1.1;

$$W.A. = \frac{m_w - m_d}{m_d} \times 10, \tag{1.1}$$

This parameter is commonly adopted in the industrial practice to quantify the degree of porosity, and assesses whether the finished sanitary-ware bodies meet the technical requirements. In general, the maximum limit value is fixed at 0.5.

1.2.3 Dilatometric Test

Dilatation measurements were carried out using a Netzsch Dilatometer 402 ED, located at the Ideal Standard laboratory in Trichiana (Italy). The instrument was previously calibrated on α-alumina and tested for industrial sanitary-ware samples, setting the temperature ramp rate at 5.5°C/min. The sample length was recorded every 0.1 min, between 20 and 815°C. A relationship between the thermal expansion coefficient (α_L) and the sample length at temperature T, i.e. L(T), is present, following the Equation 1.2

$$L(T) = L_0 exp[\alpha_L (T - T_0)] \tag{1.2}$$

where the subscript 0 indicates ambient conditions; (α_L) is here modeled by a constant term. The volume (V) thermal expansion coefficient (α) of bodies constituted of more than one phase (a subscript *j* is hereafter used to attribute a given quantity to the *j*-th phase) can be expressed as Equation 1.3:

$$\alpha = \frac{1}{V} \times \frac{\partial V}{\partial T} \tag{1.3}$$

Finally, Equation 1.3 can be casted into Equation 1.4:

$$\alpha = \frac{[\Sigma_j \lambda_j \times (\frac{\alpha_j}{\rho_j})]}{\sum_j (\frac{\lambda_j}{\rho_j})} \tag{1.4}$$

where λ_j and ρ_j are the weight fraction and density of the *j*th-phase, respectively. For all phases, the values of λ_j, ρ_j and α_j at room conditions were used, which provide an excellent approximation for the present case. However, in the case of quartz, for the volume thermal expansion coefficient was considered its average value on the 25-550°C T-range. Note that: (i) in isotropic bodies the relationship between linear and volume thermal expansion coefficients is $\alpha \approx 3 \times \alpha_L$ (ii) the model of Equation 1.3 neglects the effects due to the contact surfaces between phases; (iii) $\rho_{glass} \approx 2.07$ g/cm^3 , as used here, is an estimation resulting from an average based on over 50 pycnometer density measurements of ceramic bodies, where the raw ρ-values had been properly corrected to account for the embedded crystal phases.

1.2.4 X-ray Powder Diffraction

X-ray powder diffraction is one of the most powerful techniques to carry out phase qualitative and quantitative analyses. Fired samples have been ground in agate mortar and then analyzed with an X'Pert PRO PANalytical diffractometer working in θ-2θ Bragg-Brentano geometry and equipped with an X'Celeretor detector. Copper radiation has been adopted to investigate the 2θ range from 10 to 80° with a step size of 0.02° and a counting time of 30 s. Sanitary-ware vitrous bodies contain a significative amount of glass, so spiking with an internal standard was required to apply RIR-RIETVELD method [Gualtieri, 2000], with GSAS program and EXPGUI graphical interface [Larson & Von Dreele, 2004; Toby, 2001]. A calcined α alumina (adopted structure during refinement is ICSD 51687, [Toebbens et al., 2001]) was added in fixed amount (20 wt.%) to each sample. Twelve coefficients were used to describe the background with a Chebyshev polynomial series; then, for each phase, the relative scale factor, cell parameters and profile width parameters using a pseudo-Voigt functions were refined. Quartz amount was also determined with traditional Reference Intensity Ratio method [Chung, 1974] in order to cross-check these latter results with the results obtained with RIR-RIETVELD method. More details about this approach are shown in Chapter 3 of the present thesis.

1.2.5 Scanning Electron Microscopy

All samples were analyzed using a Cambridge Stereoscan 360 scanning electron microscope to investigate their phase-morphology and micro-structural features, and to discriminate between primary and secondary mullite crys-

tals. The cylinders were cut transversally into 5mm thick slices with a water-lubricated rock saw. Discrimination between primary and secondary mullite requires removal of as much of the glassy matrix embedding the crystals as possible. This was accomplished by etching the samples surface by means of fluoro-boric acid for 6 hours, which is an effective method for dissolving part of the glassy matrix, allowing an improved view of the crystals trapped inside.

1.3 Results and Discussion

1.3.1 Phase evolution with firing time, firing temperature and quartz particle size

Preliminary qualitative analysis highlighted the presence of quartz (structure was taken from ICSD 67117, [Dubrovinskii et al., 1989]) for structure), mullite (ICSD 100805, [Saalfeld et al., 1981]) and glass in all the investigated samples; the presence of Na-feldspar (ICSD 26248, [Ribbe et al., 1969]), even if in small amount, was detected in samples fired for short time. Kaolinite and the others clay mineral are fully decomposed during the heating ramp, in agreement with literature [Carty & Senapati, 1998]. All the results are summarized in the Appendix (Table 5.1). Rietveld refinements provided a good fit between measured and calculated diffraction patter as shown in Figure 1.2, whose fitted R_{wp}, R_p, reduced χ^2 and R_{F^2} were 0.078, 0.056, 2.678 and 0.205, respectively. Note that, in both series, each sample has been collected twice in order to check the reproducibility of the data: the standard deviations (between the two different QPA results with Rietveld refinement) ranges from 0.1 to 0.5.

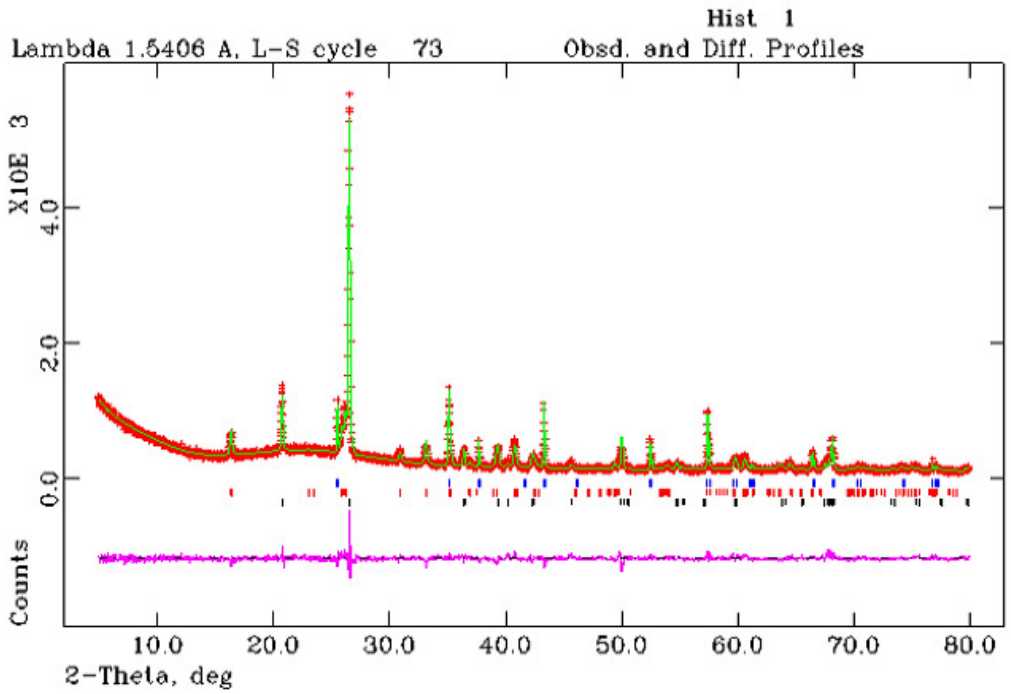

Figure 1.2: Rietveld plot for composition S1 fired at 1240℃ for 80 min.

The evolution of quartz, glass and mullite with t_f at different T_f are represented in Figure 1.3. Residual quartz ranges from 28.6 to 13.0 wt.% if RIR-Rietveld method is used, and from 31.1 to 14.6 wt.% if traditional RIR method is used. For traditional RIR method, according with [Chung, 1974], the RIR_{qtz} coefficient was previously obtained from a binary mixture of quartz-calcined α-alumina (1:1 ratio) and it was 3.97. In both series, a well defined decreasing trend is evident for quartz if t_f is increased (for all T_f). Also the effect of temperature can be observed: if t_f and quartz d_{50} are fixed, the sample fired at 1280°C has less quartz than samples fired at 1240°C , which in turn has less quartz than the sample fired at 1200°C. Differences in quartz reactivity are proven by the comparison of black and white circles in Figure 1.3: higher residual amounts of quartz are present in samples belonging to series S1 because their reactivity is lower than samples belonging to series S2 [Martin-Marquez et al., 2009; Yqbal & Lee, 2000]. In discussing the behavior and role of SiO_2 in the materials on study,

	$\varphi_{full,S1}$	$\varphi_{0-40,S1}$	$\varphi_{40-80,S1}$	$\varphi_{full,S2}$	$\varphi_{0-40,S2}$	$\varphi_{40-80,S2}$
Quartz						
1200°C	-0.04	-0.03	-0.04	-0.11	-0.12	-0.11
1240°C	-0.08	-0.12	-0.05	-0.11	-0.15	-0.09
1280°C	-0.07	-0.05	-0.07	-0.11	-0.19	-0.03
Glass						
1200°C	0.12	0.17	0.06	0.19	0.22	0.18
1240°C	0.09	0.17	0.01	0.15	0.24	0.10
1280°C	0.07	0.04	0.07	0.13	0.22	0.04
Mullite						
1200°C	0.02	0.07	-0.01	0.01	0.05	-0.03
1240°C	0.03	0.03	0.04	0.00	-0.01	0.00
1280°C	0.00	0.01	0.00	-0.02	-0.04	-0.01

Table 1.2: Full (0-80 min) and partial (0-40 and 40-80 min) slopes of phases as function of t_f at the three different T_f. Slopes have been calculated for both series.

it is important to take into account that the complex silica phase diagram as a function of temperature depends both on the heating/cooling rate of the thermal treatment [Ackermann & Sorrell, 1974] and on the parent slip's phase composition. Trydimite was not observed; although thermodynamically favored, its formation is kinetically impeded except in the presence of specific promoters [Tarvornpanich et al., 2008c]. Similarly, cristobalite, forms in situ at even lower T_fs starting from pure glass precursors, but fails to survive cooling [Moroz et al., 1980; Tarvornpanich et al., 2008; Carty & Senapati, 1998].

Glass is promoted during firing process and its amount ranges from about 46 wt.% to more than 70 wt.%. If compared with quartz, glass has an opposite trend: its formation is clearly promoted by increasing T_f and t_f and also by the finest quartz d_{50}.

Mullite content ranges from about 14 wt.% to 19.5 wt.%. It is interesting to observe that both samples fired at 1200°C for 0 min have the lowest amounts of mullite (about 14 wt.%) respect all the others; at the same time, both samples show the highest amount of residual Na-feldspar. This evidence show that, up to 1200°C , the formation of mullite is strongly connected to the feldspar presence [Lee et al., 2008; Martin-Marquez et al., 2010]. In fact, all the other samples, exhibit very small or absent amount of feldspar and constant amount of mullite (16.5-19.5 wt.%).

Moreover, different rates of phase evolution have been underlined by considering full slopes (φ_{full}, from 0 to 80 min) and partial slopes ($\varphi_{partial}$, from 0 to 40 and from 40 to 80 min) for quartz, glass and mullite contents; the results are summarized in Table 1.2. First of all, the higher reactivity of sample with finest quartz particle size (S2 series) is emphasized by the φ_{full} values of quartz and glass: such values are higher, for all T_f, if compared with the values of the samples with the coarsest quartz particle size (S1 series). Again, the comparison between quartz $\varphi_{partial}$ show comparable values in the case of S1 series, highlighting a quasi-homogeneous evolution of quartz amount during the whole explored interval. In series S2, this trend is different because higher $\varphi_{partial}$ values have been obtained in the first 40 min of treatment; such decreasing trends of quartz dissolution can be explained by the attaintment of a quasi-saturation of silica within the melt. Likewise, the evolution of glass is faster in series S2 than in series S1 as proven by the higher φ_{full} values, for all T_f. In the case of $\varphi_{partial}$, both series show higher values in the 0-40 min range even if the glass formation is still evident in the last 40 min. Finally, as expected from Figure 1.3, mullite φ_{full} are close to zero, due to the constant value of this phase in the explored firing conditions. However, at 1200°C , mullite φ_{0-40} values of 0.07 and 0.05 remark what previously mentioned about the formation of mullite from residual feldspar.

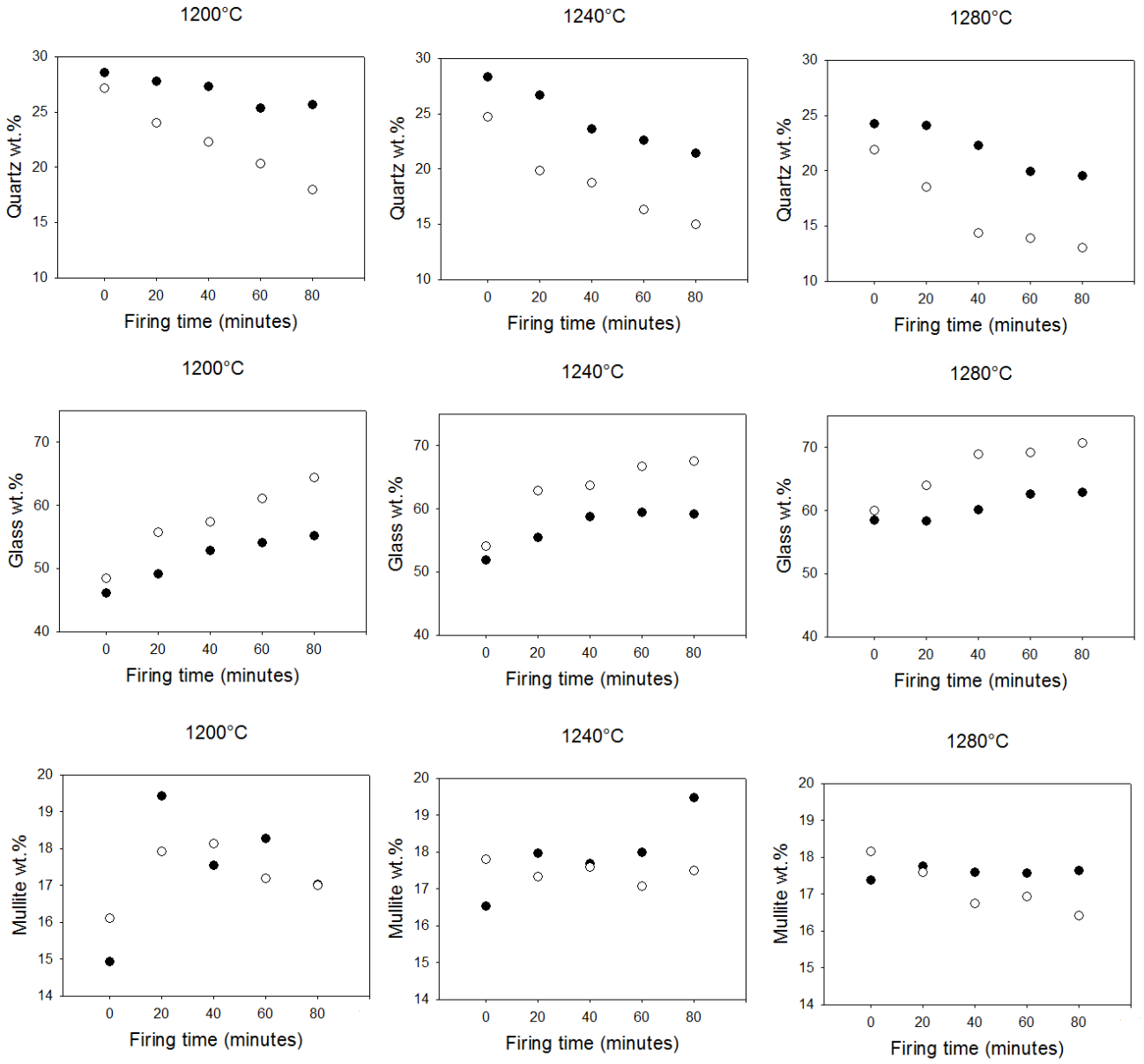

Figure 1.3: Quartz, mullite and glass wt.% evolution as a function of T_f, t_f. Black circles represent sample belonging to series S1 (quartz d50 equal to 50μm), white circles represent sample belonging to series S2 (quartz d50 equal to 18 μm).

1.3.2 Water absorption and microstructure

In both series, a prominent decrease in water absorption value has been observed when T_f and t_f are increased (see Figure 1.4, part a). At the end of the heating ramp, both series exhibit a similar value, but, if t_f is increased, samples belonging to series S2 (white circles) show lower water absorption values; this is connected to the higher reactivity of samples with smaller quartz d_{50}, that promotes the densification phenomena. In the industrial practice, water absorption must not exceed the value of 0.5; such value is never reached by samples fired at 1200°C (both series) but if T_f is increased it can be reached just after 40 min in series S2 whereas in the case of series S1 one single sample is able to satisfy this limit and it is the sample fired at the most extreme conditions (i.e. 1280°C for 80 min).

It is common to correlate the glass formation with the diminution of water absorption value because vitrification

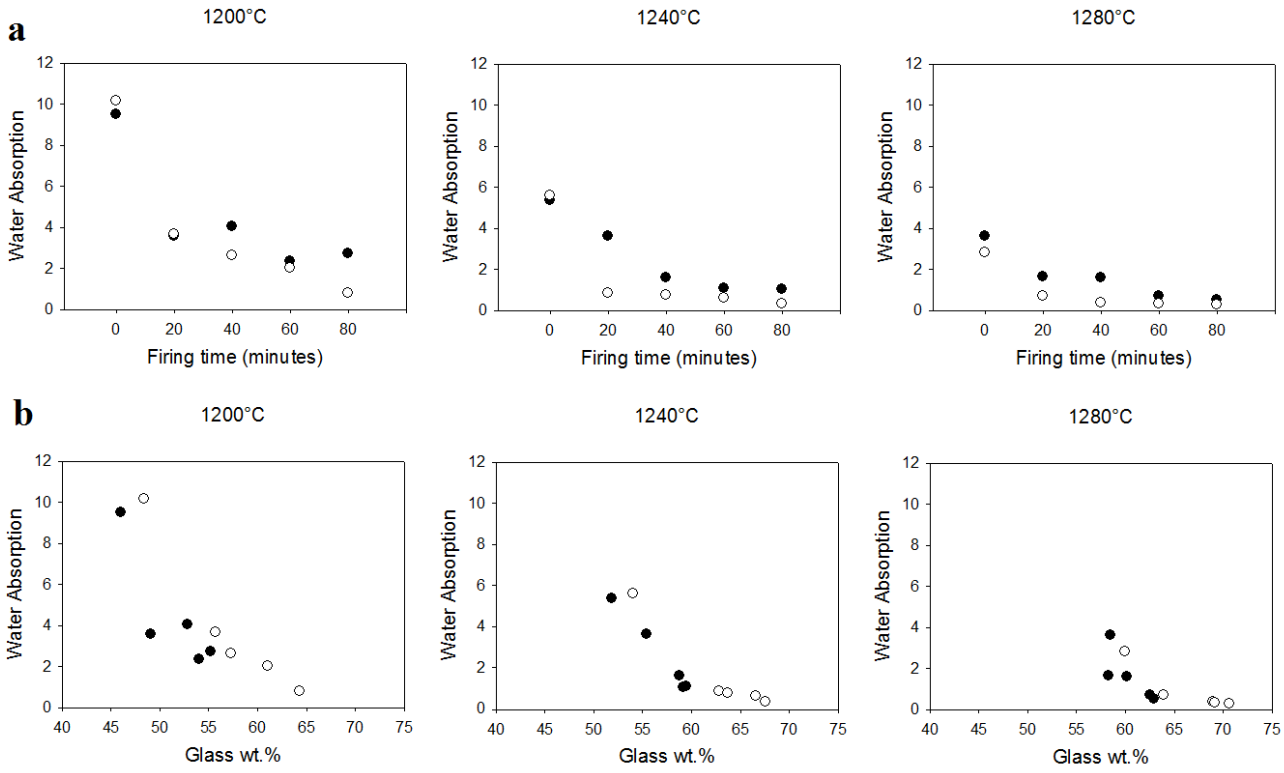

Figure 1.4: Water absorption evolution as a function of T_f and t_f. Black circles represent sample belonging to series S1 (quartz d50 equal to 50μm), white circles represent sample belonging to series S2 (quartz d50 equal to 18 μm).

process fills up the pores with a consequent more densified product. By looking at part b in Figure 1.4, this is not completely demostrated; in fact, for a fixed glass amount, the sample fired for longer time exhibits a lower water absorption value. For example at 1200°C, sample S1 fired for 80 min and sample S2 fired for 20 min have an almost identical glass amounts (i.e. 55.2 and 55.7 wt.%, respectively) but a lower water absorption value has been measured for the former sample, underlining the importance of t_f in the evolution of the densification. The light of this evidence seems to be that vitrification is mainly governed by phase transformation (such as kaolinite decomposition, feldspar melting) whilst densification has a slower development. In order to better comprehend the role of t_f on the water absorption decrease, the partial W.A. contributions have been introduced. The contribution in the first 40 min (% W.A.$_{0-40,T}$) results from Equation 1.5:

$$\%W.A._{0-40,T_f} = \frac{W.A._{0,T_f} - W.A._{40,T_f}}{W.A._{0,T_f} - W.A._{80,T_f}} \tag{1.5}$$

where $W.A._{0,T}$, $W.A._{40,T}$ and $W.A._{80,T}$ are the water absorption values after 0, 40 and 80 min, respectively, for a fixed T_f. The corresponding W.A. contribution in the 40-80 min interval is calculated subtracting the W.A. contribution in the 0-40 min interval from the 100%. The results are summarized in Table 1.3. Similar values have been obtained (about 80%), for both quartz particle size, at 1200°C, indicating a well marked densification in the 0-40 min interval rather than the 40-80 min interval. At 1240 and 1280°C, if quartz with d_{50} equal to 18 μm is used, the W.A. contributions in the 0-40 min interval are 92 and 96%. These values emphasize the role of this interval on the densification even if, as previously said, are not enough to reach the 0.5 limit. In the case of samples containing quartz with bigger d_{50}, the W.A. contributions are more balanced, especially at 1280°C. Thus,

T_f	S1	S2	S1	S2
°C	0-40 min	0-40 min	40-80 min	40-80 min
1200	80.44 %	80.35 %	19.56 %	19.65 %
1240	86.96 %	92.04 %	13.04 %	7.96 %
1280	64.94 %	96.07 %	35.06 %	9.93 %
Average	77.45 %	89.49 %	22.55 %	10.51 %

Table 1.3: Water contributions in the ranges 0-40 and 40-80 min in both series for the different explored T_f.

in general, the first 40 min contribute most to densification, but only through the next 40 min that the material is able to reach the desired value of water absorption.

Scanning electron microscope analyses have been performed to investigate the micro-structural evolution in all samples. To emphasize the differences in discussion of the results, the number of presented sample was reasonably reduced, in each series, from 15 to 3. Such samples were treated at 1200, 1240 and 1280°C at 0, 40 and 80 min, respectively; so the reader is able to easily comprehend the role of an increased T_f and t_f on the micro-structure (see Figure 1.5).

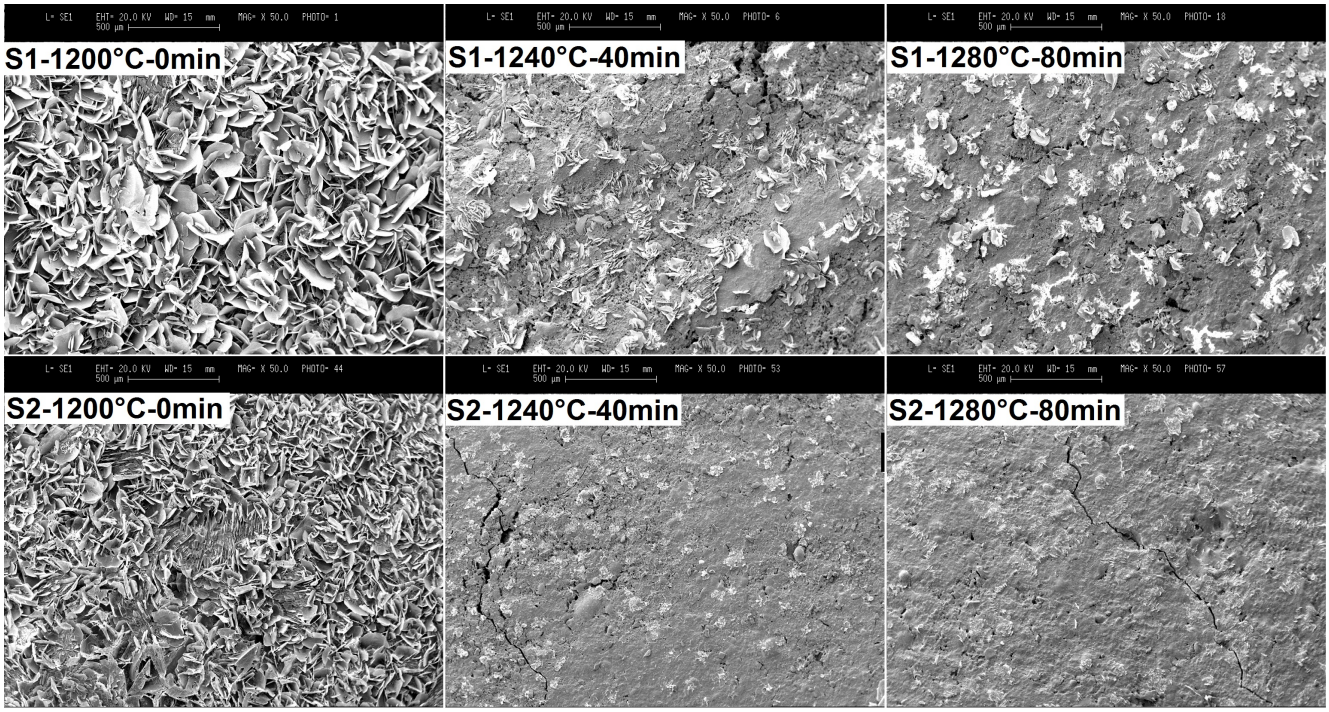

Figure 1.5: Backscattered electron images of selected samples. Surfaces have been etched with BF_4H.

At the end of the heating ramp (e.g. fired at 1200°C for 0 min) both samples exhibit a widespread lamellar habit even if no evidence of clay mineral has been detected from X-ray powder diffraction measurements. These minerals with sheet-like morphology probably are related to the starting clay minerals that have lost they long-range order but they maintain an imprint of their starting habit. If T_f and f_f are increased, the lamellar habit progressively disappears and the surface becomes more homogeneous, especially in S2 series. Moreover, primary mullite (an example is shown in Figure 1.6, part a) and secondary mullite (an example is shown in Figure 1.6, part b) crystals have been recognized: the former assumes a "cuboidal" habit and the latter a more elongated aspect. It would seem that secondary mullite is more abundant in the sample fired at the most extreme conditions; in fact, in sample fired at 1240 and 1280°C for 60 and 80 min, mullite elongated crystals are more easily visible. Finally, the

presence of feldspar crystals has been detected in sample fired at lower T_f and t_f, in agreement with X-ray powder diffraction data.

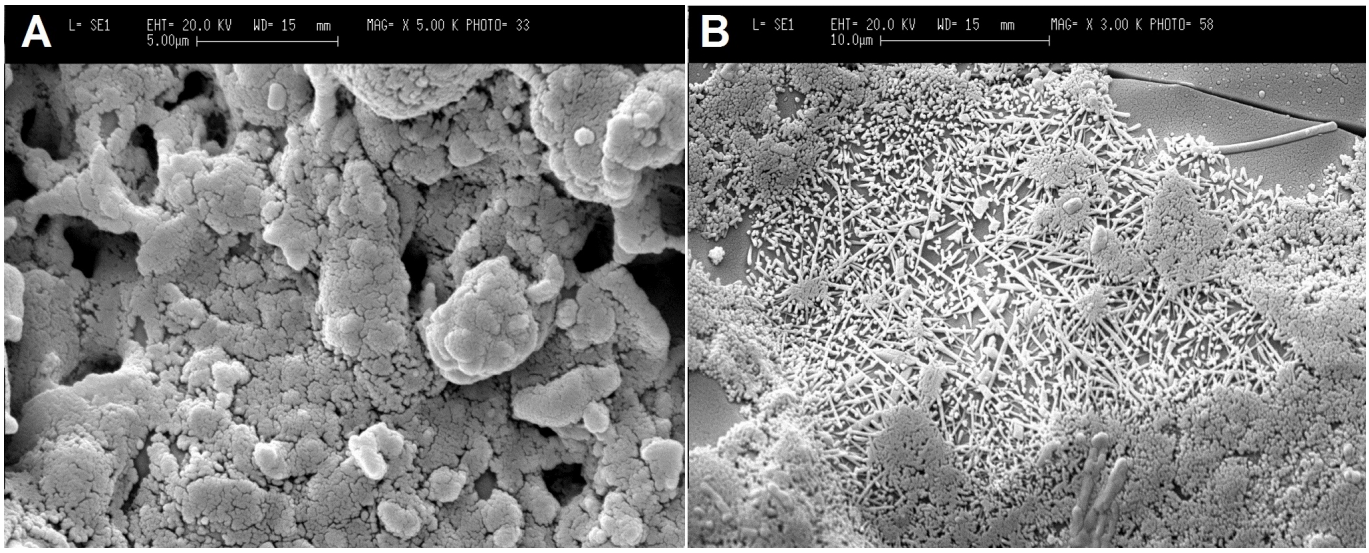

Figure 1.6: Part a: Backscattered electron image of primary mullite belonging to sample S2 fired at 1240℃ for 40 min. Part b: Backscattered electron image of secondary mullite belonging to sample S2 fired at 1280℃ for 80 min. Surfaces have been etched with BF_4H.

1.3.3 Thermal expansion

Typical dilatometric curve of sanitary-ware vitreous body is shown in Figure 1.7. It can be divided into 3 regions: from ambient temperature to 550°C the path is linear, then in the range 550-600°C is governed by the displacive quartz $\alpha - \beta$ phase transition and finally, above 600°C, is reflective of a variety of transformations involving glass phase [Stillinger, 1988].

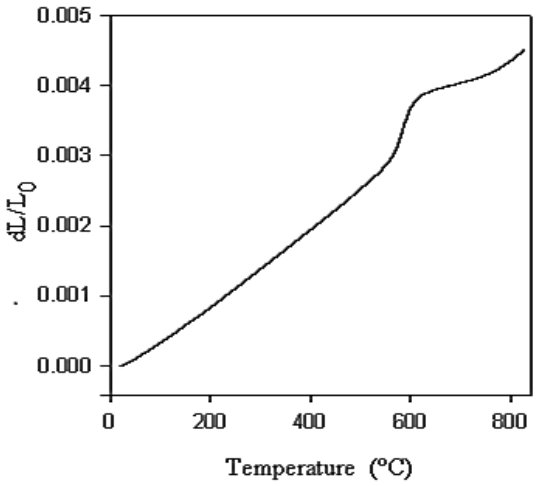

Figure 1.7: Thermal expansion curve of one of sample S1 fired at 1240℃ for 80 min.

In this study great attention was paid to the range up to 550°C because it is the most significant during cooling process; in this range, volume thermal expansion was modeled using Equation 1.3. Quartz, mullite and feldspar mean volume thermal expansion coefficients were taken from literature [Fei, 1995] and the mean volume thermal expansion coefficient of glass α_{glass} was obtained for each sample. An averaged value of 6.4 $\times$ 10 $^{-6}$°C $^{-1}$ was obtained, in keeping with those from [Fluegel, 2010] and references therein. Furthermore, α_{glass} was parameterized by Equation 1.6:

$$\alpha_{glass} = \alpha_0 + \alpha_1 \times (T_f - 1200\ ) + \alpha_2 \times t_f + \alpha_3 \times d50_{qtz} \tag{1.6}$$

where α_0, α_1, α_2 and α_3 are obtained with a minimization of the differences between observed and theoretical values of sanitary-ware body volume thermal expansion and are listed in Table 1.4. α_0 and α_3 are the most important contributors on the α_{glass}, thus quartz d_{50} influences the volume thermal expansion of glass in a more evident way than T_f and t_f.

25-550°C	α_0 ($\times 10^{-6}$ °C $^{-1}$)	α_1 ($\times 10^{-6}$ °C $^{-1}$)	α_2 ($\times 10^{-6}$ °C $^{-1}$)	α_3 ($\times 10^{-6}$ °C $^{-1}$)
Coefficient values	6.711	0.041	0.071	-0.147
Contribution % to the total α-value	105	25	43	-75

Table 1.4: Glass thermal expansion parametrization results obtained with Equation 1.6.

The negative sign of α_3 can be easily understood by calculating the differences between the linear thermal expansion coefficient of sample S1 and sample S2 (i.e. α_{S1}-α_{S2}), if T_f and t_f are fixed. In fact, even if the quartz

amount in S1 samples is systematically higher than in S2 sample, these differences tend to be negative as shown in Figure 1.8 (part a). Probably, such behavior may be ascribed to the interface between quartz and glassy matrix which may act as a "cushion" that compensates the dilatation of quartz, the phase which expands more in the sanitary-ware vitreous body. This mechanism might be enacted through detachments of the glassy matrix from quartz surface, and/or complex micro-structural arrangements of the glass phase in the vicinity, both favored by the large continuous surfaces of big quartz grains. The prominent influence of quartz in thermal expansion behavior is shown in Figure 1.8 (part b) where a correlation between quartz amount and linear thermal expansion coefficient of samples is present.

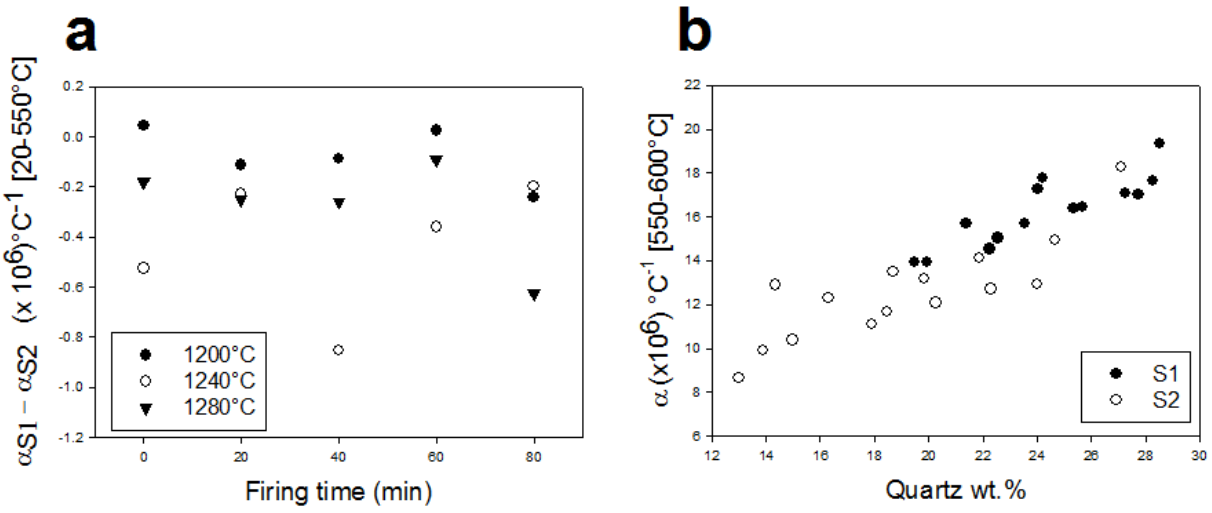

Figure 1.8: Distribution of α_{S1}-α_{S2} differences at different T_f and t_f in the 20-550°C range, part a. Relationship between quartz amount and α linear thermal expansion coefficient in the range 550-600°C , part b.

1.4 Conclusions

All the investigated parameters (T_f, t_f and quartz d_{50}) strongly influence the phase evolution, micro-structure and thermal expansion behavior. In particular:

1. Quartz decreases if T_f and t_f are increased and its dissolution trend is more marked if its starting d_{50} is 18 μm rather than 50 μm. On the opposite, glass formation is promoted if T_f and t_f are increased, and if quartz d_{50} is smaller. In both phases, the evolution is more evident in the first 40 min of high temperature treatment. Mullite content is connected to the presence of feldspar: if feldspar is still present between 8 and 10 wt.%, mullite does not exceed 16 wt.%, whilst if feldspar is less than 4 wt.%, mullite lies constant between 16.5 and 19.5 wt.%. Both typical mullite habits have been recognized; in particular, secondary mullite formation (elongated crystal) seems to be promoted for the highest T_fs and t_fs.

2. Water absorption value has also a preferred abatement in the 0-40 min interval even if the 40-80 min interval is fundamental to obtain the desired final product. Moreover, the correspondence between water absorption values and glass amounts is not univocal, indicating that vitrification develops faster than densification;

3. the volume thermal expansion coefficient of glass is significantly affected by quartz d_{50} to a lesser extent by t_f, and in a minor way by T_f. The average α_{glass} measured is 6.36 $\times$ 10^{-6}°C^{-1}, corresponding to an average linear thermal expansion coefficient of 2.07 $\times$ 10^{-6}°C^{-1}.

These results should be placed in a relative scale due to their conditionability by some parameters like raw materials, static kiln, heating ramp; so, a comparison with similar works must take into account that.

Chapter 2

Sanitary-ware glazes

2.1 Introduction

Glazes are stable coating deposed on the ceramic support which are obtained by firing a well defined assembly of raw materials. Historically, glazes were created for earthenware to better storage and transport of liquids and foods. Afterwards, they started to be used for decorative purposes due to a wide range of aesthetical properties. Differently from whiteware body, glaze formulation can be extremely different due to required aesthetical/technological properties of the finished product, which subsequently affects the adopted process in glaze manufacturing. Such properties are conferred by the crystalline phases and depends for example by their color, refraction index, hardness, thermal expansion coefficient, density and crystal habits. Two are the most common way to realize ceramic glaze: i) including desired crystalline phases in the starting mixture or ii) inducing their crystallization from a glass parent composition. In the former process, the largest part of crystalline phases (i.e. feldspar, calcite, kaolinite, quartz) melts upon heating and then give raise to a glass phase. Inert crystalline phases partially dissolve but are still present in the final glazes in form of dispersed crystals, embedded in the glassy matrix. In the latter process, the crystallization of a glass consists of a nucleation stage in which small seeds develop in the glass and then, at higher temperature, the crystals enlarge until they reach the required size. In both processes, the compatibility of these crystalline phases with the glass matrix and the ceramic body are crucial.

By virtue of such considerations, the classification of glazes is very difficult and can be based on:

1. fusibility behavior, that is conditioned by the fluxing agent. In general, feldspar, calcite and dolomite are used;
2. presence of an important component, like, for example, lead;
3. adopted firing process. In glazed tiles production, single-firing process is the most adopted strategy even if, in some cases, the support is fired, then glaze is applied and finally treated with an additional cycle (double-firing process). Some decorated earthenware materials can require a further firing at lower temperature.
4. effect on the surface, that depends from the application of material. Glaze can be shining, satin, transparent, opaque or colored.

In sanitary-ware application, opacity and whiteness are required and are strongly determined by the crystalline phases dispersed in the glass matrix. Zircon silicate ($ZrSiO_4$), zirconia (ZrO_2), zincite (ZnO), rutile (TiO_2) and cassiterite (SnO_2) are the most diffused opacifying agent used in opaque glaze production. Opacity is controlled by the difference in refrective index between the opacifier phase and the glass matrix, the number, size, shape and

distribution of the opacifier crystals, the incident light wavelength and also the thickness of the coverage. Zircon is the most diffused opacifier phase in sanitary-ware industries; a previous study about zircon showed that the maximum light scattering and whiteness can be reached if zircon particle size lies between 0.6-0.75 μm and a zircon amount of 16 wt.% [Escardino, 2001]. Both previously described mechanisms can be used to have zircon in glaze: in the case of crystallization of a glass, an appropriate amount of ZrO_2 is required whilst if zircon is loaded into starting composition, the correct amount must be calibrated. For the latter case, Castilone et al., in 1999, observed that at zircon addition lower that 3 wt. %, the largest part of it is dissolved into melts without subsequent recrystallization. Crystalline zircon in glaze enhances if zircon starting amount ranges from 3 to 13 wt.% and equals the starting amount, if its original amount is more than 13 wt.% as shown in Figure 2.1 (part a).

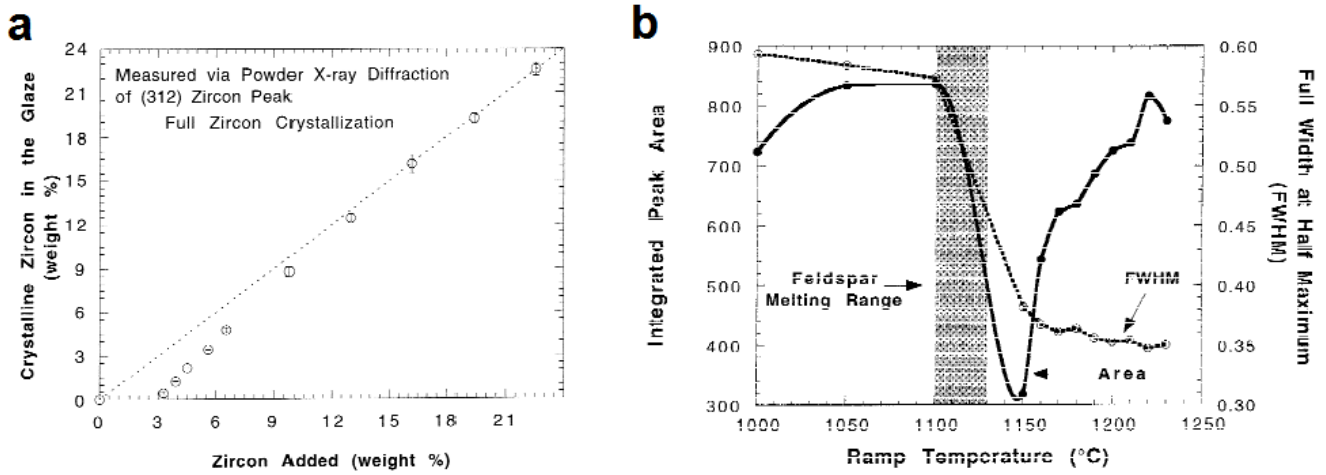

Figure 2.1: Evolution of the final zircon amount as a function of its starting amount (part a), Integrated area and FWHM for zircon (112) peak at different temperatures (part b). Figures are taken from the study of Castilone et al. (1999).

The study of Castilone et al. (1999) was also able to highlight a decrease in the zircon peak integrated area (between 1100-1150°C), due to a partial zircon dissolution, followed by an increase in the same zircon peak integrated area (between 1150-1250°C), indicating a zircon recrystallization (see Figure 2.1, part b). Moreover, the prominent decrease in FWHM in zircon peak all over the 1000-1250°C range, points out that zircon domain size is increased with temperature.

Ssifaoui et al., in 2003, studied the evolution of the number and size of zircon crystals upon firing: if zircon is added to a frit without ZrO_2 a well marked dissolution of zircon was observed coupled with a large crystal growth of zircon. Thus, the number of zircon crystal dispersed in glaze is decreased with a consequent loss of opacifying power; this is another important phenomena that must be evaluated in a glaze characterization.

Another important parameter in glaze manufacturing are the firing conditions that are related with phase evolution. Froberg et al., in 2007, carried out a study in which fast-firing and longer cycles were compared showing that fast fired glazes can contains some not fully decomposed phases (i.e. quartz) and can be free of some time favored phases (i.e. feldspar). Moreover, the same article shows how firing cycle influences the fusibility and consequently the adhesion of raw glaze to the support: a model in which the different sintering temperature have been related with main fluxing agents (such as dolomite, feldspar and limestone) have been accomplished in order to do some predictions.

This part of the present thesis is aimed at the characterization of a total of 42 different industrial glazes by means of a multi-methodological approach. In particular, the sintering behavior has been evaluated with fusibility measurement whereas phase composition and micro-structural aspect have been determined by combining X-ray diffraction, backscattered electron images and chemical-micro-analyses. Furthermore, X-ray synchrotron com-

puted micro-tomography (SR micro-CT) has been successfully used to investigate glaze pores: total bulk porosity value, size distribution and morphological characterization of voids were measured.

2.2 Experimental Procedure

2.2.1 Samples

Two sets of sanitary-ware glaze compositions have been created in order to evaluate the role of the network forming elements (in the case of series F) and the role of the network modifiers elements (in the case of series M). Then, such compositions have been prepared by weighing the correct amount of industrial quartz, kaolinite, potash feldspar, calcite, wollastonite, talc, zircon and zinc oxide. Chemical compositions are summarized in Appendix (Table 5.2 for F series, Table 5.3 for M series), mineralogical compositions are summarized in Appendix (Table 5.4 for F series, Table 5.5 for M series). For each composition, 20 g have been prepared and ground 45 min in a corundum jar-mill. About 10 g of each precursor blend have been used for flowability and hot stage measurements, the remaining part has been treated in humid condition and casted in two shapes:

1. cylinders with length and diameter of 5 and 0.4 cm, respectively. These samples have been used for thermal expansion and X-ray diffraction measurements;
2. two-dimensional slabs with 1 mm thickness deposited on an ordinary ceramic tile (50wt.% clay, 25 wt.% feldspar and 25 wt.% quartz). These samples have been used for electron microprobe and micro-tomography investigations.

Then, samples were fired up to about 1200°C following the industrial cycle represented in Figure 2.2.

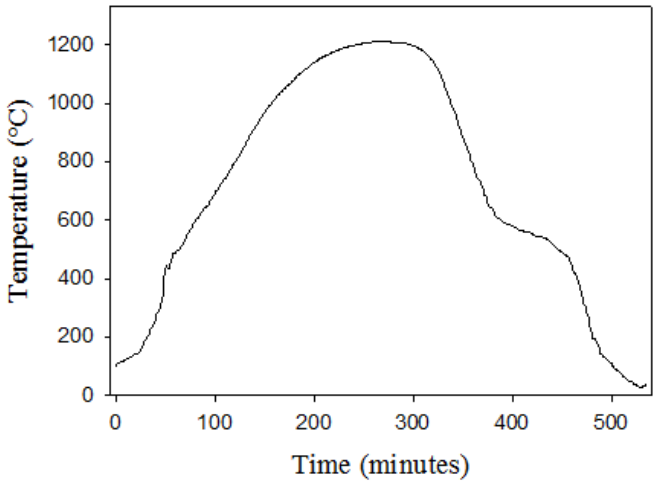

Figure 2.2: Industrial firing cycle adopted for cylinders and two-dimensional slabs.

An additional set of samples have been prepared to investigate the influence of firing time (t_f) and temperature (T_f) on the evolution of crystalline phases within the glaze. In particular, additional 200 g of M1 composition have been prepared, ground for 45 min in a corundum jar-mill, treated in humid conditions and casted into 15 cylinders as described above. Finally, each cylinder was treated separately by combining 3 T_f(1140, 1170 and 1200°C) and 5 t_f (0, 20, 40, 60 and 80 min) with an heating ramp of 10°C/min. Differently from all samples of F and M series, on these latter samples only dilatometric test and X-ray powder diffraction analysis were applied.

2.2.2 Flowability test

Flowability test are important to understand the fusibility behavior of raw glazes. For each composition, 5 g are deposited on a 45° inclined ceramic tile and fired following the industrial cycle of Figure 2.2. The sample stretches and, once is cooled, the distance is measured in millimeters. Such measurements are important to get hints about the quality of the final covering grade.

2.2.3 Hot Stage Microscope

As for flowability test, hot stage microscope observations are important to comprehend fusibility behavior of raw glaze [Paganelli, 1997; Dondi et al., 2001]. These measurements were performed by means of a Camar Microvis model, located at the Ideal Standard laboratory in Trichiana (Italy). Raw glaze powders is pressed into cylinders (length and diameter are 7 and 20 mm, respectively) and heated from ambient conditions to 1400°C with an heating ramp of 10°C/min. A camera records the outline of each cylinder every 10 s and its height (*h*) and length (*l*) are obtained. Thus, 5 different rheological temperatures ($T_{hot-stage}$) are extracted: sintering (T_{sint}), softening (T_{soft}), sphere (T_{sphere}), half sphere ($T_{\frac{1}{2}sphere}$) and melting (T_{melt}). Sintering temperature is assigned when cylinder height is 95% of the starting value while softening, sphere, half sphere and melting are assigned when the ratio 2*h*/*l* is 2.5, 2, 1 and 0.66, respectively. Finally, the influence of the different chemical species, a network ratio index (N.R.) has been introduced following the Equation 2.1:

$$N.R. = \frac{SiO_2\ mol}{(CaO + K_2O + Na_2O + ZnO)\ mol} \tag{2.1}$$

Note that molar fractions were directly taken from Tables 5.2 and 5.3.

2.2.4 Dilatometric Test

All sample have been analyzed with the same instrument and configuration of Section 1.2.3. The relationships between the volume (V) thermal expansion coefficient (α) of bodies constituted of more than one phase and such phases have been described in Equation 1.3and 1.4. In each sample, the linear thermal expansion coefficient of the glass part of glaze ($\alpha_{L,glass}$) has been determined in the 30-550°C interval by varying the unknown $\alpha_{L,glass}$ in order to cancel the discrepancies between observed-$\alpha_{L,glaze}$ and calculated-$\alpha_{L,glaze}$; the linear thermal expansion coefficient of the crystalline phases was taken from literature [Fei, 1995].

2.2.5 X-ray Powder Diffraction

Samples have been cut from fired cylinders and manually grounded in an agate mortar. Then, a 20 wt.% of high-purity calcined α-alumina was added as an internal standard to quantify the amorphous content with RIR-Rietveld method [Gualtieri, 2000]. Data collection was carried out by the same diffractometer mentioned in Section 1.2.4 in the range 5-70° , with a step size of 0.02° and an equivalent counting time of 30 s. The low content of crystalline phases in contrast with the large amorphous amount made the results from the RIR-Rietveld approach very sensitive to internal standard crystallinity and microabsorption effect [Brindley, 1945], so a parallel work has been prepared in order to clarify all such effect (see chapter 3). Therefore, powder diffraction data were used for qualitative analysis and to determine the abundances of quartz and cristobalite (if present) with the traditional RIR method [Chung, 1974] following Equation 2.2:

$$w_{qtz} = \frac{I_{qtz(101)}}{I_{cor(113)}} \times \frac{w_{cor}}{RIR_{qtz,cor}} \tag{2.2}$$

where w_{qtz} is the quartz weight fraction, $I_{qtz(101)}$ is the integrated area of the *101* quartz peak, $I_{cor(113)}$ is the integrated area of the *113* corundum peak, w_{cor} is the weighed added fraction of corundum and $RIR_{qtz,cor}$ is the RIR coefficient for quartz and corundum. On the other side, residual zircon and glass have been determined with different approaches that are explained in the Section 2.2.6.

2.2.6 Electron Microprobe

A JEOL JXA-8200 Electron Microprobe was used to perform chemical analyses in wavelength dispersive mode. All 42 samples deposed on the ceramic tile were transversely cut and embedded into araldite. The instrument was set with an accelerating voltage of 15kV, a beam current of 5nA, counting times 30 and 10 s for peak and background, respectively, and a beam spot size of about 1 μm. For each sample, 40 glass compositions have been measured along the 4 paths (10 micro-analyses/path) represented in Figure 2.3. Two main compositions were distinguished: the former corresponding to glaze surface ("upper area" U, blue lines in Figure 2.3), the latter to glaze-tile contact ("lower area" L, red lines in Figure 2.3). Al, Ca, Fe, Hf, K, Mg, Na, Si, Ti, Zn and Zr were analyzed and corrected for matrix effects following the conventional $\Phi\rho Z$ routine of the JEOL software package.

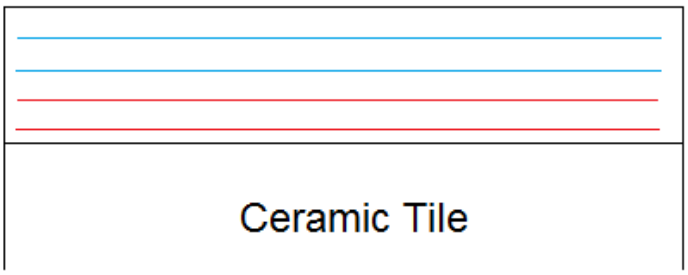

Figure 2.3: Schematic view of the strategy adopted for chemical micro-analysis.

Such investigation is aimed at the evaluation of glass homogeneity/inhomogenity from the glaze surface to the glaze-body interface. Note that crystals immersed in glassy matrix were easily identified on the basis of their shape and color, thus the recorded signals are attributable to glass phase only. For each *i*-th oxide, an "inhomogeneity index" (I.I.) was defined according with Equation 2.3:

$$I.I. = \frac{i^{th}\ oxide\ wt.\%\ in\ L - i^{th}\ oxide\ wt.\%\ in\ U}{i^{th}\ oxide\ wt.\%\ in\ U} \times 100 \tag{2.3}$$

Moreover, for each sample, two backscattered electron images have been collected with a 170x magnification and then processed by Image J Pro Plus software, Media Cybernetics Inc., 2001. These images permitted to assess the distribution of the crystalline phases within glaze. Once the most appropriate pixel range in grey scale has been attributed to zircon, quartz and pores, each image was divided into six 100 μm x 100 μm regions which provide a reliable compromise between the need of preserving intra-picture homogeneity and showing microstructural differences. Thus, an IFV (Image Fraction Value) has been attributed to the *i*-th phase for each *j*-th region as shown in Equation 2.4:

$$IFV_{i,j} = \frac{P_{i,j}}{(1 \quad - \quad P_{p,j})} \tag{2.4}$$

where $P_{i,j}$ is the fraction of pixel attributed to the *i*-th phase in the *j*-th region and $P_{p,j}$ is the fraction of pixel attributed to porosity. Then, the standard deviation of the 12 processed regions of each samples evaluated as marker of the *i*-th phase distribution.

Furthermore, by virtue of the RIR-Rietveld quantification problem described above, the residual zircon fraction by weight (X_{zircon}) was inferred in two distinct ways:

1. from chemical micro-analyses with the Equations 2.5 and 2.6;

$$w(ZrO_{2,starting}) = w_{glass} \times w(ZrO_{2,glass}) + 0.66 \times (1 - w_{qtz} - w_{crist} - w_{glass}) \tag{2.5}$$

$$w_{zircon} = 1 - w_{qtz} - w_{glass} \tag{2.6}$$

where w($ZrO_{2,starting}$) is the starting zirconium oxide weight fraction obtained from the weighed zircon (note that the loss of ignition due to volatile into calcite and kaolin have been taken into account), w($ZrO_{2,glass}$) is the amount if zirconium oxide measured in the glassy matrix; w_{qtz} and w_{crist} are the quartz and cristobalite weight fractions obtained with RIR method, respectively, in glaze; 0.66 is the stoichiometric ZrO_2 weight fraction in zircon; w_{glass} is the glass weight fraction in glaze.

2. from backscattered electron image processing [Pagani et al., 2010]. Indeed, the total volume occupied by the *i*-th phase from the *j*-th region to a *k*-th depth is given by Equation 2.7:

$$V_i = \int_0^k dz \int_j (\Phi_{x,y,z})_i \, dxdy \tag{2.7}$$

where $(\Phi_{x,y,z})_i$ is a function that describes if the *i*-th phase is occupying the (x,y,z) point. The integration above can be replaced by its numerical approximation, taking into account Equation 2.8:

$$V_i \sim \sum_{s=1,N} \triangle z_s \int_j (\Phi_{x,y,z_s})_i \, dxdy \tag{2.8}$$

where N is the number of the z-axis normal sections considered. If the section are uniformly spaced (i.e. $\triangle z_s = \triangle z_i$), Equation 2.8 is driven into Equation 2.9:

$$V_i \sim \frac{k}{N} \sum_{s=1,N} \int_j (\Phi_{x,y,z_s})_i \, dxdy \tag{2.9}$$

The $\Phi_{(x,y,z_s)_i}$ is given by image processing of the corresponding z_s section, and corresponds to the relative $IFV_{i,s}$. Equation 2.9 is now casted into Equation 2.10:

$$V_i \sim \frac{kj}{N} \sum_{s=1,N} IFV_{i,s} \tag{2.10}$$

and the corresponding volume percentage of the *i*-th phase is:

$$V_i(\%) \sim \frac{1}{N} \sum_{s=1,N} IFV_{i,s} \tag{2.11}$$

At this point, if the density of each phase is known, the relative weight percentage of the *i*-th phase ($w_i(\%)$) can be easily obtained with the final Equation 2.12

$$w_i(\%) \sim \frac{\sum_{s=1,N} V_i(\%)\rho_i}{\sum_{i=1,n}(\sum_{s=1,N} V_i(\%)\rho_i)} \tag{2.12}$$

where *n* is the number of phases involved in the volume.

All these calculations can be reasonably applied to the investigated samples if each pixel is attributed to one single phase; moreover, all these calculations can be applied to a set of 2-dimensional images if the distribution of the *n*-phases is assumed to be invariant along the *k*-depth.

2.2.7 Synchrotron X-ray Tomography

In general, imaging techniques are based on the detection of amplitude variation of the transmitted X-ray beam but if one is interested in material including objects small in size and weakly different in mass absorption coefficient, such conventional approach can be problematic. If high spatial coherence is present, "Phase Contrast" (PhC) modality is able to increase capabilities of imaging technique thank to the detection of phase shift produced by the sample on the incoming wave [Mancini et al., 1998]. PhC is generated from interference among parts of the wave-fronts that have experienced different phase shifts and it is related to Fresnel diffraction. In this modality, sample-detector distance (*D*) ranges from 10 to 100 cm, differently from absorption modality where the sample is very close to the detector. The adopted *D* value is related with the X-ray wavelength λ and the size of the feature to be identified (i.e. crystal, voids): the edge detection and the holographic regimes. The former is characterized by $D \ll \frac{a^2}{\lambda}$ and increases the visibility of edge sample features because the local phase of the transmitted beam is modified. In the latter, $D \sim \frac{a^2}{\lambda}$ and a deformed image is obtained. The Synchrotron X-Ray computed micro-tomography measurements were performed at the SYRMEP beamline of the Elettra facilities (Trieste, Italy) using the PhC modality to better study the small objects involved in sanitary-ware glazes (Figure 2.4 is a schematic view of the beamline.). Each sample was located at 20 cm from the detector and a 25 keV radiation was used.

For each sample, a total of 1400 projections were collected with an exposure time of 1 s over a 180° rotation. For each angular step a planar radiography was recorded by a 12/16 CCD camera with 4008 $\times$ 2672 pixels (pixel size is 9μm $\times$ 9μm) coupled with magnifying optics. Then, all radiographs were treated with a filter back-projection algorithm and a 3-dimensional image was obtained. The microstructural analysis was performed using

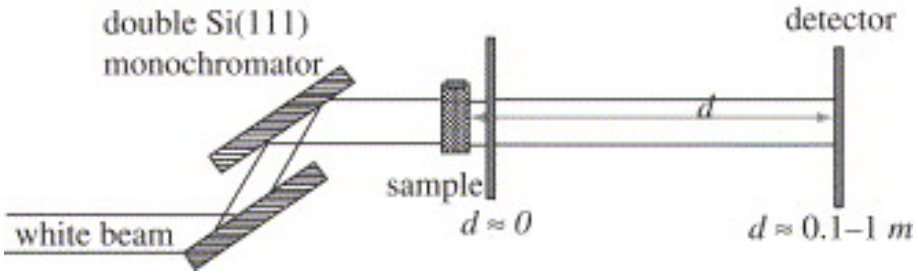

Figure 2.4: Schematic view of SYRMEP beamline set up used for absorption and PhC modalities. Figure was taken from A. Abrami et al., 2005.

the Blob 3D software; this program allowed to investigate voids volume, connectivity, shape and size distribution. In particular the voids connectivity has been evaluated by means of the Euler characteristic [Kabel et al., 1999].

2.3 Results and Discussion

2.3.1 Fusibility behaviour

Network forming and network modifying elements strongly influence the rheological behaviour of materials. For a typical sanitary-ware glazes composition, aluminum and silicon are network forming elements: high energy is required to break down their bonding with oxygen atoms, so they tent to promote polymerization, as in the case of melts where both elements increase the viscosity [Giordano et al., 2008]. On the opposite, calcium, sodium and potassium are recognized as network modifying elements because lower energies are required to break down their bonding with oxygen and consequently, in a melt, they tent to depolymerize the network. Flowability behavior has a prominent relationship with raw glaze compositions: the higher is silicon and aluminum content, the lower is the flowability value expressed in mm. At the same time, calcium, that is the most abundant network modifying element from Table 5.2, leads to a higher flowability values if it is introduced in the mixture. Such reliable correlations are present in both series and are shown in Figure 2.5.

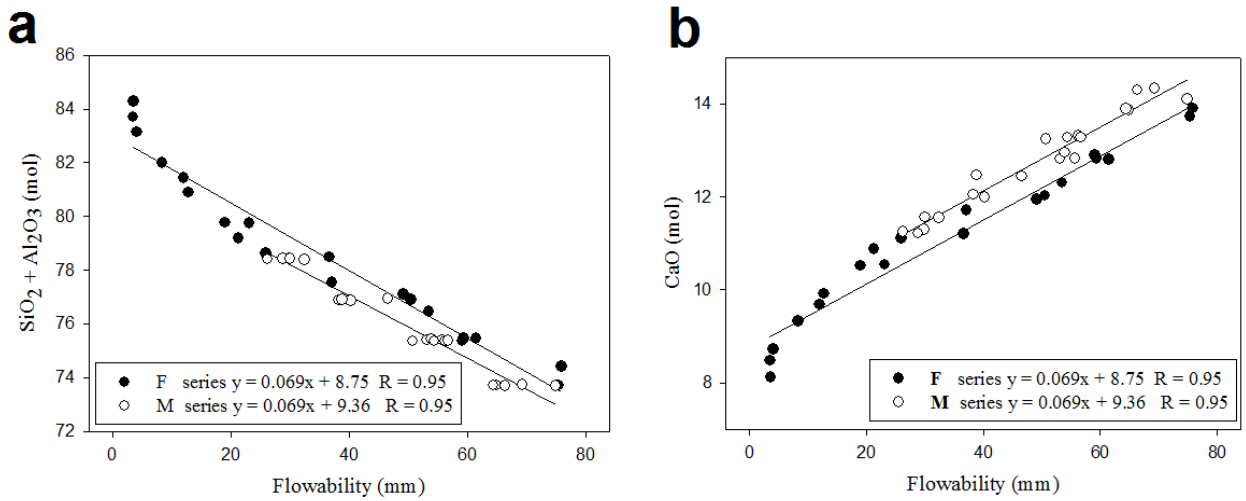

Figure 2.5: Fusibility test results. Part (a) shows the correlations with silicon and aluminum amounts, part (b) the correlation with calcium amounts. Black and white circles represent samples belonging to F and M series, respectively.

As far as hot stage microscope results, the large amount of samples and the consequent effect of noise required

to adopt clustering technique in data analysis (see Section 5.2.1, in Appendix, for details). Thus, for each series and for each rheological temperature (i.e. T_{sint}, T_{soft}, T_{sphere}, $T_{\frac{1}{2}sint}$ and T_{melt}), samples have been divided into 5 clusters and for each cluster the mean chemical composition has been determined by averaging the chemical compositions of samples that belongs to that cluster. The full results of clustering analysis are summarized in Appendix (Table 5.6 pertains F series whereas Table 5.7 pertains M series). In both series, silicon is the most abundant network forming element, so its presence tends to increase $T_{hot-stage}$. In fact, the highest amounts of SiO_2 are addressed to E clusters (i.e. the cluster with the highest $T_{hot-stage}$s). On the opposite, samples of the A clusters (i.e. the clusters with the lowest $T_{hot-stage}$s) exhibit high CaO, Na_2O, K_2O and ZnO amounts. These results can be explained by their preference for liquid phase and by the consequent fluxes role of phases that contain them. Otherwise, for silicon and aluminum it is more difficult to be incorporated into melts and consequently they are more refractory. These trends are more visible in the case of F series because its starting compositions are more different than in series M; moreover, the N.R. (network ratio) parameter emphasizes the effect of composition also in M series. In one compares the A and E clusters of the F series for softening and sphere temperatures, a N.R. difference of about 2 is present that corresponds to a mean temperature shift larger than 70°C. In the case of M series the N.R. differences lessen to about 1, corresponding to 30°C in terms of mean temperature shift. Figure 2.6 provides an example of the relationships between the $T_{hot-stage}$s temperatures and the most abundant network forming element (i.e. silicon) and the most abundant network modifier element (i.e. calcium).

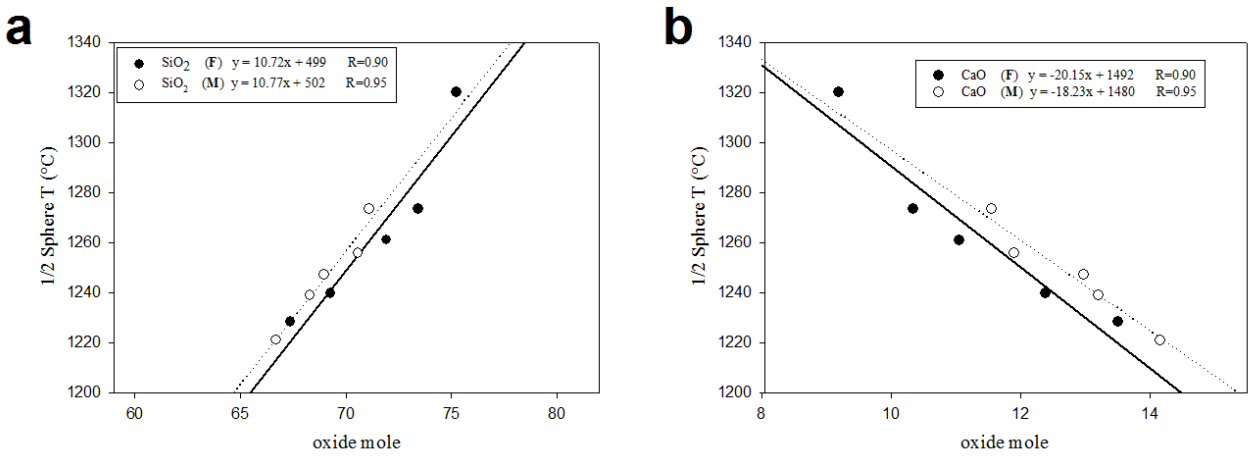

Figure 2.6: Clustering as a function of $T_{\frac{1}{2}sint}$ versus SiO_2 (part a) and CaO (part b) molar contents. Continous regression lines are related to F series, dotted regression lines are referred to M series.

2.3.2 Phases quantification and distribution

X-ray powder diffraction measurements showed that zircon and quartz are the only crystalline phases that are still present after firing cycle, save cristobalite, occurring in four samples of F-series. Figure 2.7 is an example of a collected pattern. The evident hump from 15 to 30° is related to the presence of abundant glass phase.

Before proceeding with the calculation described in Section 2.2.6, quartz amount was previously calculated with traditional RIR method. The $RIR_{qtz,cor}$ coefficient was estimated at 3.68 and after that this value was introduced into Equation 2.2. The results are summarized in Figure 2.8.

One can observe that the residual amount of quartz is very small because it dissolves during firing treatment; moreover, in general, a higher starting amount of quartz corresponds to a higher residual quartz amount. This effect is more evident in the F series, where starting quartz amount range is larger for samples belonging to M

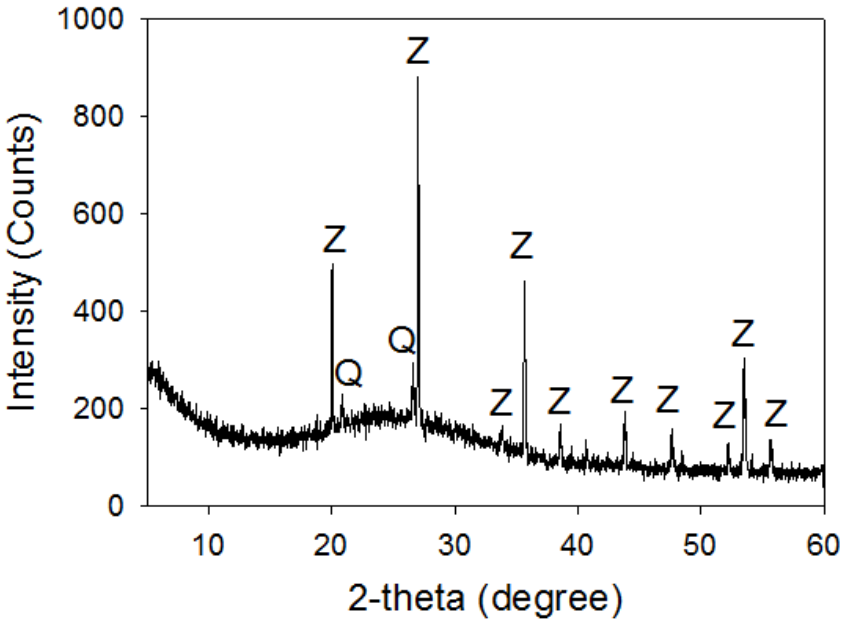

Figure 2.7: X-ray powder diffraction pattern of sample M8. Labels are assigned to each peak: "Z" and "Q" correspond to zircon and quartz, respectively.

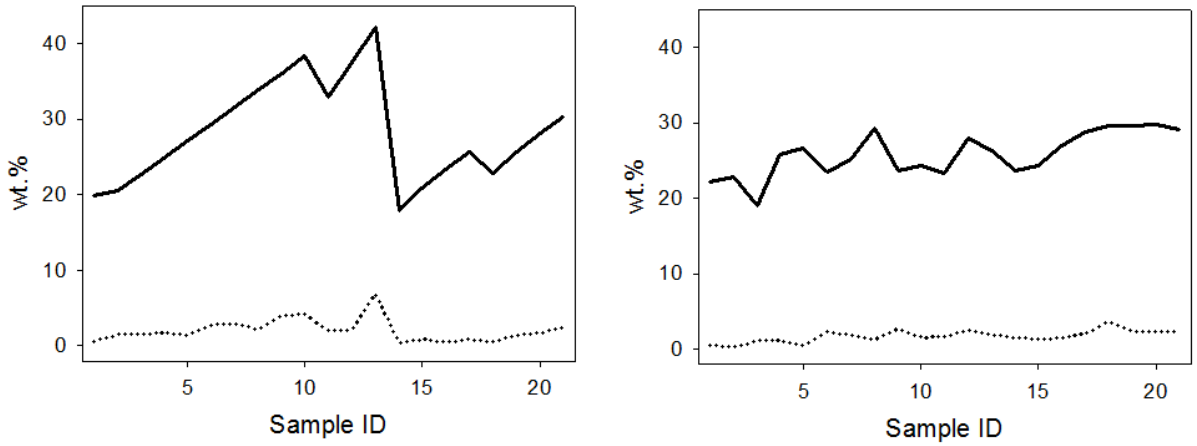

Figure 2.8: Comparison between starting quartz amount (continuos line) and residual quartz amount after firing cycle (dotted line). Graphic on the left is referred to F series, graphic on the right is referred to M series.

series (it lies between 16.8 and 40.2 wt.% in F series and between 17.8 and 27.9 wt.% in M series). Traditional RIR method was adopted also for cristobalite quantification by means of tabulated $RIR_{crist,cor}$ value [Dollase, 1965] that is 5.07. Cristobalite was detected in F10, F11, F12, F13 and F17 samples whose calculated wt.% amount is 0.35, 0.19, 0.46, 0.55 and 0.10, respectively. Once quartz and cristobalite amounts have been calculated, zircon quantification has been performed with chemical micro-analysis recalculations following Equation 2.5 and 2.6. In both series, ZrO_2 wt.% in glass ranges from 1.1 to 2.2, with a consequent dissolved zircon amount that lies between 1.6 and 3.2 wt.%. Thus, the residual zircon amount is from 5.4 to 9.9 wt.% in F series and from 8.0 to 10.4 wt.% in M series. Again, as shown in Section 2.2.6, zircon was quantified also by image processing following Equation 2.12. In this case the choice of the correct pixel range in the grey scale for zircon and quartz is very

important. Many trials were performed in order to decide the most correct one with Image J Pro software: Figure 2.9 shows 4 different threshold values for zircon with the relative quantification by mean of Equation 2.12 using the same backscattered image belonging to sample M17.

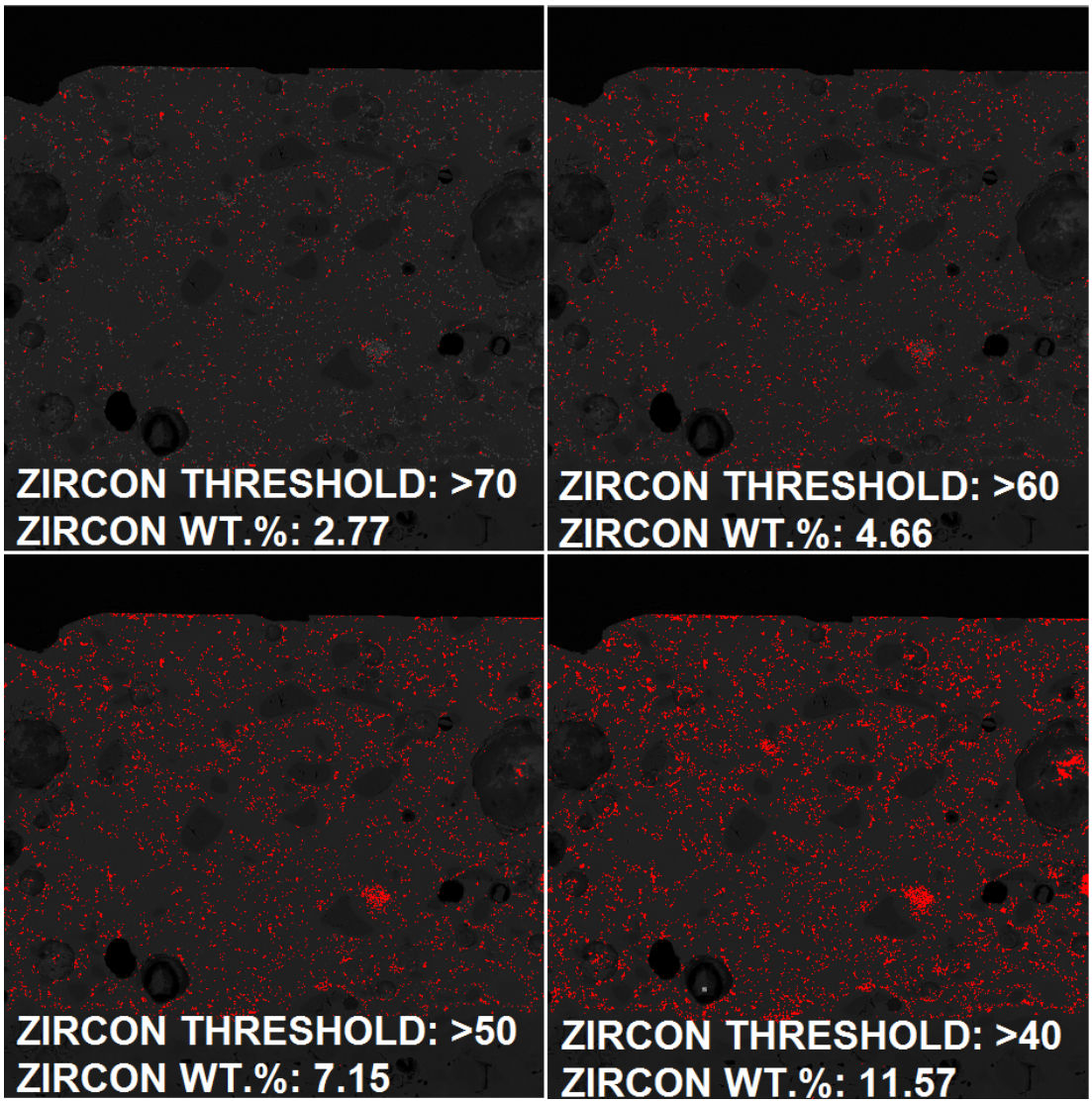

Figure 2.9: Image processing of electron backscattered image of sample M17. The different pixel range adopted for zircon are described below each picture and the final zircon quantification was performed by means of Equation 2.12.

White grains in the original backscattered images represent zircon crystals while red pixels correspond to pixel that have been assigned to the selected pixel range by the software Image J Pro Plus. If one wants to quantify zircon, all white grains must turn into red pixel, therefore, if only a fraction of these pixels have turn into red objects, zircon will be underestimated. This is the case of images treated using ">70" and ">60" threshold values that provide final zircon contents that are 2.77 and 4.66 wt. %, respectively. The other two pixel ranges (i.e. 50-255 and 40-255) allow a better conversion of white pixel into red pixel, and the zircon amount goes to 7.15 and 11.57 wt.%, respectively. At this point, one must consider the reliability of these results, if compared with the starting zircon amount that is, in sample M17, 10.4 wt.%. Accordingly, 40-255 range overestimates zircon whilst 50-255 range seems to be reasonable also by comparing it with the result of chemical-recalculation that is 8.4 wt.%. Estimated residual zircon ranges from 5.6 to 10.1 wt.% in F series and from 7.1 to 10.4 wt.% in M series. Also these values, like the example of sample M17, are in good agreement with chemical micro-analysis results,

as proven by Figure 2.10. Note that the most appropriate pixel range must be evaluated whenever beam current, voltage and brightness/contrast configuration are changed; furthermore, these parameters must be carefully defined by the instrument operator if a phase with heavy element is present (like zircon that contain zirconium) in order to avoid a systematic amplification of signal that correspond to a prominent overestimation of the occupied area of such phase.

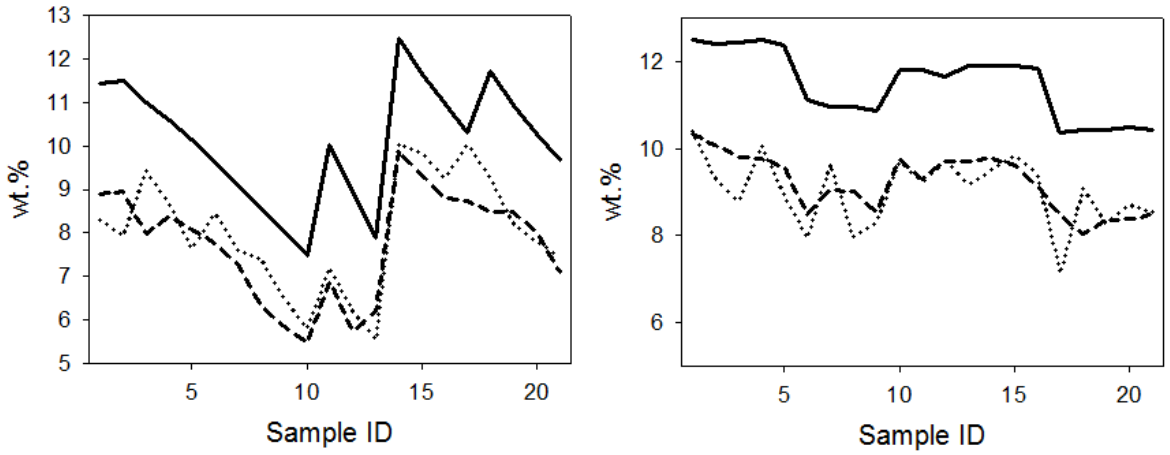

Figure 2.10: Comparison between starting zircon amount (continuos line) and residual zircon amount after firing cycle obtained by mean of chemical micro-analysis recalculation (dotted line) and image processing (dashed line). Graphic on the left is referred to F series, graphic on the right is referred to M series.

Image processing technique allowed to characterize the zircon and quartz distribution within glass matrix. As described in Section 2.6.6 each backscattered image was divided into six 100 μm $\times$ 100 μm subregions and then, for each phase, the relative IFV$_j$ values was calculated (j is the selected subregion). In the case of zircon the 50-255 pixel range was maintained, in the case of quartz the considered range was 10-25. Note that, for relative phase distribution characterization, the selection of the pixel range can be considered less univocal than in absolute quantification. In all sample, zircon IFV lies between 0.04 and 0.06 with a standard deviation that is from 0 to 0.01, thus zircon can be defined as uniformly dispersed in all the 12 sub-regions for each sample, differently from Castilone et al., (1999, see Figure 6a). No aggregations of crystals are detected, likely because the action of the thicker additive that prevents from flocculation phenomena. Furthermore, no significant evidence of zircon crystal growth was detected at variance with Ssifaoui et al. (2003), and a simple zircon grain size distribution analysis was performed with the Image J Pro Plus software showing that crystals are always smaller than 2 μm. Quartz, owing to its lower content and bigger average particle size respect to zircon's, exhibits an higher variability in IFVs, whose values lie between 0 to 0.01 with a standard deviation up to 0.008 in some samples. In the light of what has been descibed, it is not possible to precisely fix the processes involving zircon upon heating but, likely, dissolution and crystallization phenomena are present. The former is established by the presence of significative ZrO_2 amounts within glassy matrix, the latter by a different FWHM in zircon diffraction peaks before and after firing (see Figure 2.11), in agreement with Castilone et al. (1999).

2.3.3 Glass composition

On the basis of electron microprobe chemical micro-analyses, the upper and lower area compositions (see Figure 2.3 have been calculated for each sample and then the Inhomogenity Index was determined following Equation 2.3. In both series, the behavior of the I.I. is similar, as shown in Table 2.1.

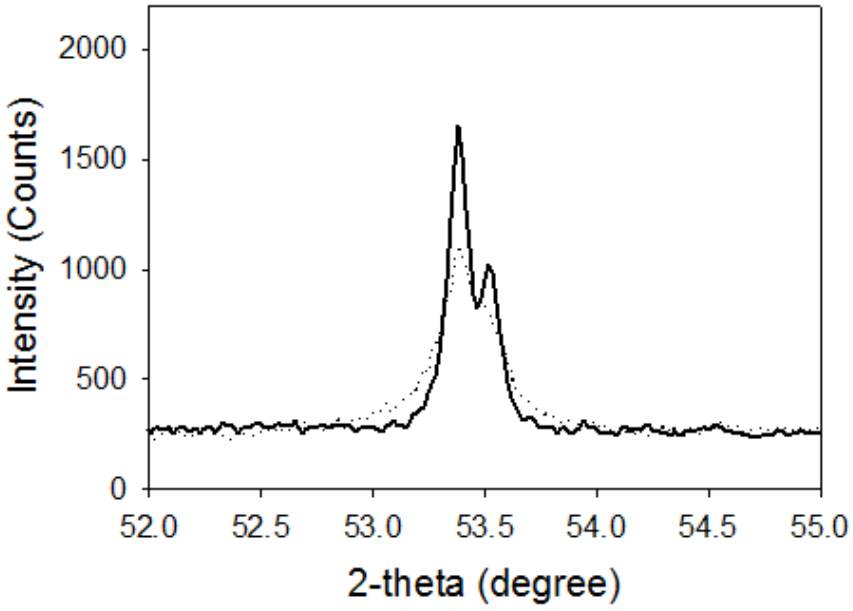

Figure 2.11: Comparison between (312) reflection of zircon in M1 sample (continuous line) and in starting zircon (dotted line). Peak full width half maximum was quantified equal to 0.108 and 0.248° 2θ, respectively.

	F series			M series		
Upper Area	CaO	ZrO_2	K_2O	CaO	ZrO_2	K_2O
Number of samples with enrichment in U-area	19	15	14	18	17	18
Mean I.I.	-10.1	-20.4	-5.2	-9.0	-17.1	-8.1
Lower Area	MgO	Na_2O	Al_2O_3	MgO	Na_2O	Al_2O_3
Number of samples with enrichment in L-area	11	20	16	18	21	19
Mean I.I.	7.7	7.5	6.5	13.0	10.0	8.8

Table 2.1: Characterization of glass composition in terms of Inhomogenity Index (I.I.) for both series.

Al_2O_3, Na_2O and MgO are more abundant in the L-zone, whereas K_2O, ZrO_2 and CaO are more concentrated in U-zone. Such a trend might be reflective of the crystal habit of the starting mineralogical phases, that may differently orient themselves with respect to the ceramic support. For example, kaolinite and talc are sheet silicates, so they have a high surface/volume ratio that could be responsible of they adhesion to the ceramic tile as proven by their preferred concentration in the L-zone. However, all the I.I. values yield so modest differences between lower and upper regions, that can conclude that all glazes exhibit a quasi chemical homogeneity.

2.3.4 Voids Analysis

Synchrotron X-ray micro-tomography collected data allows characterization of size, spatial distribution, shape and connectivity of voids inside glazes.

First of all, for each sample, a volume of interest (VOI) of 450 × 343 × 300 voxels (corresponding to about 417 × 10^6 μm^3) has been selected. The outer surface of the sample was cut off so as to focus on the inner features, more representative of the actual material. An example of a synchrotron X-ray radiation image in transmission mode is

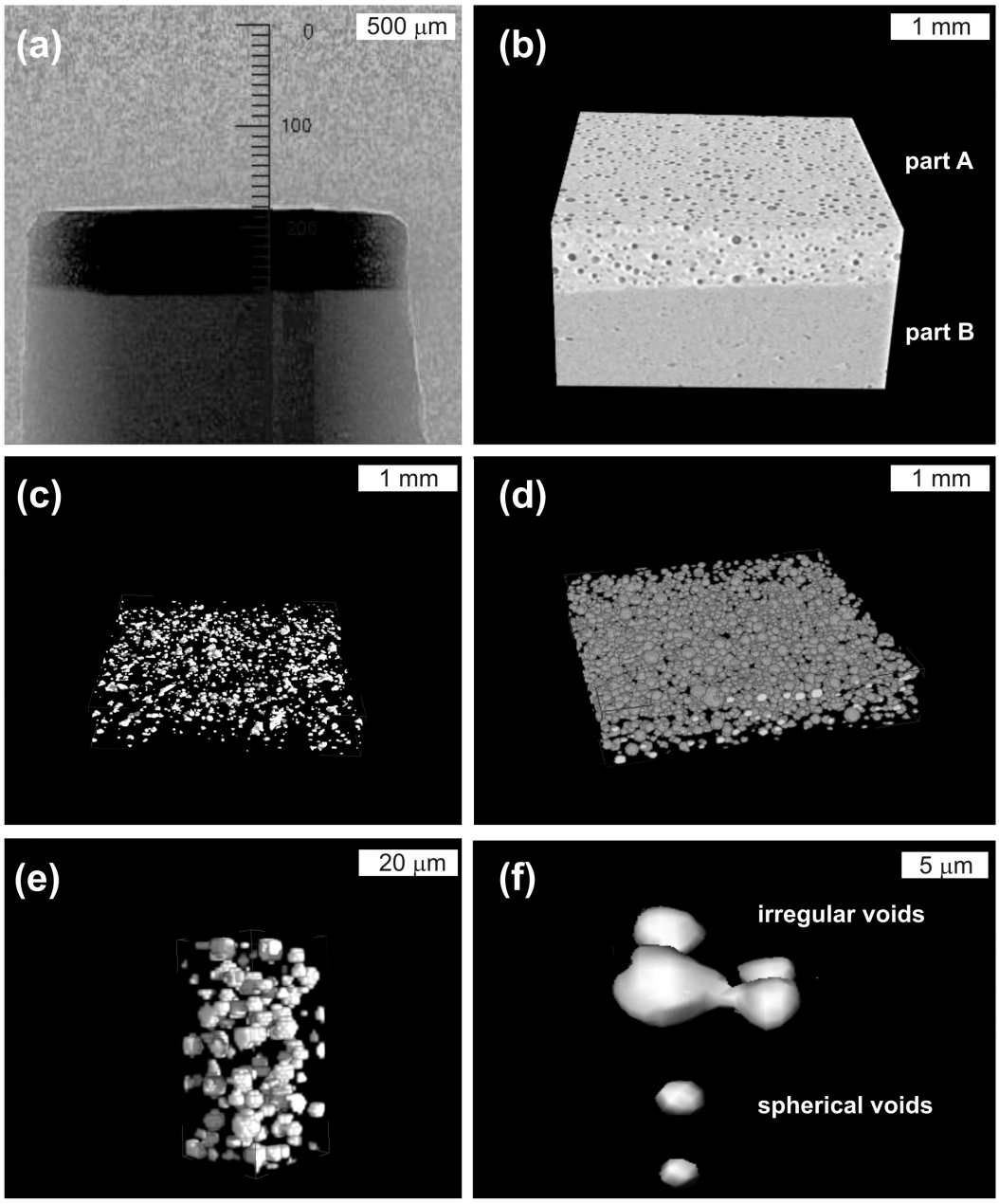

Figure 2.12: (a) transmission mode image, (b) volume rendering of a sub-volume, (c) volume rendering of voids within ceramic tile, (d) volume rendering of voids within glaze, (e) magnification of a sub-region of image (d), (f) example of spherical and irregular voids of a sub-region of image (d). All these images belong to sample F6.

provided by Figure 2.12 (part a), where the upper and darker part is glaze because of its higher X-ray absorption power respect the ceramic tile (lower and brighter part). Afterward, VGStudio Max 2.0 software built up the relative volume rendering: part A is glaze, part B is the ceramic support. A well marked porosity can be easily assumed for glaze, whereas in ceramic support the porosity is less pronounced. As in the case of backscattered electron images, the quantification procedure requires the definition of a threshold value of grey scale-level to discriminate the features one is interested in (i.e. voids) from the others parts of the material. In the present work, the adopted range for voids is from 0 to 10 allowing to obtain three-dimensional rendering like the one displayed in Figure 2.12 (part c and part d). In the case of ceramic tile the volume quantification of voids lies between 0.6 and 4.7 % and such voids are prevalently irregular in shape. The volume occupied by voids in glazes is much

greater and ranges from 10 to 20 % among all samples; moreover voids are very large, spherical in shape even if coalescence phenomena have been observed (see Figure 2.12 part e and part f). The spherical/speudo-spherical voids size distribution have been evaluated for sample F6, showing that the most abundant are characterized by having a diameter smaller than 10 μm as shown in Figure 2.13 (part a). If these data are converted into volume, the class of voids with diameter from 20 to 40 μm constitutes the 40 % of porosity whereas that from 0 to 10 μm is less than 1 % although it is the most frequent. Finally, the morphometric analysis confirm that voids are prevalently spherical up to 20 μm diameter with low tortuosity. However, largest voids are often interconnected with a negative value of the Euler characteristic ($\sim$-48mm^{-1}) that can be attributed to coalescence of originally spherical voids.

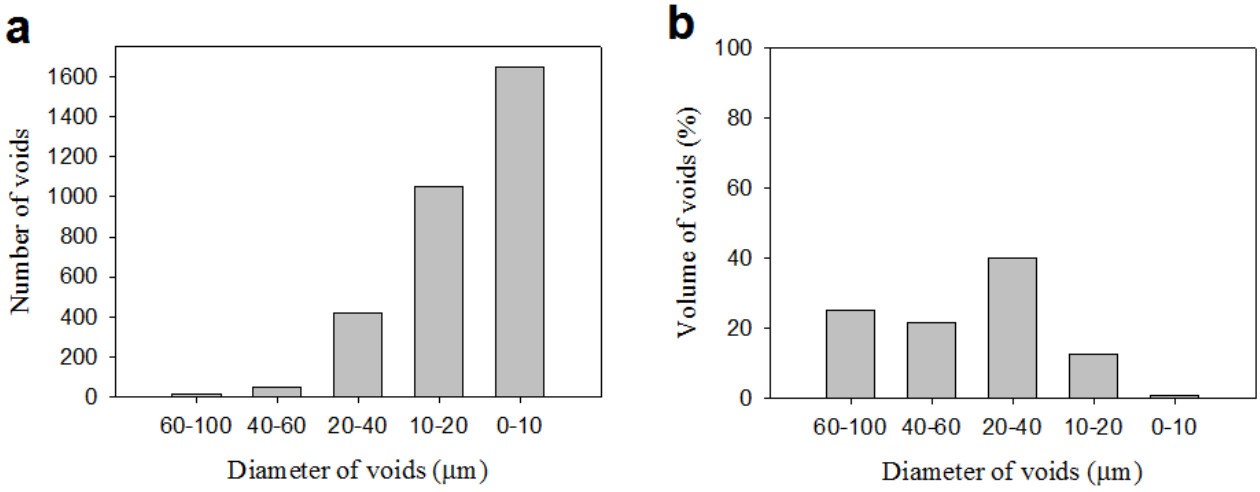

Figure 2.13: Pore size distribution in sample F6 expressed as (a) number of voids and (b) volume %.

2.3.5 Thermal Expansion

The typical thermal expansion curve of sanitary-ware glaze is shown in Figure 2.14.

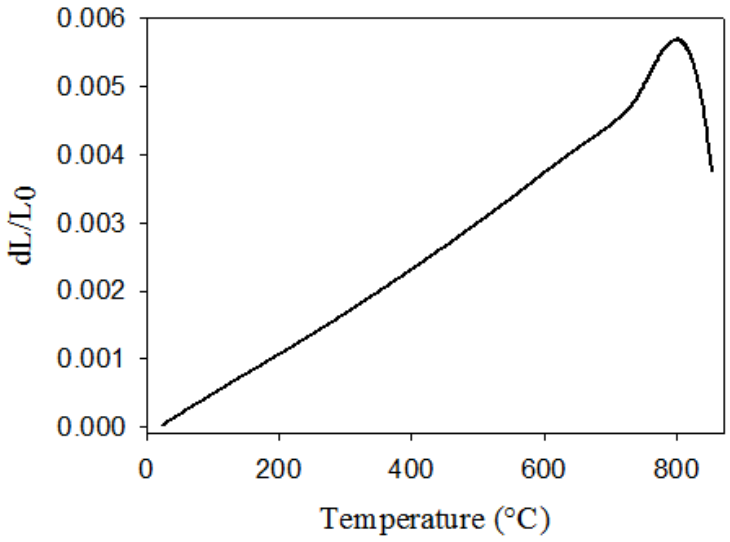

Figure 2.14: Thermal dilatation curve of sample F5 over the 20-850 °Crange.

It can be partitioned into three regions, delimited by glass transition (T_g) and softening (T_s) temperatures that are related to the presence of abundant amorphous phase. As for heating microscope measurements, data have been treated with cluster analysis and are fully represented in Appendix (see Table 5.8). Silicon and calcium are the elements that mainly control the evolution of glass transition and sintering temperatures, due to their network forming and modifier, respectively, role. In particular, clusters A, which are characterized by lower SiO_2 amounts and higher CaO amounts, exhibit the lowest glass transition and sintering temperature. This trend have been noticed in both series but is more pronounced in F series, because of its higher compositional variability (look at Figure 2.15)

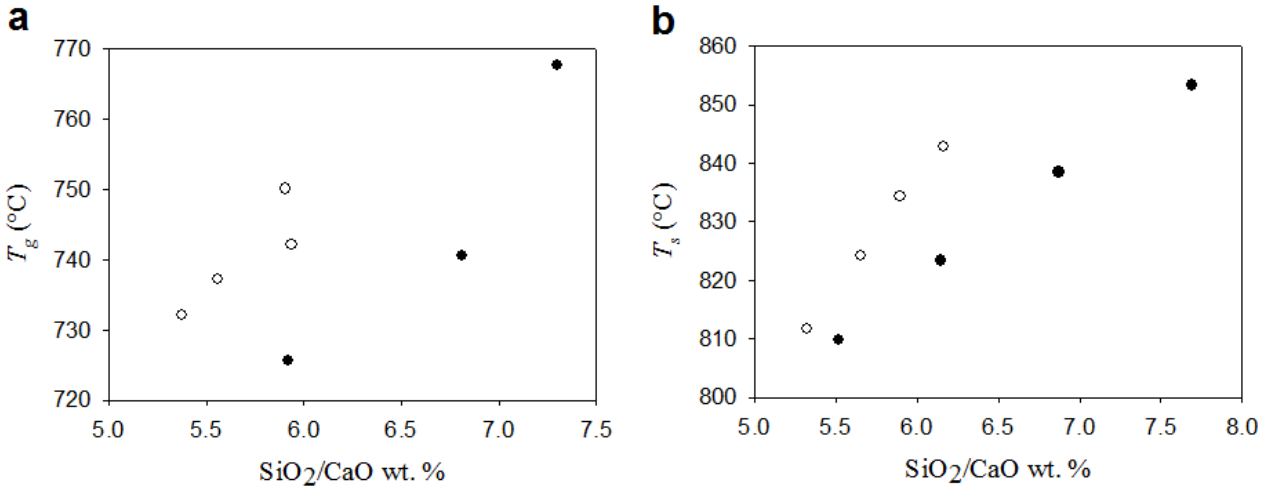

Figure 2.15: Influence of silicon oxide and calcium oxide on the evolution of glass transition (part a) and softening (part b) temperatures. Black circles represent cluster belonging to F series whereas white circles represent clusters belonging to M series.

Additionally, the linear thermal expansion of the glass phase ($\alpha_{L,glass}$) was calculated as described in Section 2.2.4 and ranges between 6.3 to 7.4 $\times$ 10^{-6}°C^{-1}.

2.3.6 Firing cycle influence

The influence of T_f and t_f has been evaluated for M1 composition with X-ray powder diffraction. Differently from the 42 sample of F and M series fired following the industrial cycle, a few samples contains also residuals feldspar and wollastonite. Due to the previously mentioned quantification problems with zircon, the phase evolution was approximated by measuring the ratio between the *i*-th phase integrated area of a selected reflection and the zircon (002) reflection integrated area. Zircon was to as denominator because it can reasonably considered the most inert phases among all those present. The results are summarized in Table 2.2.

Zircon and quartz are present for all the investigated T_f and t_f, whereas cristobalite, feldspar and wollastonite disappeared after 60 min at 1140°C and after 20 min at 1170 and 1200°C. Moreover, at 1140°C, the dissolution trend of feldspar and wollastonite is given by the reduction in feldspar/zircon and wollastonite/zircon ratios. More attention was paid to quartz dissolution trend (see Figure 2.16 (part a)).

For all T_f, the ratio moves to lower values in the 0-60 min interval, indicating that quartz dissolution trend is faster than zircon one. In particular, this trend is emphasized if T_f is increased because the linear regression slopes are -0.08 at 1200°C, -0.06 at 1170°C and -0.05 at 1140°C. Thus, both firing parameters T_f and t_f tend to increase the dissolution trend of quartz. A relevant effect of quartz dissolution is shown in Figure 2.16 (part b) where a prominent decrement of the α linear thermal expansion coefficient in the 20-540°C interval is present. The decreasing trend of zircon is more complex because it is certainly more inert than quartz in the 0-60 min

t_f	quartz/zircon	cristobalite/zircon	albite/zircon	wollastonite/zircon
1140°C				
0	1.22	0.16	0.1351	0.66
20	0.57	0.05	0.11	0.17
40	0.41	0.09	0.09	0.11
60	0.18	0	0	0
80	0.15	0	0	0
1170°C				
0	0.81	0.10	0.26	0.31
20	0.35	0	0	0
40	0.28	0	0	0
60	0.21	0	0	0
80	0.18	0	0	0
1200°C				
0	0.32	0	0.10	0
20	0.17	0	0	0
40	0.10	0	0	0
60	0.03	0	0	0
80	0.01	0	0	0

Table 2.2: Evolution of the ratio between the *i*-th phase (hkl) reflection integrated area and the zircon (002) reflection integrated area. (101), (101), (002) and (302) are the selected reflections for quartz, cristobalite, albite and wollastonite, respectively.

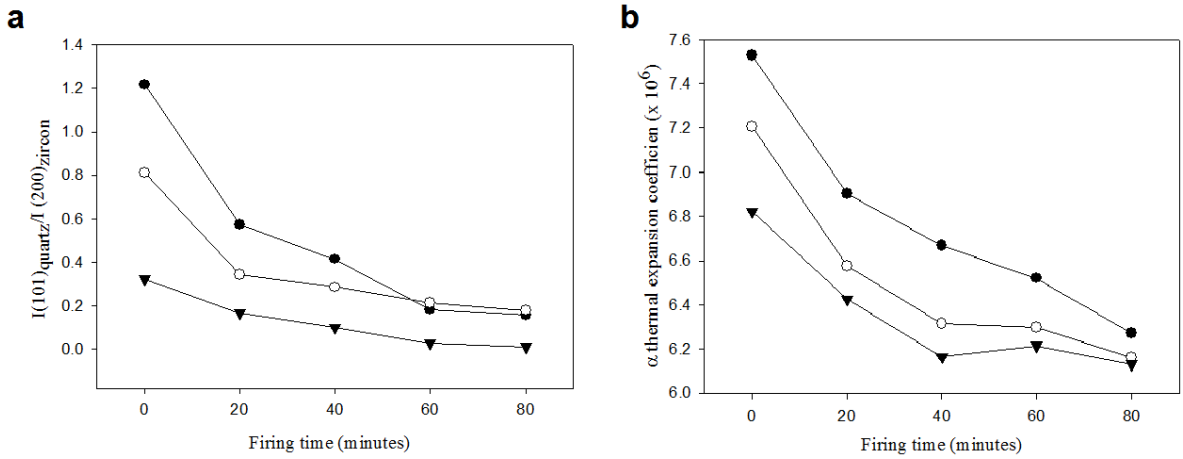

Figure 2.16: Evolution of (a) the $zircon_{200}$ and $quartz_{101}$ peak and (b) the linear thermal expansion between 20 and 540 ℃in glaze M1 fired at different T_f and t_f. Black circles, white circles and black triangles represent samples fired at 1140, 1170 and 1200 ℃, respectively.

interval whilst in the 60-80 min range the trend is flat due to: i) a silica saturation in the melt (with consequent interruption/deceleration of quartz dissolution) or ii) an increased dissolution trend of zircon. Certainly, taking into account also the presence of ZrO_2 into the glass matrix and the results of the zircon quantification by means of image processing, zircon is not a fully inert phase and the existence of a zircon dissolution, especially in the late stage of firing, is reasonable.

2.4 Conclusions

Two set of sanitary-ware glaze have been characterized using several methodology in order to better comprehend their evolution during (flowability and hot stage measurements) and after (all the others techniques) firing process.

In both series, the effect of network forming elements (silicon and aluminum) is evident: they lessen the reactivity of raw glaze as proven by the increase in T_{sint}s and heighten the viscosity as proven by the decrease in flowability tests. On the other side, the contrasting effect of network modifying elements (calcium overall) has been clearly found also in M series, even with a smaller compositional variability. The role of network forming and modifying elements was noticed also on the final products thanks to dilatometric test: the presence of silicon raises glass transition and softening temperatures whilst the presence of calcium makes them lower. Furthermore a set of tools has been introduced to better describe the final properties of these materials:

1. traditional RIR method and chemical recalculation following Equations 2.5 and 2.6 results very helpful in Quantitative Phase Analysis;
2. image processing technique appears useful for quantifying zircon amount and its spatial distribution;
3. "Inhomogenity Index" (I.I.) allows the evaluation of chemical homogeneity/heterogeneity within glass matrix;
4. synchrotron X-ray micro-computed tomography reveals the abundant presence of large voids that reaches up 15 % in volume.

Part II

Accuracy in Zircon quantification by X-ray Powder Diffraction

Chapter 3

Accuracy in Zircon quantification by X-ray Powder Diffraction

3.1 Introduction

This chapter of the thesis is aimed at the definition of the procedure which provide the most accurate results in zircon determination by X-ray Powder Diffraction technique within sanitary-ware glazes. An accurate quantification of zircon can be important to model some technological properties, like thermal expansion behavior (as shown in the previous chapter), to better comprehend aesthetical properties of glazes in terms of opacity and brightness, and to calculate how much zircon is dissolved during firing process. Moreover, the quantification of crystalline phases in mixtures by means of X-ray powder diffraction is also a matter of pure theoretical interest for the comprehension of the parameters which may affect the goodness of the results, especially if also an amorphous phase is involved. In the previous chapter, zircon was quantified with chemical recalculation and image processing because the low amount of crystalline phases in glaze (zircon and quartz) coupled with the crystallinity of the internal standard and microabsorption effect made the QPA by means of X-ray Powder Diffraction (XRPD) a tool which require additional study to achieve more accurate results. It is well known that XRPD is one of the most powerful techniques to perform quantitative analysis of a polyphase mixture [Alexander & Klug, 1974; Zevin & Kimmel, 1995; Dinnebier & Billinge, 2008]. There are different approaches: from the classical Reference Intensity Ratio method [Chung, 1974a,b] to the Rietveld refinement method [Rietveld, 1969; Hill & Howard, 1987; Bish & Howard, 1988; Bish & Post, 1993]. With the latter, it is possible to obtain the mass fraction (w_i) of each i-th crystalline component in the mixture following the Equation:

$$\frac{w_i}{\sum_j w_j} = \frac{S_i(Z_i M_i V_i)}{\sum_j S_j(Z_j M_j V_j)} \tag{3.1}$$

where S_i is the refined scale factor, Z_i is the number of unit formula in the elementary cell, M_i is the mass of the unit formula and V_i is the elementary cell volume. This method is based on the normalization constrain that the sum of all w_i is equal to 1, so the presence of an amorphous fraction cannot be directly evaluated with a standard Rietveld refinement. This approach is now widespread and it usually provides accurate results, especially when the different sources of error were taken into account. In fact, even with a good data collection, great attention must be paid to: (i) Rietveld refinement strategy, (ii) absorption/microabsorption effects, (iii) presence of amorphous matter and (iv) sample preparation strategy.

1. A summary of guidelines to perform an accurate Rietveld refinement can be found in [McCusker et al., 1999] and [Hill, 1992]. A correct background modeling is crucial because its underestimation could results in strong overestimation of amorphous fraction; again, QPA results can be strongly affected by improper atomic displacement parameters [Gualtieri, 2001] and also by preferred orientation [Chapter 11, Madsen I.C. & Scarlett N.V.Y., Dinnebier & Billinge, 2008]. Some of these problem can be easily detected by observing the goodness of the obtained fit, while in other cases it is important to check the physical meaning of the refined parameters. Others traditional approaches (e.g. the RIR method), on the other hand, are certainly quicker but face a series of problems connected to their single peak approach, the reliability of the RIR coefficients, the accuracy in extracting the integrated area of the peak, together with the impossibility to correct the most common source of bias (microabsorption effect, preferred orientation, primary extinction).

2. The presence of an amorphous fraction in the mixtures must be taken into account, even when it is small enough not to be visible in the diffraction pattern. An amorphous fraction could be present, within a crystalline phase, as structural disorder [e.g clay minerals, kaolinite overall], as an impurity in a crystalline phase, as surface layer defect [Cline et al., 2011] and it may be due, sometimes, to a grinding action effect [Zevin & Kimmel, 1995]. One of the most widely used applications of the Rietveld method is the possibility to obtain the amorphous content by adding a known amount of internal standard to the investigated mixture and then the amorphous fraction w_a is calculated as:

$$w_a = 1 - \frac{W_m}{W_s}\left(\frac{1}{w_s'} - 1\right) \tag{3.2}$$

where W_s is the weighed fraction of the internal standard, W_m represents the weight of the rest of the mixture (i.e. W_m=1-W_s), and w_s' is the refined mass fraction of the internal standard.

3. The presence of X-ray absorption contrast within the investigated mixture is a very important element that one must considers to obtain accurate QPA results. It is well know that an X-ray beam that pass through a layer of any material is partially absorbed following Lambert-Beer's law, depending on the wavelength, the thickness of the layer and the linear absorption coefficient of the material [Bish D.L. & Reynolds, R.C., 1989]. If a polycrystalline mixture is investigated this effect is strongly connected to the volume of the particles of the various phases in the sample [Zevin & Kimmel, 1995] and minimized for extremely small particle size. A lot of contributions [Brindley, 1945; De Wolff, 1956; Suortti, 1972; Hermann & Ermrich, 1987; Taylor & Matulis, 1991] helped in understanding this effect: in the simple case of a binary mixture, the less absorbing phase is overestimated. Brindley, in 1945, provided a very consistent correction that require the knowledge of the particle diameter D and the linear absorption coefficient μ of the phase. With these information, it is possible to define a correcting factor τ for each i-th crystalline phase, given by:

$$\tau_i = \frac{1}{A}\int \exp^{-(\mu_i - \mu_m)x}\, dA_i \tag{3.3}$$

where A_i is the particle volume of the i-th phase, μ_i is the linear absorption coefficient of the i-th phase, μ_m is the mean linear absorption coefficient of the mixture and x is the path of the X-ray beam within the particle. If the product $(\mu_i$-$\mu_m)x$ ranges between 0.1 and 0.01, τ can be directly included into the classical intensity equation, resulting in:

$$I_{hkl,i} = \frac{\tau_i w_i K_{hkl,i}}{\rho_i \mu^*} \tag{3.4}$$

Where $I_{hkl,i}$ is the intensity of an (*hkl*) peak of the i-th phase, $K_{hkl,i}$ is influenced by the instrumental configuration and by the structure factor of the (*hkl*) peak of the i-th phase, ρ_i is the density of the i-th phase and μ^* is the mass absorption coefficient of the specimen. Afterwards, Taylor and Matulis, showed that Brindley absorption coefficient τ can be incorporated into Eq. 3.1 to correct the Rietveld refinement results following:

$$\frac{w_i}{\sum_j w_j} = \frac{\frac{S_i(Z_i M_i V_i)}{\tau_i}}{\frac{\sum_j S_j(Z_j M_j V_j)}{\tau_j}} \tag{3.5}$$

This method has been adopted by different authors [De la Torre et al., 2001; Orlhac et al., 2001; Gualtieri et al., 2004; Leinekugel-le-Cocq-Errien et al., 2007; Suzuki-Muresan et al., 2010], giving accurate results.

4. Sample preparation is often underestimated by the operator but there are a lot of contributions that could strongly affect the QPA results, in terms of reproducibility and bias. A coarse particle size distribution can be responsible of low particle statistics but, on the opposite, an extreme grinding can produce unwanted microstrain, and, in extreme cases, amorphization [Zevin & Kimmel, 1995]. Hardness contrast among the crystalline phases of the mixture and between them and the adopted mortar must be considered. Also, great attention must be paid in weighing procedures.

In this chapter, X-ray powder diffraction experiments coupled with some Scanning Electron Microprobe (SEM) observations and laser scattering measurements were performed in order to evaluate the most accurate strategy for zircon quantification in sanitary-ware glaze mixtures.

3.2 Theoretical considerations

This section is aimed at the estimation of how amorphous and microabsortion affect the accuracy of RIR-Rietveld QPA by applying some theoretical calculations on binary 50:50 mixtures. Thus, it was observed how the Rietveld refinement results can be affected as a function of different amorphous contents, particle size and linear absorption coefficient in both phases. Furthermore, a method for quantify the effect of grinding time on a selected phase, within a multiphase mixture, has been developed.

3.2.1 Amorphous contents effect

The presence of an amorphous fraction (a discrete amorphous phase and/or an amorphous surface layer in a crystalline phase [Cline et al., 2011]) strongly influence the results of QPA analysis. If one wants to quantify the amorphous fraction in a mixture, a fully crystalline internal standard, or an internal standard with a certified amorphous content w_{OS}, is required (NIST strongly suggests the use of SRM 676a αAl_2O_3, being its amorphous content recently quantified to be 0.00975 wt.%). The latter case is the most common and it implies that Equation 3.2 should be modified by introducing the amorphous fraction in the internal standard, w_{OS}, and results in:

$$w_a = 1 - \frac{W_m}{W_s}(1 - w_{OS})(\frac{1}{w_s'} - 1) \tag{3.6}$$

So, if one wants to perform accurate QPA, the knowledge of the amorphous fraction in the selected internal standard is very important. In some cases, however, it maybe be necessary to use a standard with an unknown or not certified amorphous content as, for example, when corundum is present in the starting mixture or when the absorption coefficient of the mixture is too different from the one of corundum. If one has a certified internal standard (S) and would like to quantify the amorphous fraction of the uncertified internal standard (U), a reliable way to do so is to prepare a binary mixture (or more than one) with S and U phases. The results of Rietveld QPA can be introduced in Equation 3.6: w_a is, in this case, the amorphous fraction of the selected internal standard (w_{OU}). This consideration is true because the ratio between S and U is known: w_a is the only amorphous amount in the mixture, so it can be fully attributed to U phase. In general, in a binary mixture of two standards, four different cases are possible:

1. certified and uncertified internal standards are fully crystalline (w_{OS} = w_{OU} = 0);
2. an amorphous fraction w_{OU} is present in the uncertified internal standard ($w_{OU} \neq 0$);
3. an amorphous fraction w_{OS} is present in the certified internal standard ($w_{OS} \neq 0$);
4. an amorphous fraction is present in both standards (w_{OS} and $w_{OU} \neq 0$).

To a better comprehension, these four different cases can be explained in terms of discrepancies between the real and the Rietveld refined fraction of S and U. The real fractions would sum up to 1, i.e. (w_S + w_U + w_{OS} + w_{OU} =1), while in the Rietveld refinement case, the constrain w_S' + w_U'=1 is valid, i.e. no information on the amorphous content can be directly retrieved. In case (1), the absence of w_{OS} and w_{OU} implies that the refined fraction of the certified internal standard (w_S') and the refined fraction of the uncertified internal standard (w_U') correspond to the real fraction of the certified internal standard (w_S) and to the real fraction of the uncertified internal standard (w_U), respectively.

In case (2), things start to get complex because the presence of a w_{OU} different from 0. The sum of the real fractions (w_S, w_U and w_{OU}) is equal to 1, while the sum of Rietveld-refined fractions (w_S' and w_U') is forced to 1, with consequent discrepancies between real and refined fractions. In particular w_S' and w_U' will results larger than w_S and w_U, respectively. If we suppose to have an w_{OU} value that lies between 0 and 0.5 and a w_{OS} value equal to zero, the difference between w_U and w_U' is given by the black circles in Figure 3.1.

Note that i) the overestimation of U increases if w_{OU} is increased and ii) w_S is also overestimated by Rietveld refinement. In much the same way, in case (3), if w_{OU} is null, w_{OS} ranges from 0 to 0.5 and the ratio between S and U is unitary, the results are reversed. Problems increase in case (4) because the same refined fractions (w_S' and w_U') can be achieved by combining different values of w_{OS} and w_{OU}. Moreover, as for cases (2) and (3), w_S' and w_U' will results larger than w_S and w_U, respectively. In the same binary mixture of S and U with unitary ratio, if w_{OU} ranges between 0 and 0.5 and w_{OS} is fixed at 0.05, the difference between w_U and w_U' is given by white circles in Figure 3.1. If w_{OS} goes up to 0.10, the difference between w_U and w_U' is larger (see black triangles in Figure 3.1). So, having a certified internal standard is essential, because it allows to calculate the real w_{OU} value with Equation 3.6. In general, α-Al_2O_3 is used as an internal standard in different kind of mixtures, because of its inertness and absence of preferred orientation [Visser & de Wolff; 1964]; but, if one wants to perform accurate QPA, its w_{OS} must be determined. Obviously, certified NIST SRM 676a cannot be used to satisfy this intent but, however, a

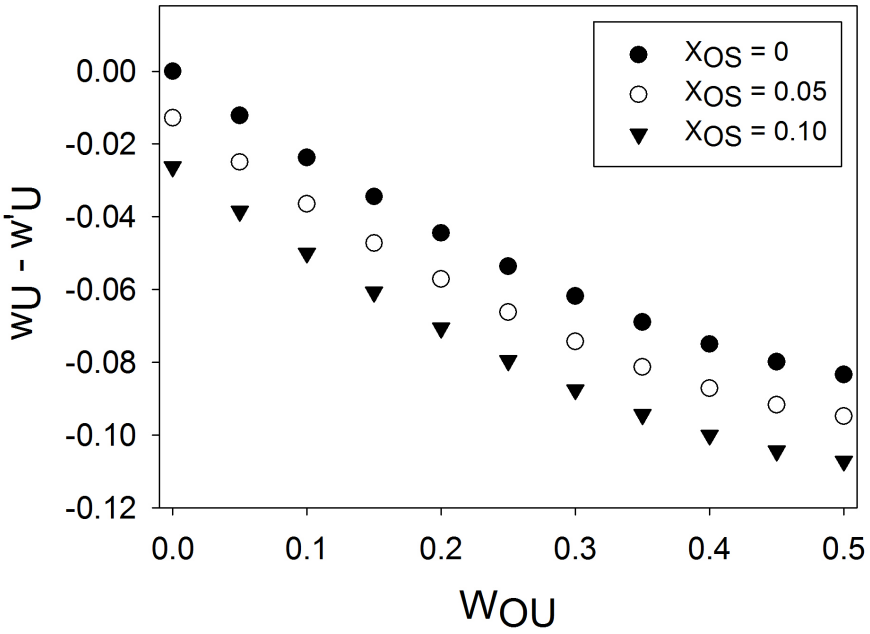

Figure 3.1: Difference between real and the Rietveld refined fraction of U (uncertified internal standard) by varying its amorphous content fraction (w_{OU}) considering a binary mixture with S (certified internal standard) with unitary ratio. The amorphous content of the certified crystalline phase fraction (w_{OS}) is fixed at 0 (black circles), 0.05 (white circles) and 0.10 (black triangles). Note that the real fraction are calculated considering that w_S + w_U + w_{OS}+ w_{OU} is equal to 1; on the opposite Rietveld refinement fractions are calculated considering the constrain w'_S + w'_U equal to 1

valid alternative is to quantify, with NIST SRM 676a, the amorphous fraction in a different crystalline phase, such as NIST SRM 640c (polycrystalline silicon), by preparing a binary mixture (or more than one) with both NIST SRMs. As described in this section, NIST SRM 676a can be considered as the certified internal standard (S) and NIST SRM 640c as the uncertified internal standard (U). The amorphous fraction of NIST SRM 640c is obtained by applying Equation 3.6 to Rietveld results of the binary mixture (or mixtures) and, in the following, NIST SRM 640c can be used as "certified" internal standard. Note that the preparation of different binary mixtures (instead of a single mixture) should improve the accuracy of the results because a wider composition range is explored and the statistics is increased. Once amorphous fraction in NIST SRM 640c has been determined, it will be possible to quantify the amorphous fraction in the selected α-Al_2O_3 (or any other uncertified internal standard) by considering NIST SRM 640c as a "certified" internal standard. This method for quantification of the amorphous fraction in a selected internal standard does not take into account the other already mentioned effects that can control the accuracy of the QPA results, such as refinement strategy, microabsorption effects, and sample preparation issues, consequently, it is important to pay great attention to them.

3.2.2 X-ray linear absorption effect

The problem of relative diffraction intensity within mixtures containing phases with different linear absorption coefficients has been observed by different authors. The most adopted correction to avoid this kind of problem is the one proposed by Brindley that is applicable when $(\mu_i$ - $\mu_m)x$ lies between 0.01 and 0.1 (medium powder range). Assuming spherical particles, x (the path of X-ray within the particle) is the particle diameter D. If this value is lower than the minimum, the microabsorption effect is negligible; otherwise, if this value is bigger than the maximum, one can consider the i-th phase as a coarse powder and the correction cannot be applied. If powders

are in the medium powder range, the correction can be applied: for each phase involved in the mixture a τ value is calculated from Equation 3.3, in order to correct the Rietveld refinement results with Equation 3.5. In Figure 3.2 is possible to observe some theoretical application of Brindley's criteria in a binary mixture where corundum (α-Al_2O_3, μ=126cm^{-1}) is used as certified internal standard (S), for the quantification of the amorphous content in a selected uncertified internal standard (U).

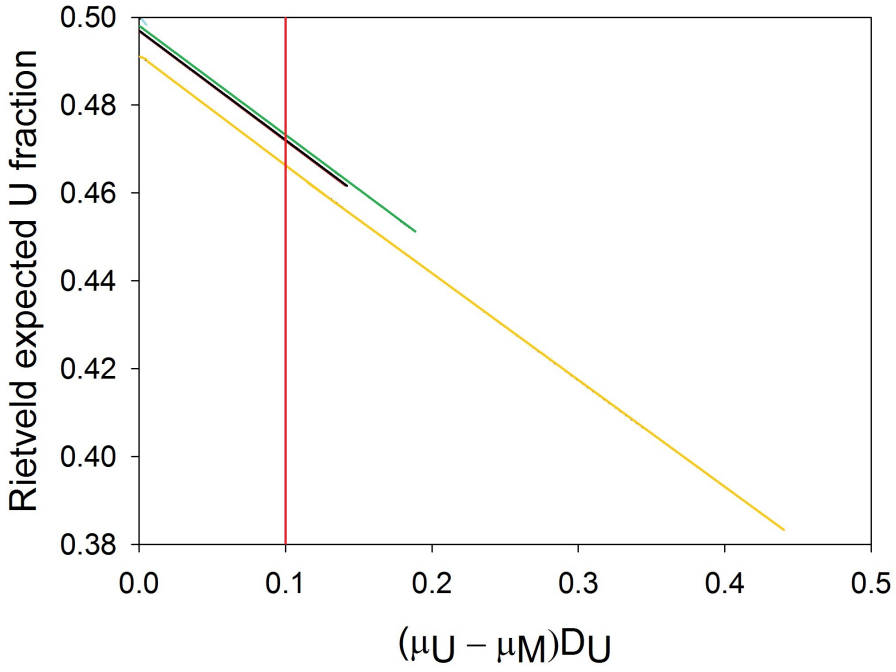

Figure 3.2: Rietveld expected fraction of different U-crystalline phases (i.e. zircon, eskolaite and silicon) mixed with corundum ($D_{corundum}$ is fixed at 1 μm) with unitary ratio. Refined expected fractions were calculated varying particle size of U-phase without the application of Brindley correction: black line, yellow line, blue line and green line are referred to zircon-corundum, eskolaite-corundum, silicon-corundum and zircon-corundum-glass mixtures, respectively. Red vertical bar represent the medium powder range limit for the application of Brindley correction.

The ratio between the two phases is unitary and, for simplification, we start by assuming that no amorphous fraction is present in either phase. If the diameter of corundum is 1 μm, and the diameter of the internal standard D_U varies from 0.1 to 10 μm, the values of (μ_U - μ_m)D_U and τ_U vary consequently. For each different value of the diameter a "Rietveld expected U fraction" can be obtained by reversing Equation 3.5. In other words this value is equal to $w_U\tau_U/(w_{corundum}\tau_{corundum}+w_U\tau_U)$. If the uncertified phase U is represented by zircon ($ZrSiO_4$, μ=391cm^{-1}) a significant underestimation is provided by Rietveld (black line). Moreover, Brindley correction will be valid, on the basis of medium size powder limit, only if zircon diameter is 7.5 μm or less. If eskolaite is U (Cr_2O_3, μ=912cm^{-1}), the Rietveld underestimation of U is larger (yellow line) than for zircon and the size limit for Brindley correction smaller (about 2.5 μm). If silicon is U (Si, μ=135cm^{-1}) the microabsorption effect is very small, the "Rietveld expected U fraction" is close to 0.5 and Brindley correction can be applied in the entire considered range of particle diameter (blue line). Finally, if one applies Brindley correction in a mixture similar to a sanitary-glaze (zircon (0.2 wt. fraction), corundum (0.2 wt. fraction) and glass (0.8 wt.fraction, μ=170 cm^{-1})), and if zircon and corundum have the same particle size, Brindley correction can be applied for a maximum diameter of about 5 μm (green line). Differences in glass linear absorption coefficient do not change the Rietveld expected results but would reduce the maximum diameter for Brindley correction application. For the sake of simplicity, in Figure 2, corundum and the different U phase were considered fully crystalline, but, if

a known amount of amorphous is present in corundum (as for NIST SRM 676a), it is possible to preliminarly apply Brindley correction to the Rietveld results, following Equation 3.5, and then introduce these latter results in Equation 3.6 to quantify the actual presence of an amorphous fraction in U. Note that, in the event that corundum is present in the investigated sample, corundum cannot be adopted as certified internal standard and a different phase must be used; the choice of a different internal standard passes through these Brindley limit calculations.

3.2.3 Grinding effect on particle size distribution

It is well known that grinding is finalized at decreasing particle size, in order to get a better homogeneity in the mixture, a larger number of particles, and therefore a better statistics in powder diffraction; in extreme cases, however, a degradation effect can occur on powders [D.L. Bish & J.E. Post, 1993; Zevin & Kimmel, 1995]. In a mixture, in which each *i*-th phase has its particle size distribution (PSD_i), the cumulative particle size distribution (CPSD) can be calculated from the single PSD_i and the relative *i*-th volume fractions (X_i), following Equation:

$$CPSD = \sum_i X_i PSD_i \tag{3.7}$$

This equation is valid if no ulterior grinding is performed after the PSD_i measurements, and it can give useful information if one of the PSD_i includes particles that are much larger than all the others in the mixture. In other words, there is a region of the CPSD (between r_1 and r_2) where there are only particles belonging to a single phase (see Figure 3.3): in this case, it is possible to calculate, for a sample grinded for two different times (t_1 and t_2), the integrated area under the cumulative CPSD between r_1 and r_2, for the time t_1 and for the time t_2.

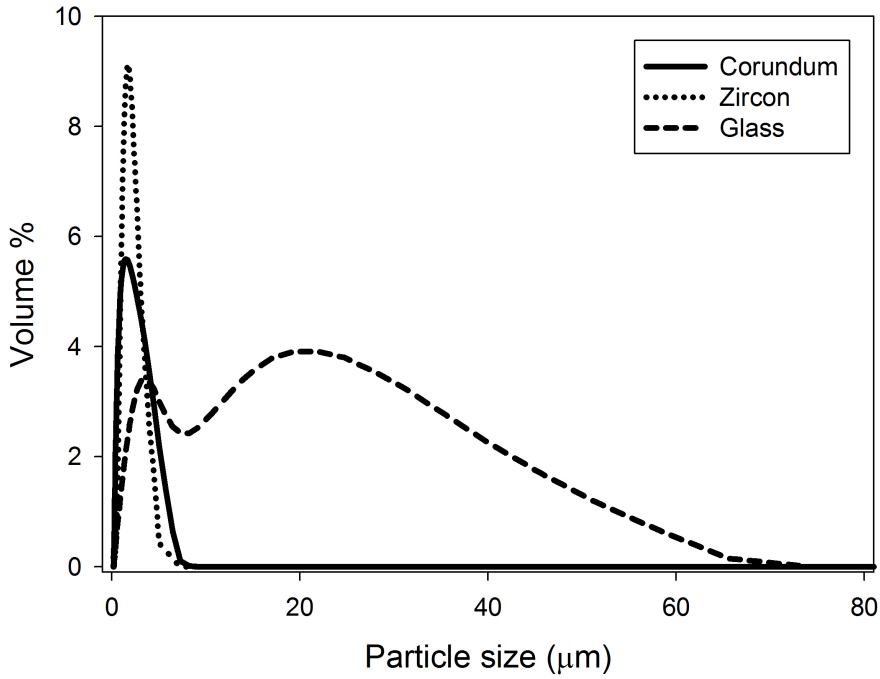

Figure 3.3: Example of three different particle size distribution curves. Corundum and zircon curves do not present particles with a diameter bigger than 10 μm.

The volume loss (i.e. the reduction of the integrated area under the cumulative CPSD due to the reduction in

radius of the particles at time t_2 with respect to time t_1) is then:

$$Volume\ Fraction\ Loss = \int_{r_1}^{r_2} CPSD(t_1)dr - \int_{r_1}^{r_2} CPSD(t_2)dr \tag{3.8}$$

Figure 3.3 is a valid example of this situation: particle size distribution curves of corundum (continuous line) and zircon (dotted line) stop at about 10 μm but particle size distribution curve of glass goes up to about 70 μm, so, in this case, it is possible to evaluate, in the particle size range 10-70 μm, the glass volume loss of the investigated sample from t_1 to t_2.

3.3 Experimental Procedure

This work is aimed at finding the correct procedure to carry out accurate (and reproducible) zircon determinations in mixtures with a large amorphous content. To do so, Rietveld-RIR technique [Gualtieri, 2001], traditional RIR internal standard method [Chung, 1974a,b] and Fullpat method [Chipera & Bish, 2002] have been applied on an artificial sanitary-ware-like mixture (90% wt. glass and 10% of industrial grade zircon) with different internal standard, in order to evaluate which one provides the better results. Table 3.1 summarizes the list of the adopted internal standard with some of their physical properties; all these standard were used to quantify zircon in *adhoc* mixture with Rietveld-RIR and RIR approaches, while, for Fullpat approach, only Aldrich annealed α-Al_2O_3 was used.

Phase	μ CuK$_\alpha$ (cm^{-1})	PSD (50%) μm	PSD (90%) μm	Density g/cm^{-3}	Hardness Mohs' scale	ICSD number & main author
SRM 676a (α-Al_2O_3)	130	1.3	2.8	4.05	9	51687 D.M. Toebbens, 2001
SRM 674a (ZnO)	279	0.8	2.4	5.56	4-5	157132 H. Rozale, 2007
SRM 674a (TiO_2)	536	0.5	0.7	4.25	6-6.5	31322 W. Gonschorek, 1982
SRM 674a (Cr_2O_3)	912	0.9	2.2	5.18	8-8.5	75577 H. Sawada, 1994
SRM 640c (Si)	140	4.4	-	2.32	7	60389 D.N. Batchelder, 1964
Aldrich annealed (α-Al_2O_3)	130	5	19.5	4.05	9	51687 D.M. Toebbens, 2001

Table 3.1: Some physical properties of the different crystalline phases involved in the experiment. In the last column there are the ICSD reference number and the first author for each structure adopted in Rietveld refinement.

3.3.1 Sample preparation

The large number of samples involved in this chapter requires an ulterior partition of this subsection into three part.

1. "Amorphous content in internal standards". As previously mentioned in Section 3.2.1, a crystalline phase may contain an amorphous fraction, even if no sign of it is shown in the relative powder diffraction pattern (i.e. diffuse scattering bump). The only standard with a certified amorphous content is NIST SRM 676a

(α-Al_2O_3), but it cannot obviously be used to evaluate the amorphous content of the other α-Al_2O_3-based standard (see Table 3.1) and also if corundum is present in the sample that one would like to investigate. To overcome this problem, three binary mixtures NIST SRM 676a (α-Al_2O_3)- NIST SRM 640c (Si) were prepared, in order to evaluate the amorphous content of standard silicon. Silicon was selected because its linear absorption coefficient is close to the one of corundum and consequently, as shown in Figure 3.2, microabsorption effect are small. Then the amorphous contents of the other standards were quantified by preparing, for each internal standard, three binary mixture with NIST SRM 640c (Si). The same procedures was adopted also to quantify the amorphous fraction in zircon ($ZrSiO_4$), whose μ (CuK_α), PSD (50%), PSD (90%), density, hardness and structure ICSD reference are 400 cm^{-1}, 1.4 μm, 3.5 μm, 4.65 gcm^{-3}, 7.5 (Mohs' scale) and 15759 [Robinson et al., 1971], respectively.

2. "*Adhoc* sample". One single batch of 20 grams of *adhoc* mixture has been prepared by weighing 18 g of glass (66.7 wt.% SiO_2, 11.9 wt.% Al_2O_3, 13.3 wt.% CaO, 2 wt.% MgO, 2.1 wt.% Na_2O, 3.3 wt. % K_2O, 0.7 wt.% ZnO, calculated μ=158 cm^{-1}). The industrial glass used is not entirely amorphous, but contains 3 wt.% of quartz (ICSD 67117 , [Dubrovinskii et al., 1989]), previously calculated by spiking with NIST SRM 676a. This does not alter the results that will be shown, as the crystalline content is fixed, and quantified. The mixture was grinded for 10 min in an agate mortar, and then 2 g of industrial grade zircon were added. After homogenization, the batch was divided in several portions, and then spiked by adding 20 wt.% of the different internal standards available. The 20 wt.% amount of internal standard was selected because of the restricted number of phases involved and because it was previously established that such quantity does not significantly abate the intensity of minority phase (i.e. quartz). Each mixture, with the relative internal standard, has been divided in two parts. The first one was grinded in a zirconia mortar, the other in a common agate mortar. After the first grinding batch (2 min, in order to homogenize the mixtures), X-ray powder diffraction data were collected. Then, two additional grinding sessions were performed (10 min each), each followed by X-ray powder diffraction data collection. Finally, in each *adhoc* mixture treated in zirconia mortar, a very small amount of zircon (about 1 wt.%) has been added in order to evaluate the sensitivity of the method to very slight change of composition; these samples are called *added* mixtures. It is important to say that the expected zircon mass fraction w_Z of each *added* mixture can be calculated with Equation:

$$w_Z = \frac{0.1W_{adhoc}(1 - w_{OZ}) + ((W_{added} - W_{adhoc})(1 - w_{OZ}))}{W_{added}} \tag{3.9}$$

And the internal standard weighed amount in *added* mixture $W_{s,added}$ must be recalculated following:

$$W_{s,added} = 0.2\frac{W_{adhoc}}{W_{added}} \tag{3.10}$$

Where W_{adhoc} and W_{added} are the weighed amount of *adhoc* and *added* mixtures, respectively, and w_{OZ} is the amorphous content in zircon. The values 0.1 and 0.2 are the starting weighed amounts, in *adhoc* mixture, of zircon and internal standard, respectively. Obviously, after Rietveld refinement, when zircon is calculated by means of Equation 3.6, W_s does not correspond to 0.2, but must be replaced by the related $W_{s,added}$. Note that the added zircon amount was not exactly the same in the different samples; so we took into account the real weighed quantities in the calculations.

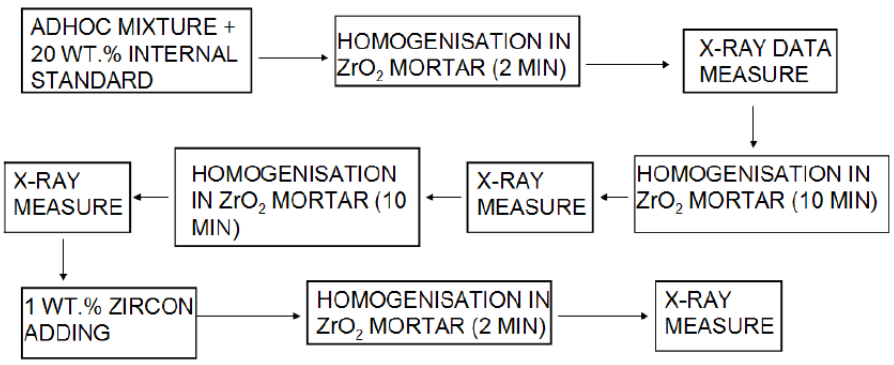

Figure 3.4: Summary of the different sessions in sample preparation and measurement.

3. "Traditional RIR and Fullpat methods". *Adhoc* mixtures are composed by a crystalline phase (zircon) and an amorphous phase. Traditional RIR method [Chung, 1974] requires a coefficient for calculating the zircon amount in each mixture. So, for each internal standard of Table 3.1, a binary 50:50 mixture with zircon was prepared, grinded for 2 min in zirconia mortar, and then measured by X-ray powder diffraction. The powder pattern was used to calculate the coefficient (one for each zircon-internal standard pair), which were used to calculate the zircon amount in the *adhoc* mixture following the Equation:

$$w_Z = (\frac{I_{200,Z}}{I_{hkl,S}})(\frac{W_S}{RIR_{Z,S}}) \tag{3.11}$$

where $I_{200,Z}$ is the integrated area of the 200 peak of zircon, $I_{khl,S}$, is the integrated area of a chosen peak of the internal standard (the most intensive peak free from overlapping) and $RIR_{Z,S}$ is the calculated coefficient for the actual zircon-standard pair. For what concerns Fullpat, a library pattern normalization is required for each phase involved in the mixture. Aldrich annealed α-Al_2O_3 were used as internal standard for Fullpat method.

3.3.2 Data collection

Samples have been analyzed with an X'Pert Pro PANalytical Diffractometer working in θ-2θ geometry and equipped with an X'Celerator multichannel detector. Initially, in order to refine the structure of each phase (see Table 3.1 and industrial grade zircon) a pattern in the range 5-110° 2θ was collected, with a counting time of 50 s/step, and a step size of about 0.008° 2θ. Afterwards all samples described in Section 3.3.1 have been collected in the angular range between 5 an 80° 2θ with a counting time of 30 s/step and a step size of about 0.017° 2θ. A sample spinner has been used during data collection in order to increase the statistic of the experiments; each mixture has been collected twice to check for reproducibility. In order to cross-check the results obtained with Cu-wavelength, a significant number of samples have been collected at the ID31 beamline at the European Synchrotron Radiation Facilities, in Grenoble, to exploit the potentiality of a very small wavelength (in the present experiment it was 0.354191 λ), of the high brilliance of synchrotron radiation. In terms of data collection, the most important advantages for this experiment were i) the dramatic decrease of microabsorption effect, due to the limited linear absorption coefficient, ii) the minimization of primary extinction effect [Sabine, 1985], iii) the detection of low quantity phases, iv) the higher investigated d-spacing range (d_{min} was 0.68 Åinstead of 1.2 Å) and v) the high instrumental resolution (Fitch, 2004). For each phase that required the amorphous content quantification

(NIST SRM 640c (Si), zircon ($ZrSiO_4$) and all the others internal standards) the high potentialities of ID31 have been exploited to one of the three different compositions described in section 3.1.1, and to the *added* mixture.

Some samples have been analyzed using a Cambridge Stereoscan 360 scanning electron microscope to investigate some aspects such as the presence of impurities (e.g. for NIST SRM 674a (Cr_22O_3), the particle size distribution (e.g. for Aldrich annealed corundum and *adhoc* mixture with NIST SRM 676a as internal standard). In all these cases, backscattered electron images have been collected at different magnification levels.

Finally, some laser scattering measurements have been carried out with a Malvern Mastersizer 2000 in humid conditions. This instrument is able to provide particle size (in the range 0.02 μm-2000 μm) by measuring the intensity of the light scattered when the laser beam passes through the dispersed sample. Such analyses have been performed on i) phases whose particle size distribution was not certified (i.e. annealed Aldrich corundum and industrial grade zircon) to be able to apply Brindley correction and ii) on some selected *adhoc* mixtures, with different internal standard, grinding time and mortar, to evaluate the effect of such parameters on the final particle size distribution.

3.3.3 Rietveld refinement strategy

All Rietveld refinements have been performed with GSAS and EXPGUI package [Larson & Von Dreele, 2004, Toby, 2001]. First of all, structural refinements of each pure crystalline phase were performed (the results are in the Appendix, see Table 5.9), in order to get a reliable structure to be used in the quantitative analyses afterwards. For each phase, scale factor, cell parameters, displacement parameters, coordinates of each atom of the structure and profile function (pseudo-Voigt type function) were refined; zero shift was corrected and instrumental background modeled with a Chebychev polynomial function.

Afterwards, the amorphous evaluation in crystalline phases has been performed on Cu-anode data: for each phase, scale factor, cell parameters and profile parameters (pseudo-Voigt type function) have been refined. Background and instrumental zero have also been refined. For NIST SRM 640c (111) plane preferred orientation has been refined using March-Dollase model [Dollase, 1986] and at the same time, primary extinction correction, following Sabine formalism [Sabine et al., 1988], was refined due to the low defectuality of this material and to the low energetic X-ray source, in agreement with Cline et al., 2011. Moreover, for ID31 data, the same strategy was adopted even if preferred orientation and primary extinction corrections were not applied on NIST SRM 640c, due to the Debye Scherrer geometry (that minimizes crystals orientation) and to the higher energetic beam (that minimize primary extinction phenomenon). Finally, the patterns relative to all the *adhoc* and *added* mixtures (for Cu-anode and ID31 data) with different internal standards, have been refined. Rietveld refinement strategy was similar to the one adopted for amorphous determination procedure even if the presence of the amorphous bump in the 2θ angular range 10-30° required the refinement of 14 parameters of the Chebychev function.

3.4 Results and discussion

For a better comprehension of the different results that will be discussed in the following paragraphs, a preliminary introduction to the different step is required.

Section 3.4.1 is focused on the determination of amorphous content in industrial grade zircon and in the different internal standards with RIR-Rietveld method. All the binary mixtures have been collected with Cu-anode apparatus; moreover, for each binary mixture a composition has been selected and investigated also at ID31 beamline. Amorphous content has been determined without and with the application of Brindley correction (Equations 3.3 and 3.5) and by means of Equation 3.6. So, for each investigated phases, 4 different amorphous content de-

terminations were obtained: two from Cu-anode data (without and with Brindley correction), two from ID31 data (without and with Brindley correction).

Section 3.4.2 shows the zircon quantification in *adhoc* mixtures by RIR-Rietveld method that have been applied taking into account the amorphous content in the standards and in zircon, obtained in Section 3.4.1. The results have been obtained by Equation 3.6 in two different ways: i) amorphous content determination was performed from Cu-anode data, with Brindley correction, and ii) amorphous content determination was performed from ID31 data, with Brindley correction. Again, the importance of exploiting equation 3.6 instead of Equation 3.2 is evaluated.

Section 3.4.3 discusses the same data of Section 3.4.2 with tradition internal standard (RIR) method and Fullpat approach.

Section 3.4.4 is aimed at the evaluation of grinding effects in terms of kind of mortar and grinding time on the *adhoc* mixture with the different internal standards. This effect has been evaluated by grinding each mixture for a total period of 2 min, 12 min and 22 min in a zirconia mortar. The same treatment has been performed with an agate mortar. Data have been collected with Cu-anode diffractometer and have been treated with RIR-Rietveld and traditional RIR internal standard methods. RIR-Rietveld results are presented with Brindley correction and by considering, in Equation 3.6, both the amorphous determinations for the different internal standards (i.e. Cu-anode and ID31).

Finally, Section 3.4.5 is focused on the determination of the sensitivity of Rietveld method to very slight differences in zircon amount on *added* mixtures (see bottom part of section 3.1.1 for details). Cu-anode data have been treated with Rietveld and RIR methods. In particular, for Rietveld results, Brindley correction has been applied with Equations 3.3 and 3.5, and then Equation 3.6 has been applied considering two different amorphous determination: the former is the one obtained with Cu-anode with Brindley correction, the latter is the one obtained with ID31 data with Brindley correction.

3.4.1 Quantification of the amorphous fraction in zircon and internal standards

NIST SRM 640c amorphous determination was done using the certified NIST SRM 676a. The Cu-anode results showed that a certain amount of amorphous is indeed present within NIST SRM 640c: 4.87 $\pm$ 2.02 wt.% (no Brindley correction) and 4.68 $\pm$ 2.02 wt.% (with Brindley correction). The standard deviation does not come from the matrix inversion in the least squares procedure, but it was calculated as the difference in amorphous content between the three compositions of each binary mixtures refined (see Section 3.3.1 for details). If ID31 data are used, the amorphous content in NIST SRM 640c (Si) is 7.24 ($\pm$ 0.23) wt.% (no Brindley correction) and 7.20 ($\pm$ 0.23) wt.% (with Brindley correction). Now that, as the purity of NIST SRM 640c can be traced back to NIST SRM 676a, it can be used to certify the purity of zircon and of the others internal standards. It is important to say that no increasing (or decreasing) trend of amorphous content in NIST SRM 640c occurred in the three compositions. Detailed results are shown in top part of Table 3.2.

In most of the cases, Brindley's correction may be applied, due to the very small particle size of the phases involved but there are two exceptions. In fact in the case of NIST SRM 674a (Cr_2O_3), the $(\mu_S\text{-}\mu_m)D_S$ value is out of the range for one composition and close to the limit for the others two composition, and in the case of NIST SRM 674a (TiO_2) the $(\mu_S\text{-}\mu_m)D_S$ values are close to the limit. In the above mentioned cases, there are marked differences in amorphous contents with and without the application of Brindley correction. Moreover, zircon is not completely crystalline, this means that, in the *adhoc* mixture, actual zircon content is lower than the weighted 10 wt.%. In order to check this latter result, an additional zircon-NIST SRM 676a has been prepared and it confirms the presence of an amorphous fraction within zircon, with results not dissimilar to those in Table 3.2: 17.47 ($\pm$ 1.42) wt. % if no Brindley correction is applied and 14.52 ($\pm$ 1.46) wt. % if Brindley correction is applied.

	SRM 674a ZnO	SRM 674a TiO_2	SRM 674a Cr_2O_3	Annealed αAl_2O_3	Zircon $ZrSiO_4$
Cu-anode					
Amorphous wt.% (1)	15.25 ($\pm$ 2.26)	7.02 ($\pm$ 2.13)	18.79 ($\pm$ 2.83)	2.90 ($\pm$ 3.07)	17.48 ($\pm$ 1.27)
Amorphous wt.% (2)	13.03 ($\pm$ 2.47)	0.69($\pm$ 3.31)	6.71 ($\pm$ 2.70)	2.93 ($\pm$ 3.06)	12.51 ($\pm$ 1.3)
$(\mu_{640c}\text{-}\mu_{mixture})D_{640c}$	-0.0187	-0.0624	-0.1061	0.0008	-0.0168
range	-0.0083	-0.0290	-0.0493	0.0007	-0.0376
$(\mu_S\text{-}\mu_{mixture})D_S$	0.0081	0.0117	0.0466	-0.0015	0.0239
range	0.0100	0.0151	0.0578	-0.0016	0.0305
τ_{640c}	1.019	1.064	1.112	0.999	1.038
range	1.008	1.029	1.051	0.999	1.017
τ_S	0.992	0.988	0.954	1.002	0.976
range	0.990	0.985	0.944	1.002	0.970
ID31					
Amorphous wt.% (1)	12.34 (2)	6.73 (2)	13.02 (2)	2.50 (1)	8.19 (3)
Amorphous wt.% (2)	11.89 (2)	6.64 (2)	12.86 (2)	2.51 (1)	7.51 (2)
$(\mu_{640c}\text{-}\mu_{mixture})D_{640c}$	-0.0021	-0.0003	-0.0006	0.0003	-0.0025
$(\mu_S\text{-}\mu_{mixture})D_S$	0.0026	0.0002	0.0007	-0.0007	0.0045
τ_{640c}	1.002	1.001	1.001	1.000	1.003
τ_S	0.997	0.999	0.999	1.001	0.996

Table 3.2: Results of the amorphous content determination in the different internal standards and in industrial grade zircon. Amorphous has been quantified with Equation 3.6 without (1) and with (2) the application of Brindley correction. In the top and the bottom parts of the table are referred to Cu-anode and ID31 measurements, respectively. Note that, for Cu-anode data, values in bracket correspond to standard deviations calculated by considering the amorphous quantifications of the three different binary mixtures. In the case of ID31 data, values in bracket correspond to the conventional sigma due to the least square refinement procedure in Rietveld refinement.

The amorphous content determination performed with Cu-anode diffractometers have been compared with the results obtained with ID31 data (bottom part of Table 3.2). These results confirm the presence of a not negligible amorphous fraction within the different internal standards and within zircon, and the values are, in general, close to the values obtained with Cu-anode. It must be considered that ID31 data are almost free from microabsorption effect. In fact, the extremely low linear absorption coefficient for the adopted wavelength minimize this effect as proven by the small values of $(\mu_S\text{-}\mu_m)D_S$ and $(\mu_{640c}\text{-}\mu_m)D_{640c}$ (see bottom part of Table 3.2).

A separate comment is needed for SRM 674a (Cr_2O_3), which, in our experiments, seems to be one of the internal standard with the highest amorphous fraction; so some Scanning Electron Microscope observations have been performed on it. Evidence of a phase with a "spider-web" like habit (crystalline or more likely not crystalline) chemically and morphologically different from (Cr_2O_3) have been found as shown in Figure 3.5, part a-b. These phase also contains sulphur evidence that could be connected with the typical synthesis adopted for these kind of material (Anger et al., 2005). On the opposite, as shown in Figure 3.5, part c, Aldrich annealed (α-Al_2O_3) results to be extremely homogeneous in terms of grey scale color and in terms of particle distribution even if, in agreement with laser scattering measurements, its particle size is bigger than the one of the other standards. A simple imaging determination of the mean particle diameters provided the values of 3.85 ($\pm$ 4.91) μm.

Amorphous quantifications performed with Cu-anode data are strongly affected by primary extinction correction. In fact, if this effect is neglected, amorphous content in SRM 640c moves to about 9.0 wt.% and consequently, also the amorphous contents in the others standards are a quite different. At the moment, the only one certificated standard is NIST SRM676a, whose certification involved the refinement of primary extinction effect on silicon powder, due to its high crystallinity, following the same refinement strategy adopted in the certification procedure of Cline et al., 2011. Moreover, further checks may be necessary, taking into account that some correlations

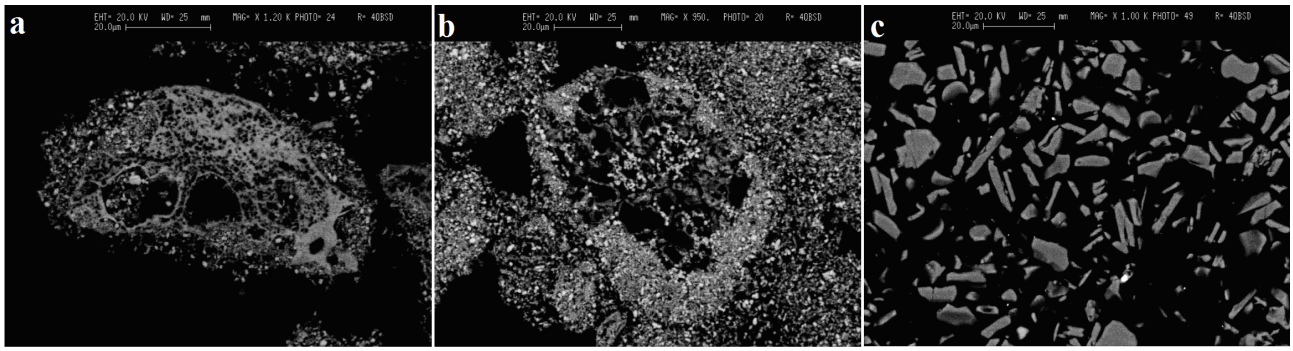

Figure 3.5: Backscattered electron images at different magnification from NIST SRM (Cr_2O_3) (a,b) and from Aldrich annealed (α-Al_2O_3) (c).

between parameters can occur during Rietveld refinement if silicon primary extinction is toggled.

3.4.2 RIR-Rietveld QPA on *adhoc* mixture with Brindley and amorphous corrections

Once Rietveld refinements of *adhoc* mixtures with different internal standards, collected with Cu-anode, have been completed, the results can be corrected for microabsorption effect, by means of Equation 3.3 and 3.5, and then for amorphous content within internal standards with Equation 3.6. It is important also to consider the presence of an amorphous fraction within zircon: this is quite large (ranging from about 8 wt.% for ID31 data, with negligible microabsorption effects, to about 12.5 wt. % for Cu-anode data, with more evident microabsorption effects), as seen in the last column of Table 3.2. The quantified zircon obtained considering Cu-anode and ID31 amorphous content determinations by applying, in both cases, Brindley correction, are represented in first and second line, respectively, of Table 3.3.

	SRM 676a α-Al_2O_3	SRM 674a ZnO	SRM 674a TiO_2	SRM 674a Cr_2O_3	Aldrich annealed α-Al_2O_3	Expected Zircon
(a)	8.70 (4)	8.97 (6)	9.16 (9)	9.25 (5)	9.53 (6)	8.75
(b)	8.70 (4)	9.08 (6)	8.61 (9)	8.64 (6)	9.57 (6)	9.25
(c)	8.80 (3)	10.31 (7)	9.21 (9)	9.92 (6)	9.82 (6)	10.0

Table 3.3: Zircon quantification in *adhoc* mixture with Brindley correction. Results are calculated with Equation 3.6 considering amorphous contents obtained with Cu-anode data and corrected with Brindley (a), and with ID31 data corrected with Brindley (b). Furthermore,in (c), additional results have been calculated with Equation 3.2.

The expected zircon amounts are very similar; NIST SRM 676a and NIST SRM 674a (ZnO) provide the most accurate zircon quantifications whereas the other three standards cause a zircon underestimation/overestimation that range from 0.4 to 1.3 wt.%. In the case of NIST SRM 674a (TiO_2) and NIST SRM 674a (Cr_2O_3) the small discrepancies can be explained by their high linear absorption coefficient, as described in previous section. The importance of applying Equation 3.6 instead of Equation 3.2 is brought to light in the third line of Table 3.3 where zircon quantification seems to be accurate for all the internal standards except for NIST SRM 676a, which provides a zircon underestimation up to 1.2 wt.%. For each adopted internal standard, a graphical fit obtained with GSAS package is shown in the Appendix (Section 5.2.3, see Figure 5.1).

3.4.3 Internal standard (RIR) and Fullpat approach

As discussed in Section 3.3.1, each internal standard has been mixed with zircon in equal amount to obtain the Reference Intensity Ratio coefficient. All the coefficients have been introduced in Equation 3.11 and the resultant

zircon amounts in the *adhoc* mixtures are summarized in Table 3.4. Obviously, the diffraction patterns adopted for these calculation are the same adopted for Rietveld calculations of previous sections. The results are more dispersed and less accurate, if compared with the results obtained with RIR-Rietveld method. RIR method is not disturbed by the linear absorption coefficient of the mixture (μ_m), so this variability in the results can be addressed to others sources of bias, as for example the presence of abundant amorphous fraction in (ZnO), (TiO_2), and (Cr_2O_3), or simply to the lower accuracy of the method because of its single peak approach. As far as the Fullpat method, this approach has been applied only to annealed Aldrich (α-Al_2O_3). After the classical library pattern normalisation of the zircon (on the 012 peak of corundum), amorphous phase has been treated as a conventional phase in the software procedure (normalised on the 014 peak of corundum). An example of the Fullpat graphical fit can be observed in Figure 3.6.

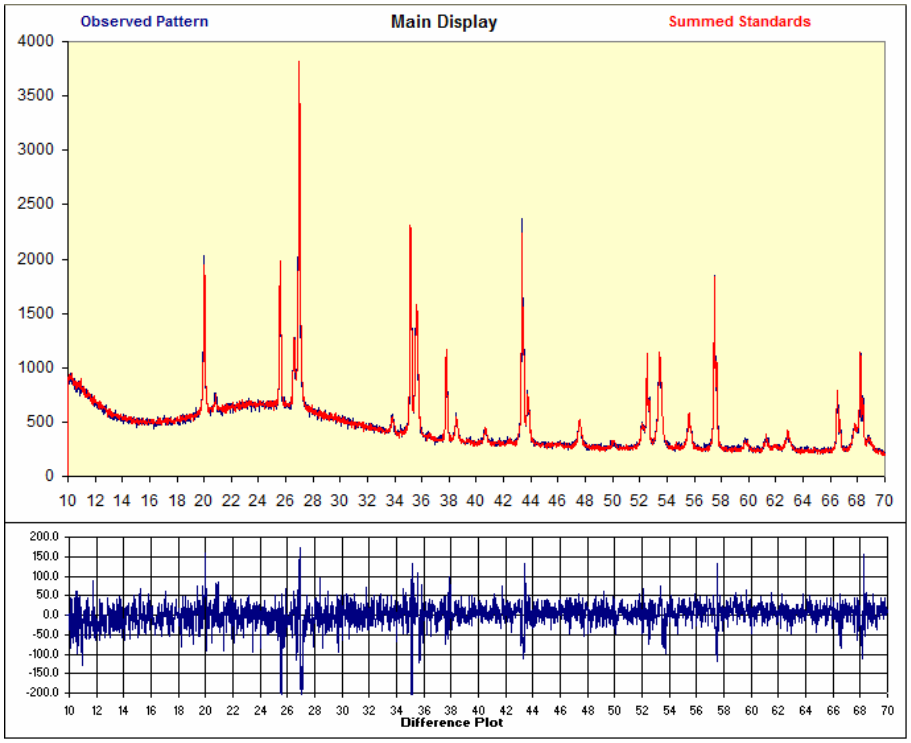

Figure 3.6: Fullpat graphical fit of *adhoc* mixture spiked with Aldrich annealed αAl_2O_3.

The final results (bottom line of Table 3.4), show an overestimation (1.5 wt.%) of the zircon content. It is important to say that Fullpat approach, that is strongly dependent on similarity of the Full Width Half Maximum (FWHM) of the library pattern and of the same phase in the mixture, can be more problematic to apply real sanitary-ware glaze. In this case, in fact, the starting mixture is heated at about 1200°C, causing the annealing of the original zircon, and the consequent decrease in its FWHM. The use of a calcined zircon in the Fullpat library might help.

	SRM 676a α-Al_2O_3	SRM 674a ZnO	SRM 674a TiO_2	SRM 674a Cr_2O_3	Aldrich annealed α-Al_2O_3
$RIR_{Z,S}$	3.41	0.84	1.45	2.03	3.97
Zircon wt.% by RIR	10.33	8.17	7.63	8.76	9.20
Zircon wt.% by Fullpat	-	-	-	-	11.50

Table 3.4: Zircon determination on *adhoc* mixture calculated with traditional RIR method and Fullpat approach. In bracket, for each standard, the (hkl) diffraction plane used for calculations. For zircon the (200) plane was always used.

3.4.4 Sample preparation effect

Grinding operations are required to homogenize the sample and also to reduce the particle size of the grains involved in the mixture. Sometimes, to achieve these goals, the quality of the diffraction pattern can be damaged or may be not the same as the one of the original sample. In the present chapter, a significant difference has been observed between a zirconia mortar and a common agate mortar. Zirconia mortar is known to be the ideal one because of its low porosity, hardness, inertness, high density, so it is best to grind hard material and to minimize contamination; on the other side, agate mortar is the most commonly adopted in laboratories, being relatively harder and less porous than a porcelain mortar. It is important to underline that manual grinding, even if applied by the same operator, can be different during the entire grinding time and also can be different between the two mortar. For example, the applied strength can be different during the entire grinding time and influenced by the handgrip of the pestle. Again the difference in hardness between the particle involved in the mixture and between them and the mortar could influence the efficiency of grinding. The operation can be more subtle than usually thought, especially if a good accuracy is required. It is well known that long grinding times can damage the quality of the sample (and the diffraction pattern in turn) by decreasing peak intensity and by broadening the peak but, in general, the integrated intensity should be the same (and therefore the QPA results). In these cases, the problem can be solved paying more attention to profile fitting in Rietveld refinement and to the extraction procedures of integrated area for traditional RIR internal standard method. In order to compare the samples with different mortars and different grinding time, two methods were applied: RIR-Rietveld and classical RIR. The results are complemented by some observations on the FWHM of zircon and internal standard peaks. The discussion is simplified by presenting the results, for each internal standard, as a function of grinding time.

1. NIST SRM 676a (α-Al_2O_3). Table 3.5 shows the results for both mortars. The comparison between RIR-Rietveld and RIR method shows a disagreement in terms of absolute zircon quantity, probably because of the amorphous presence in zircon (not taken into account in RIR method), but a good agreement has been reached in terms of increasing/decreasing variations of zircon.

	Zircon with NIST 676a	2 min	12 min	22 min
Zirconia mortar	RIR-Rietveld	8.70(4)	8.91 (5)	8.45 (5)
	RIR	10.33	10.77	10.22
	FWHM zircon (°2θ)	0.121	0.122	0.127
	FWHM NIST 676a (°2θ)	0.085	0.083	0.087
Agate mortar	RIR-Rietveld	8.71 (5)	8.85 (6)	8.51 (5)
	RIR	10.38	10.75	10.20
	FWHM zircon (°2θ)	0.125	0.121	0.130
	FWHM NIST 676a (°2θ)	0.084	0.080	0.095

Table 3.5: QPA results and peak broadening details of *adhoc* mixture with NIST 676a (α-Al_2O_3) as internal standard by varying grinding strategy. Data have been obtained by means of Equation 3.6 with Brindley correction and amorphous contents obtained by Cline et al., 2011.

In general one can say that the zircon amount is almost constant as a function of the grinding time. In terms of peak damaging a slight increase of zircon and corundum FWHM has been observed. Some laser scattering measurements have been performed on these samples and are shown in Figure 3.7. The grinding time effect is present in both sample: if the grinding time is increased the cumulative curve moves to smaller particle size, this effect is more evident for particles larger than 10 μm.

Particles with this size correspond to glass particles because zircon and NIST SRM676a are extremely fine, as shown in Table 3.1, so we are in the condition to apply Equation 3.8, using $\sim$20 μm as r_1 value. An

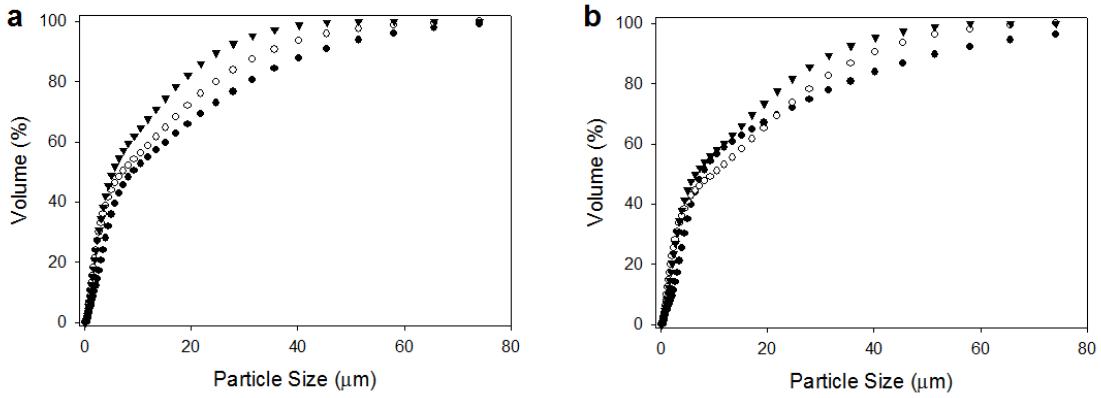

Figure 3.7: Cumulative particle size distribution curve of *adhoc* mixture with NIST SRM 676a (α-Al_2O_3) as internal standard, grinded for 2 min (black circles), 12 min (white circles) and 22 min (black triangles) in a zirconia mortar (a) and in an agate mortar (b).

assessment of grinding effect on zircon particle has been performed by image processing of backscattered images: the comparison between *adhoc* mixture grinded for 2 min in agate mortar and the same sample grinded for additional 10 min showed that mean zircon diameter moves from 1.58 ($\pm$ 0.02) μm to 1.50 ($\pm$ 0.05) μm. This is a further evidence that grinding procedure does not strongly affect the final zircon particle size. Zirconia mortar seems to be more efficient than agate one because, in the 19.348 - 136.397 μm range; in fact, after 22 min, the former abates the glass volume % up to 37.4 while the latter only up to 46.1 %. If this data is converted into glass volume % loss from 0 to 22 min, within the same particle size distribution range, you get a result of 16.3 % for zirconia mortar and 7.7 % for agate mortar.

2. NIST SRM 674a (ZnO). QPA results using zincite as internal standard with different mortar and grinding time are represented in Table 3.6.

	Zircon with NIST 674a (ZnO)	2 min	12 min	22 min
Zirconia mortar	RIR-Rietveld (a)	8.97 (6)	8.41 (5)	8.45 (5)
Zirconia mortar	RIR-Rietveld (b)	9.08 (6)	8.52 (5)	8.56 (5)
	RIR	8.17	7.93	7.87
	FWHM zircon (°2θ)	0.118	0.123	0.127
	FWHM NIST 676a ZnO (°2θ)	0.076	0.083	0.133
Agate mortar	RIR-Rietveld (a)	7.79 (5)	7.58 (6)	7.41 (5)
Agate mortar	RIR-Rietveld (b)	7.90 (5)	7.68 (6)	7.51 (5)
	RIR	7.95	7.81	7.45
	FWHM zircon (°2θ)	0.117	0.129	0.124
	FWHM NIST 674a ZnO (°2θ)	0.082	0.211	0.296

Table 3.6: QPA results and peak broadening details of *adhoc* mixture with NIST 674a (ZnO) as internal standard by varying grinding strategy. Data have been obtained by means of Equation 3.6 with Brindley correction and amorphous contents obtained with Cu-anode (a) and ID31 (b) data.

RIR-Rietveld results are not affected by the slight differences in amorphous content determinations performed with Cu-anode and ID31 data; their discrepancy is less than 0.2 wt.%. The most impressive difference is that grinding time strongly affect the FWHM of ZnO peaks and the effect is larger for agate mortar (Figure 3.8 shows an example of ZnO peak broadening).

On the other side, zircon peaks do not change their shape. Another important effect is that zircon content, differently from sample with NIST SRM 676a as the internal standard, is not constant but is affected by a

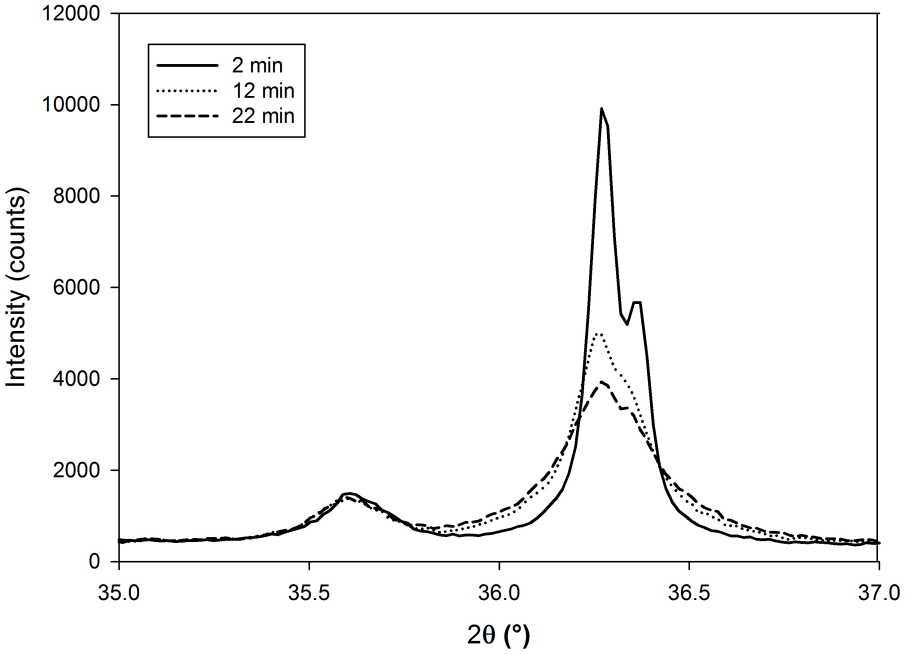

Figure 3.8: Zincite (101) peak broadening effect in *adhoc* mixture grinded with agate mortar for 2, 12 and 22 min.

decreasing trend if grinding time is increased. This "underestimation effect" is present for both mortar and is confirmed by traditional RIR method even with slight difference in the absolute zircon content between the two method (the discrepancies range between 0.5 and 1 wt.%). A well noticeable difference is present between zirconia and agate mortar: the former provides results very close to the expected zircon amount, while the latter presents a significative underestimation of zircon. As for NIST SRM 676a, a particle size analysis, with zirconia mortar, in the particle size range 19.348 - 136.397 μm, has been performed and shows a glass volume % of 49.2 after 22 min of grinding, corresponding to a volume loss from 0 to 22 min of 6.7 %. If compared with NIST SRM 676a results, these two values show that there is a slight grinding effect in the range 19.348 - 136.397 μm if NIST SRM 674 ZnO is adopted; this effect can be explained by the lower hardness of zincite with respect to corundum.

3. NIST SRM 674a (TiO_2). QPA results using rutile as the internal standard with different mortar and grinding time are represented in Table 3.7.

   Zircon quantity obtained by RIR-Rietveld method with Cu-anode amorphous determination is $\sim$ 0.5 wt. % larger than the one obtained with ID31 amorphous determination, due to the different amorphous determination in rutile between both apparata. Differences between zirconia and agate results, as with NIST SRM 674a (ZnO), are still present, especially for short grinding time whilst if grinding time is increased the results tend to converge. The comparison between RIR-Rietveld and RIR results shows a constant zircon underestimation of traditional RIR of about 1-1.5 wt.% with respect to the results obtained with RIR-Rietveld. The FWHM of zircon and TiO_2 coherently increase with grinding time and this trend seems to be more evident for TiO_2 if agate mortar is adopted, maybe because TiO_2 is softer than zircon. However, no correlations seem to be present between the zircon decreasing trend and the change in peaks FWHM. Particle size analysis within the range 19.348 - 136.397 μm shows a 43.3 volume % after 22 min of grinding time and a volume loss of 10.8 % from 0 to 22 min of grinding time. These two values are intermediate respect the ones concerning NIST SMR 676a and NIST SRM 674a (ZnO) and are coherent with the hardness of rutile

	Zircon with NIST 674a (TiO_2)	2 min	12 min	22 min
Zirconia mortar	RIR-Rietveld (a)	9.16 (6)	8.35 (5)	8.38 (5)
Zirconia mortar	RIR-Rietveld (b)	8.61 (6)	7.85 (5)	7.88 (5)
	RIR	7.63	6.55	6.51
	FWHM zircon (°2θ)	0.127	0.131	0.134
	FWHM NIST 676a TiO_2 (°2θ)	0.085	0.088	0.095
Agate mortar	RIR-Rietveld (a)	8.44 (5)	8.57 (6)	8.55 (5)
Agate mortar	RIR-Rietveld (b)	7.94 (5)	8.06 (6)	8.04 (5)
	RIR	6.77	6.92	6.98
	FWHM zircon (°2θ)	0.121	0.129	0.130
	FWHM NIST 674a TiO_2 (°2θ)	0.082	0.090	0.098

Table 3.7: QPA results and peak broadening details of *adhoc* mixture with NIST 674a (TiO_2) as internal standard by varying grinding strategy. Data have been obtained by means of Equation 3.6 with Brindley correction and amorphous contents obtained with Cu-anode (a) and ID31 (b) data.

that is higher than zincite and lower than corundum.

4. NIST SRM 674a (Cr_2O_3). QPA results using NIST SRM 674a (Cr_2O_3) as the internal standard with different mortar and grinding time are again different (see Table 3.8).

	Zircon with NIST 674a (Cr_2O_3)	2 min	12 min	22 min
Zirconia mortar	RIR-Rietveld (a)	9.25 (6)	8.27 (5)	8.19 (5)
Zirconia mortar	RIR-Rietveld (b)	8.64 (6)	7.72 (5)	7.64 (5)
	RIR	8.78	7.80	7.86
	FWHM zircon (°2θ)	0.1178	0.1201	0.1274
	FWHM NIST 676a Cr_2O_3 (°2θ)	0.0796	0.0789	0.0802
Agate mortar	RIR-Rietveld (a)	8.29 (5)	8.22 (6)	8.17 (5)
Agate mortar	RIR-Rietveld (b)	7.75 (5)	7.68 (6)	7.63 (5)
	RIR	7.77	7.91	7.66
	FWHM zircon (°2θ)	0.1168	0.1286	0.1371
	FWHM NIST 674a Cr_2O_3 (°2θ)	0.0739	0.0830	0.0870

Table 3.8: QPA results and peak broadening details of *adhoc* mixture with NIST 674a (Cr_2O_3) as internal standard by varying grinding strategy. Data have been obtained by means of Equation 3.6 with Brindley correction and amorphous contents obtained with Cu-anode (a) and ID31 (b) data.

Like for NIST SRM 674a (TiO_2), zircon quantities obtained by RIR-Rietveld method taking into account both amorphous determinations in NIST SRM 674a (Cr_2O_3) are different by about 0.6 wt.%. As for the previous samples, a zircon decreasing trend has been observed if grinding time is increased, particularly with the use of zirconia mortar, and it is confirmed by the comparison between RIR-Rietveld and RIR results. Again, this trend cannot be related with the differences in FWHM: in fact, if zirconia mortar is used, there are larger differences in zircon content and smaller differences in peaks FWHM than if agate mortar is used. Traditional RIR method provided results that are very similar to RIR-Rietveld and a confirmation of the zircon decreasing trend. Cr_2O_3 is harder than ZnO and TiO_2 and consequently, the variation in FWHM are smaller. After 22 min of grinding time, for the fixed particle size range 19.348 - 136.397 μm, the glass volume % is 40.1 and the loss of glass from 0 to 22 min is 15.3 %. These values are close to the values obtained for NIST SRM 676a and are coherent with the similar hardness of corundum and eskolaite.

5. Aldrich annealed (α-Al_2O_3). QPA results using annealed Aldrich (α-Al_2O_3) as internal standard with different mortar and grinding time are shown in Table 3.9. As for NIST SRM 674 (ZnO), RIR-Rietveld results

are not affected by the slight differences in amorphous content determinations performed with Cu-anode and ID31 data.

	Zircon with Aldrich annealed (α-Al_2O_3)	2 min	12 min	22 min
Zirconia mortar	RIR-Rietveld (a)	9.53 (6)	9.10 (5)	8.94 (5)
Zirconia mortar	RIR-Rietveld (b)	9.57 (6)	9.14 (5)	8.98 (5)
	RIR	9.20	7.92	7.63
	FWHM zircon (°2θ)	0.120	0.122	0.129
	FWHM Aldrich annealed (α-Al_2O_3) (°2θ)	0.057	0.055	0.057
Agate mortar	RIR-Rietveld (a)	9.39 (5)	8.66 (6)	8.67 (5)
Agate mortar	RIR-Rietveld (b)	9.43 (5)	8.69 (6)	8.71 (5)
	RIR	8.79	7.53	7.98
	FWHM zircon (°2θ)	0.124	0.126	0.124
	FWHM Aldrich annealed (α-Al_2O_3) (°2θ)	0.054	0.058	0.058

Table 3.9: QPA results and peak broadening details of *adhoc* mixture with Aldrich annealed (α-Al_2O_3) as internal standard by varying grinding strategy. Data have been obtained by means of Equation 3.6 with Brindley correction and amorphous contents obtained with Cu-anode (a) and ID31 (b) data.

Zircon decreasing trend is confirmed for both mortars, and, for 12 and 22 min, zircon content is lower in zirconia mortar than in agate mortar. Peaks FWHM show a slight increase but the values are comparable between the two different mortars. Figure 3.9 is an example of the difference in zircon (002) intensity that has been observed in the different internal standard and that corresponds to a decreasing trend of zircon in RIR-Rietveld and traditional RIR methods.

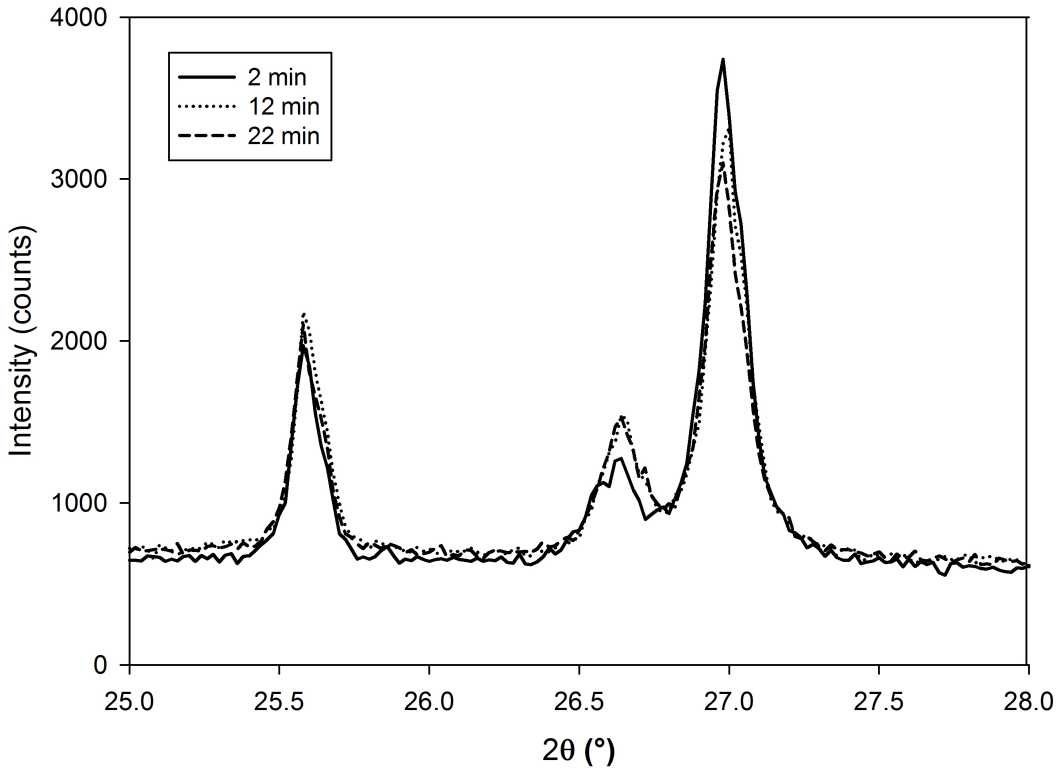

Figure 3.9: Example of zircon (002) peak, located at about 27°2-θ, loss of intensity if grinding time is increased using agate mortar. Note that the corundum (012) peak, located at about 25.5°2-θ, exhibits approximately the same intensity.

No glass volume % analysis, in the range 19.348 - 136.397 μm, has been performed because the higher particle size of annealed Aldrich (α-Al_2O_3) does not satisfied the condition explained in Section 3.2.3 because a small volume of its particle is bigger than 19.348 μm.

If grinding time is increased a more or less marked peak broadening was observed for all phases involved but, this effect, as already mentioned, should not generally modify the peaks integrated area and then the QPA results. However, in the *adhoc* mixture, both peak broadening and differences in QPA results have been observed in terms of zircon amount. Reasonably, if differences in integrated area peak ratio (i.e. between zircon and the adpoted internal standard) are present, this could be due to a preferred loss/contamination of particle belonging to a phase or to loss of crystallinity of a phase caused by grinding. Considering Equation 3.6, a zircon decreasing trend during grinding operations is compatible with i) a loss of zircon ii) a contamination of internal standard or iii) a zircon "amorphization". A contamination with internal standard is unrealistic but the other two possibilities are not unlikely. At the moment I am not able to explain the observed loss of zircon in the different cases, but we can state that this loss of zircon is present because of the agreement in decreasing trend of zircon with RIR-Rietveld and traditional RIR methods. Moreover, if the internal standard and the grinding time are fixed, we observed a higher zircon content if zirconia mortar is adopted, in agreement with the best properties of zirconia mortar. Finally, two very interesting effect of internal standard from 2 to 22 min of grinding time has been observed. At first, a strong effect on the glass fraction (particle size range 19.348 - 136.397 μm) during grinding has been observed. In fact, for NIST SRM 676a and NIST SRM 674a, a correlation between the internal standard hardness and the glass volume % has been observed, as shown in Figure 3.10, suggesting that, even if extremely finer than the glass fraction, the internal standard has a grinding role in the mixture.

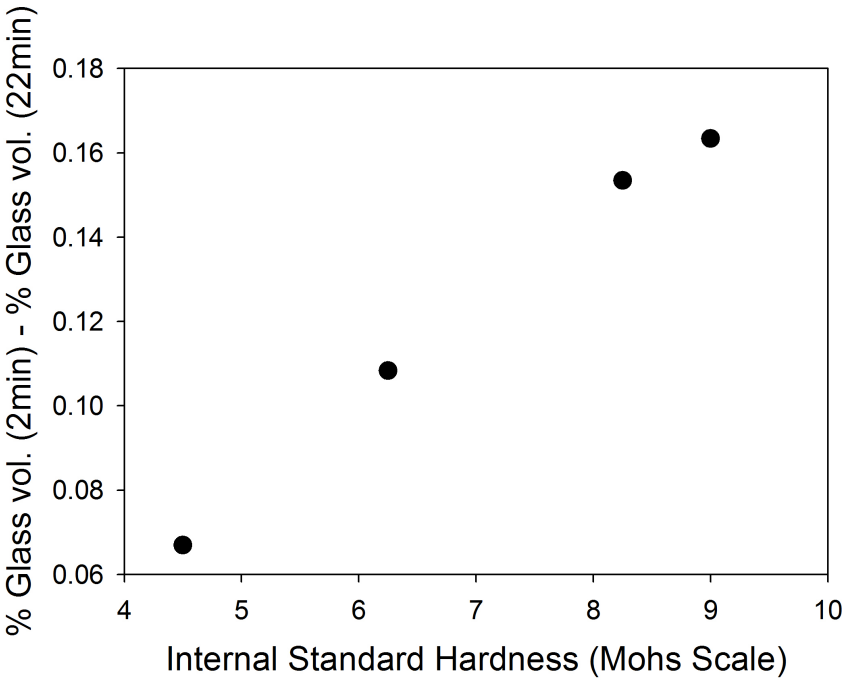

Figure 3.10: Correlation between the loss of glass volume in the 19.348 - 136.397 μm range and the hardness of the different adopted internal standards. Note that Aldrich annealed (α-Al_2O_3) was not considered because its particle size distribution curve includes particles bigger than 19.348 μm.

Afterwards, the different hardness of internal standard is related to the difference in FWHM of internal standard peak after 22 min of grinding time and FWHM of internal standard after the first step of grinding time. This effect has been observed in both mortar and is very prominent for NIST SRM 674a ZnO as proven by Figure 3.11.

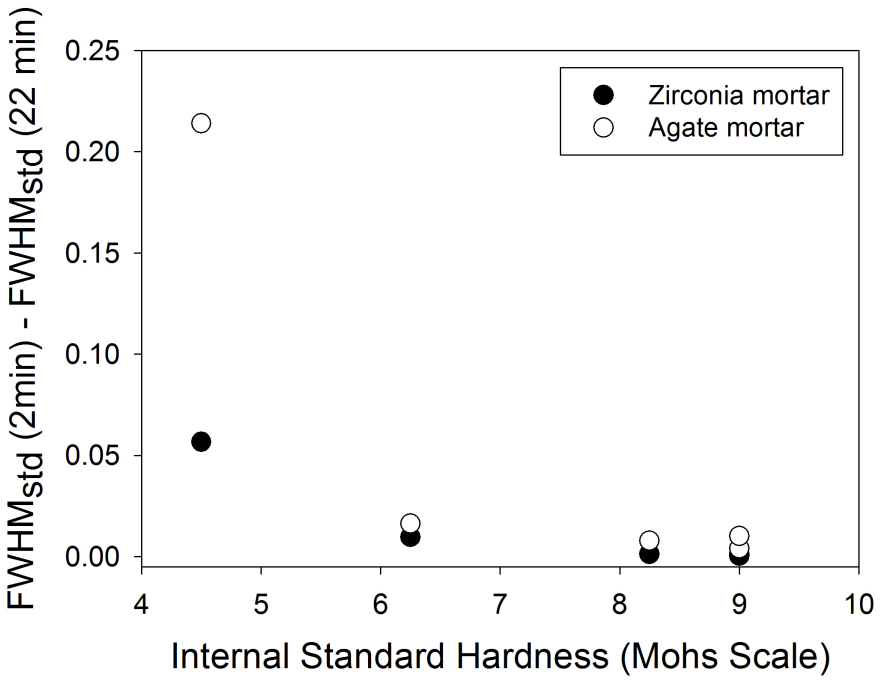

Figure 3.11: Correlation between the internal standard hardness and the peak broadening effect if grinding time is increased. Black circles correspond to *adhoc* mixtures grinded in zirconia mortar, white circles correspond to *adhoc* mixtures grinded in agate mortar.

No similar correlation has been observed in terms of difference in FWHM of zircon peaks from 2 to 22 min of grinding time.

3.4.5 QPA sensitivity to small differences in zircon amount

The responsiveness of all the different internal standards to small addiction of zircon is treated in this section. It must be observed that the decreasing trends in zircon content observed in section 3.4.4 is a primary evidence of the sensitivity of Rietveld and traditional RIR to small differences in zircon content, even if it was not expected and even if it is not easy to justify. Furthermore, the addiction of zircon in all *adhoc* mixtures can be a valid proof to better observe this effect. So, for each *added* mixture, the expected zircon amount has been calculated following Equation 3.9 but replacing the 0.1 value with the zircon amounts calculated in section 3.4.4 after grinding for 22 min in zirconia mortar. For example, in the case of *added* mixture with NIST SRM 676a, 0.1 must be replaced by 0.0845, in agreement with Table 3.5. The results obtained are shown in Figure 3.12. Discrepancies between expected zircon and calculated zircon have been calculated considering: i) Cu-anode data on *added* mixture and correcting them for amorphous determinations based on Cu-anode data (black circles), ii) Cu-anode data on *added* mixture and correcting them for amorphous determinations based on ID31 data (white circles), and iii) ID31 data on *added* mixture and correcting them for amorphous determinations based on ID31 data (black triangles).

In all three cases, a good agreement is present between the expected and the calculated zircon; not only, results obtained with Cu-anode data and corrected for amorphous determination based on Cu-anode data (black circles) are less dispersed and closer to the expected value estimated with Equation 3.9 (ideal null discrepancy), than the other two (white circles and black triangles) Thus, for these samples, if proper correction are considered, also Cu-anode data can provide good accuracy.

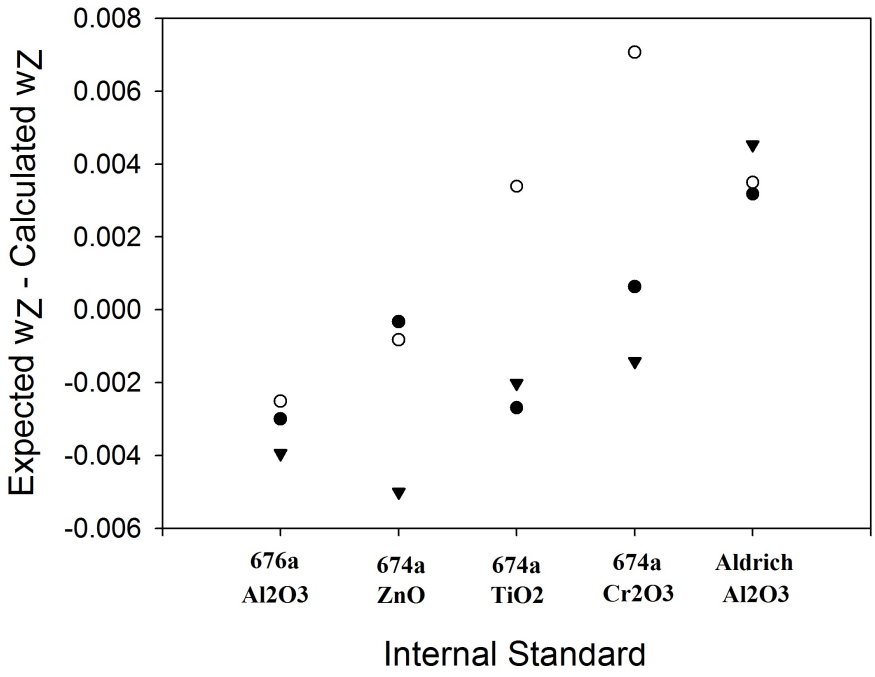

Figure 3.12: Comparison between the difference in expected zircon amount (calculated with Equation 3.9) and the calculated zircon amount (calculated with Equation 3.6). Symbols description is in the text.

3.5 Conclusions

All the internal standard and the industrial grade zircon contain a not negligible amorphous content. Zircon quantification in *adhoc* mixture resulted accurate for all the adopted internal standard favored by i) the small particle size of involved phases tent to minimize microabsorption effect, and ii) by the application of Equation 3.6 instead of Equation 3.2, which corrects the results for the amorphous amounts within standards. However, it was observed that the most accurate zircon quantification was obtained with NIST SRM 676a and NIST SRM 674a (ZnO).

Care must be taken in the sample preparation procedure: zirconia mortar and a not too long grinding time are fundamental, allowing one to avoid zircon underestimation. Again, if one is aimed at a faster but less accurate zircon determination, RIR traditional method and Fullpat approach are able to satisfy this request. They also maintain a good sensitivity to small zircon variations, as remarked by their agreement with RIR-Rietveld method, if grinding time is increased. Finally, the comparison between Cu-anode and ID31 results on *added* mixtures are very close, pointing out that an accurate zircon quantification can be reached also with a laboratory apparatus.

Part III

Local Structure of Si-Al-Ca-Na-O Glasses

Chapter 4

Local Structure of Si-Al-Ca-Na-O Glasses

4.1 Introduction

In the last decades, amorphous materials increased their importance as many functional materials and many dielectrics are nanocrystalline or amorphous [Wallace & Wilk, 2003]. An amorphous component is almost always present in ceramic production, as shown in Chapter 1 and 2, influencing the properties of the whole material. In particular, in this chapter, great attention is paid to the amorphous component of sanitary-ware glazes that can get to be even the 90 wt. %. The coating has more than just an aesthetic role and has to fulfill certain technological features. Mostly, glazes have to perfectly adhere to the underlying material, shrinking upon cooling in the same way as the ceramic support in order to avoid the formation of cracks and the development of detachment phenomena. In Chapter 2, the importance of some chemical elements (i.e. silicon, calcium but also sodium and potassium) on glass transition (T_g) and softening (T_s) temperatures has been observed. Variation in composition and structure play a control role on strength of chemical bonding and, in turn, the thermal expansion behavior is affected [Konijnendijk & Stevels, 1976]. The flexibility of chemical bonds and, therefore, the amplitude of thermal vibration, are influenced by such chemical variations, by the coordination number within the polyhedra and by the bond angles between atoms [Fluegel, 2010].

Due to their intrinsic disorder, the structure of these materials requires a different approach from the long-range ordered crystalline material. Molecular dynamics calculations or Monte Carlo simulation are widely used to comprehend the myriad of interatomic configurations and structural properties of the system but these methods suffer from the limitation that their results will be strongly affected by the prior assumption made in the choice of interatomic potentials and by the absence of measured data. Experimentally, one can access the real structural information by total scattering techniques [Bowron, 2008], X-ray absorption fine structure spectroscopy (EXAFS) [Greaves, 1985] or nuclear magnetic resonance (NMR) [Benoit et. al, 2005] even if, the N/(N+1) number of pairwise interactions between the N number of atomic species gives rise to complications in the data modeling. In the present thesis, total scattering is the way selected to achieve this purpose and both X-ray and neutron data were collected in order to improve the effectiveness of this approach. X-ray photons do not have charge and have a strong interaction with the electron density, even though this interaction becomes weaker moving towards smaller interatomic distances due to the Debye-Waller factor effect.

Neutrons are neutral particles with a mass of 1.674928×10^{-27} kg that are unaffected by the charge of the orbital electrons and that interact with the nucleus of the atom via the strong nuclear force even if it acts only at short distances with a consequent weak signals. This offers the advantage of deep penetration (i.e. centimeters in aluminum) which enables to probe the bulk properties of a materials but has the drawback of large sample require-

ment. Their interaction with nuclei makes them very useful if isotopes are present, and being not monotonically sensitive to atomic number,they better distinguish elements with a very close number of electron, differently from X-rays [Sivia, 2011]. To obtain good real space resolution to be able to discriminate between pairwise correlations of atoms of quite similar size and to minimize Fourier transform artifacts, it is necessary to have scattering data to a high momentum transfer Q (Q is equal to $4\pi \sin\theta/\lambda$, where 2θ is the scattering angle and λ is the wavelength of the incident radiation), usually larger than 20 Å^{-1} but ideally larger than 30-35 Å^{-1}. This means that the experiments should be performed with large scale facilities [Sivia, 2011] because, for example, an ordinary X-ray diffractometer with copper radiation can reach only a momentum transfer value of 8 Å^{-1}. Synchrotron (for X-rays) and reactor or spallation source (for neutrons) are ideal and they also provide high flux radiation, minimizing time requirement for data collection and improving the counting statistics. For neutrons, during a total scattering experiment, the interference differential cross section, or total structure factor, *F(Q)* is obtained, as defined by Equation 4.1:

$$F(Q) = \sum_{\alpha\beta}(2-\delta_{\alpha\beta})c_\alpha c_\beta b_\alpha b_\beta [S_{\alpha\beta}(Q)-1] \tag{4.1}$$

where $c_\alpha, c_\beta, b_\alpha, b_\beta$ are the atomic fractions and neutron scattering lengths of each type of atom in the sample, and $\delta_{\alpha\beta}$ is the Kronecker δ function to avoid double counting the interactions between like species, and Q is the magnitude of the momentum transfer vector in the scattering process. In the case of X-ray data, neutron scattering length are replaced by atomic form factor, which depend not only from the chemical element but also from the λ and θ. The partial structure factors $[S_{\alpha\beta}(Q)-1]$ are summed together (with $c_\alpha, c_\beta, b_\alpha, b_\beta$ weighting them), to give the total *F(Q)* in 4.1). The partial structure factors are related to the partial pair distribution function *g(r)* by a sine Fourier transform, as shown in 4.2:

$$g_{\alpha\beta}(r) - 1 = \frac{1}{(2\pi)^3\rho}\int_0^\infty 4\pi Q^2 [S_{\alpha\beta}(Q)-1]\frac{\sin Qr}{Qr}\,\mathrm{d}Q \tag{4.2}$$

where ρ is the atomic density of the sample. Like the total structure factor $F(Q)$, the total pair distribution function $g(r)$ is simply the weighted sum of all the partial $g_{\alpha\beta}$*(r)*, described in 4.2. These functions describe the probability of an atom of type β to be in a coordination shell at a distance *r* from an atom of type α. A total scattering experiment is therefore able to provide, through the described functions, a description of the structure in an amorphous material. The achievement of these information passes through a proper data correction procedure and data treatment approach.

The aim of this investigation is to access the local structure of amorphous samples with a composition similar to the glass in sanitary-ware glazes (see Table 2.1). Having in mind the wide chemical variability of sanitary-ware glazes and to the consequent large number of pairwise interactions, it was necessary to choose a set of simplified compositions. In particular, only silicon, aluminum, calcium, sodium and oxygen species have been selected because they are the main diffused elements in glaze formulation. The experimental approach consists in coupling neutron and X-ray high-energy data, correcting them with Gudrun software [Soper, 2010a] and then modeling them in an Empirical Potential Structure Refinement type approach [Soper, 2010b]. It will be especially interesting, for calcium and sodium, to experimentally check their charge compensating or network modifying role within the structure, with subordinate effects on the degree of polymerization. This information can then be directly compared with the results obtained by means of EXAFS and molecular dynamics simulations [Cormier &

Neuville, 2004], and by means of molecular dynamics only [Cormack & Du, 2001].

Silicon is a network forming element, thus it is expected to be an element that encourages the polymerization of the network through the formation of chains of tetrahedra. Bowron, in 2008, modeled with EPSR the silica glass structure on the basis of neutron scattering data to study its local and intermediate range structural veracity. The validity of this model was tested versus X-ray diffraction and EXAFS: for each technique, a signal was calculated starting from the EPSR results and a reasonable match was obtained with experimental data from literature. Thus, the model generated by EPSR based on neutron data provides a good representation of silica structure. The results show that the first peak in $g_{Si-O}(r)$ is at about 1.6 Å, that correspond to a 3.9 oxygen atoms around each silicon atoms, if one considers a radial distance of 2.5 Å, as shown in Figure 4.1 (part a); this value is coherent with the typical tetrahedral coordination of silicon.

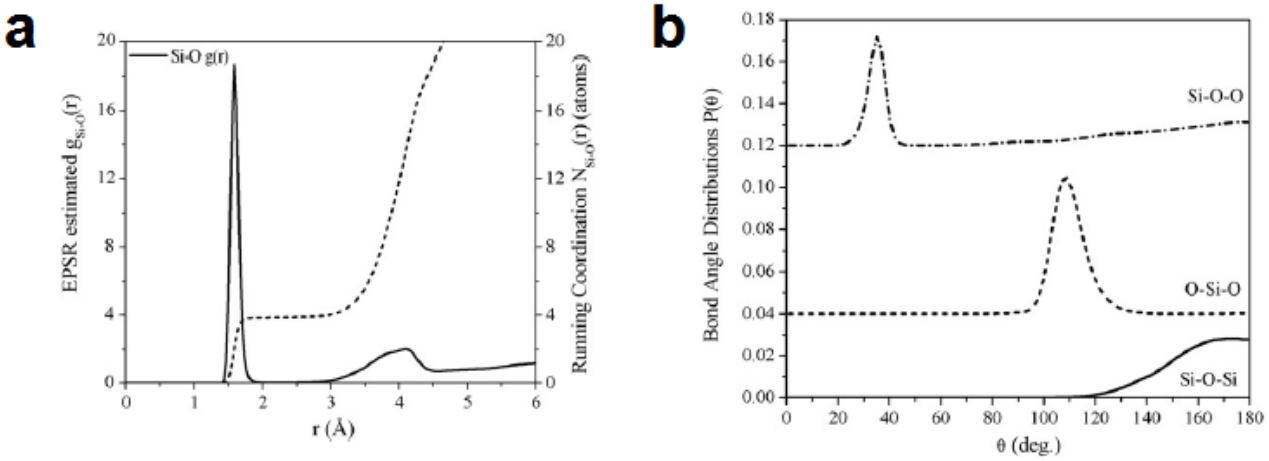

Figure 4.1: Part a: the EPSR estimated g_{Si-O} (solid line) and running coordination number N_{Si-O} (dashed line). Part b: probability angular distribution function for near neighbor Si-O-Si (solid line), O-Si-O (dashed line) and Si-O-O (dashed-dotted line).

The coordination number is directly related with partial pair distribution function $g_{x-y}(r)$ by a simple integration as described in Equation 4.3:

$$N_{x,y} = \int_a^b g_{x,y}(r)dr \tag{4.3}$$

where *a* and *b* are the minimum and maximum limits of the coordination shell, *x* is the chemical species in the center of the shell, whereas *y* is the chemical species surrounding *x*. Moreover, by looking at part b of Figure 4.1, the tetrahedral arrangement of silicon is confirmed by the bond angles probability distribution $P(\theta)$. For example, the O-Si-O arrangement is centered at about 109°, with a more or less pronounced broadening due to the disordered nature of glass.

Okuno et al., in 2005, studied the progressive introduction of Al_2O_3 in aluminosilicate-glass structure with X-ray powder diffraction. The most straightforward effect is that first peak in *g(r)* moves to higher values, as shown by the radial pair distribution function of Figure 4.2 (part a). In particular, it is centered at 1.66 Åif the molar fraction of Al_2O_3 is 0.25, and reaches up the value of 1.76 Å for an Al_2O_3 molar fraction of 0.60. These results have been explained by the presence of some five-fold and six-fold coordinated aluminum atoms. Silicon should maintain its four-fold typical coordination at ambient conditions.

Karlsson et al., in 2005, investigated mixed alkali/alkaline-earth silicate glasses from neutron diffraction and

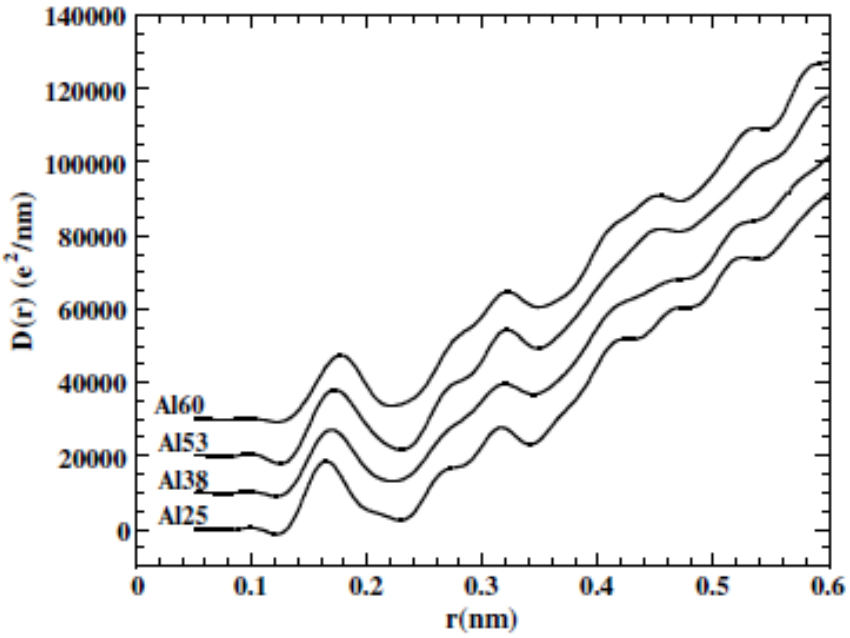

Figure 4.2: Radial distribution function, D_r, curves of aluminosilicate glasses as function of the increased molar fraction of Al_2O_3.

vibrational spectroscopy. The introduction of sodium and calcium in the silica is evidenced by the appearance of a 2.25 Å centered peak in the pair distribution function. Calcium and sodium are dispersed in the Si-O network and their coordination numbers (calculated up to 2.4 Å) are 1.8 ($\pm$ 0.0.4) and 1.7 ($\pm$ 0.0.3), respectively. The full replacement of sodium and calcium with strontium moves the 2.25 Å peak in pair distribution function to 2.6 Å, due to the higher ionic radius of strontium.

4.2 Experimental Procedure

4.2.1 Samples preparation

Three different Si-Al-Ca-Na-O glasses have been prepared following the common industrial formulation of sanitary-ware glaze practice. The SiO_2/Al_2O_3 molar ratio was fixed at 10.2 (6 in weight %), a CaO molar fraction of about 0.07 and Na_2O molar fractions of 0.06, 0.09 and 0.12. These compositions are summarized in Table 4.1.

sample	silicon		aluminium		calcium		sodium		density
	SiO_2	A.F.	Al_2O_3	A.F.	CaO	A.F.	Na_2O	A.F.	g cm^{-3}
A	0.78	0.25	0.08	0.05	0.08	0.04	0.06	0.04	2.49
B	0.73	0.23	0.07	0.04	0.08	0.03	0.12	0.08	2.56
C	0.68	0.21	0.07	0.04	0.07	0.03	0.18	0.12	2.62

Table 4.1: Chemical composition of the three sample expressed as molar fraction and atomic fraction (AF). Note that the AF fraction have been used to directly obtain the number of atoms to put in the simulating box.

Samples were obtained by carefully weighing the appropriate amounts of different reagents (quartz SiO_2 from Sigma-Aldrich (purum, $\geq$ 95 %), alumina Al_2O_3 from Sigma-Aldrich (99.7 %), calcium carbonate $CaCO_3$ from Analar (99.5 %), and sodium carbonate Na_2CO_3 from Analar (99.9 %)) and mixing together in an agate mortar. Each composition was placed in a platinum crucible and heated up to 1200°C in a static kiln for about 30 min. This

resulted sufficient to fully melt the powder. The crucible was then quenched in water to obtain a fully amorphous material. X-ray diffraction measurements by means of the PANalytical X'Pert PRO diffractometer (described in Section 1.2.4) showed that all samples did not contain any crystalline phase (see Figure 4.3).

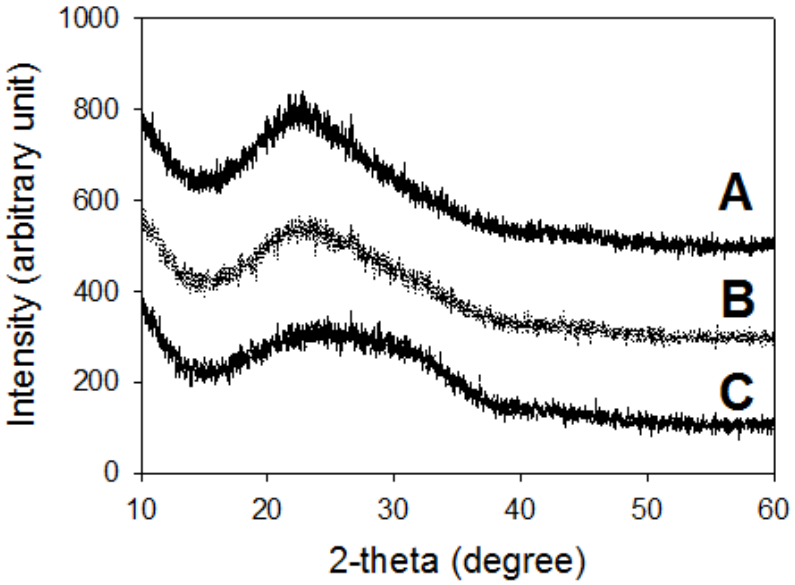

Figure 4.3: X-ray diffraction patterns of three sample collected with copper radiation. The total absence of Bragg peak exclude the presence of any crystalline phase.

Density measurements, required for total scattering data treatment and modeling, have been performed with a Quantachrome micropycnometer and the results can be found in Table 4.1.

4.2.2 Neutron and X-ray data collection

Neutron diffraction data have been collected over the wavelength range of 0.05-4.95 Å at the SANDALS beamline, located at the ISIS spallation source in Chilton (UK), that provides to access the glass total structure factor scattering vector (Q) range from 0.2 to 50 $Å^{-1}$. SANDALS diffractometer was built in 1989 and completely refurbished in 2005 and has in liquids and amorphous material its more suitable targets by combining an intense pulsed radiation and a large number of detectors at low angle. The beamline uses liquid methane at 110 K as moderator, an incident flight path of 11 m and a final flight path from 0.75 to 4 m, before the neutrons reach the 633 ZnS scintillation detectors. The most straightforward capabilities of a time of flight source is that each single detector is able to collect a single diffraction pattern because, differently from synchrotron and reactor sources, θ is fixed, with all the possible wavelengths of the spallation source. Furthermore, in consideration of De Broglie relation ($\lambda = \frac{\hbar}{mv}$), Bragg's law ($2d_{hkl} \sin\theta = n\lambda$) and linear motion equation (s=vt), the time t at which a neutron with a λ wavelength, diffracted by the *hkl* plane, is collected by the detector, located at θ angle after a total path L, considering the path from source to sample and from sample to detector, is given by Equation 4.4:

$$t = 505.56 L \sin\theta d \tag{4.4}$$

For more details see [Sivia, 2011]. Before data collection, powdered samples are manually pressed into flat TiZr alloy cans (packing fraction of 0.481 and density of 0.0542 atoms $Å^{-3}$), with a diameter of 35 mm and walls

thickness of 1 mm. Each sample has been measured for at least 9 hours to obtain a good signal to noise ratio; than additional shorter measurements (3-6 hours) have been performed on the empty instrument (3 hours), vanadium reference (6 hours), and all the empty cans (3-6 hours).

Complementary X-ray data have been collected with the Ag K_α (λ is 0.559 Å) PANalytical X-Pert Pro diffractometer, equipped with a scintillation detector, available at the ISIS second target station support laboratories. Each sample was collected for 48 hours over a Q range of 0.65-20 $Å^{-1}$.

4.2.3 Data correction

Both neutron and X-ray data have to be normalized and corrected before they can be Fourier transformed to a pair distribution function. In both cases, the Gudrun [Soper, 2010a] software was adopted to apply the necessary procedure. The basic quantity that a scattering experiment aims to measure is the fraction of incident particles that emerges from various directions. This is the differential cross section $\frac{d\sigma}{d\Omega}$ (λ, 2θ) but, unfortunately, this function is not directly measured. However, a diffraction experiment is able to collect the number of particles/photons scattered by that assembly in the same time interval Δt in the wavelength range $\lambda + \Delta\lambda$ into a solid angle $\Delta\Omega$ in the direction 2θ relative to the incident beam direction; let call this CNT (λ, 2θ). This quantity is related to the differential cross section $\frac{d\sigma}{d\Omega}$ (λ, 2θ) by Equation 4.5:

$$\frac{d\sigma}{d\Omega} = \frac{CNT(\lambda, 2\theta)}{N\langle\Phi(\lambda, t)\rangle_t \Delta\lambda\Delta\Omega(2\theta)\Delta t} \tag{4.5}$$

where $\Phi(\lambda, t)$ is the average number of particles of radiation per unit area per unit time per unit wavelength which impinge on an assembly of N atoms. Unfortunately, neutrons and X-rays are not easily quantifiable; moreover, detectors may be affected by problems, with consequent loss of incoming radiation. Again, some physical phenomena like self attenuation (A_s) and multiple scattering (M_s) may affect the measured intensity CNT (λ, 2θ), so, it is not easy to obtain the differential cross section $\frac{d\sigma}{d\Omega}$ (λ, 2θ). For a particular sample s, $\Sigma_s(\lambda,2\theta)$ is equal to $\frac{d\sigma_s}{d\Omega}$ (λ, 2θ) and the measured signal CNT(λ, 2θ) is given by Equation 4.6:

$$CNT_s(\lambda, 2\theta) = (A_{s,s} N_s \Sigma_s(\lambda, 2\theta)) + \langle\Phi(\lambda, t)\rangle_t E_d(\lambda)\Delta\lambda\Delta\Omega(2\theta)\Delta t_s \tag{4.6}$$

If the beam is not passing through a sample, the signal that is collected by the detectors is known as the background signal CNT_b(λ, 2θ) and is given by Equation 4.5:

$$CNT_b(\lambda, 2\theta) = B(\lambda, 2\theta)\langle\Phi(\lambda, t)\rangle_t E_d(\lambda)\Delta\lambda\Delta\Omega(2\theta)\Delta t_b \tag{4.7}$$

where B(λ,2θ) is the background differential cross section. Commonly, samples are included into a container (i.e. glass capillary, metallic container) which has its own scattering behaviour. In that case the attenuation factor for the sample, A_s becomes $A_{s,sc}$ where (s, sc) means "scattering in the sample, attenuation in the sample and container", and that for the container will be $A_{c,sc}$ where (c, sc) means "scattering in the container, attenuation in the sample and container". The multiple scattering will include both sample and container contributions, M_{sc}. Now the measured number of counts becomes CNT_{s+c}(λ, 2θ) and is defined by Equation 4.8:

$$CNT_{s+c}(\lambda, 2\theta) = (A_{s,sc}N_s\Sigma_s(\lambda, 2\theta) + A_{c,sc}N_c\Sigma_c(\lambda, 2\theta) + M_{sc} + B(\lambda, 2\theta))\langle\Phi(\lambda, t)\rangle_t E_d(\lambda)\Delta\lambda\Delta\Omega(2\theta)\Delta t_{sc} \tag{4.8}$$

After this consideration, different measurements are necessary to perform the data correction procedure. In general, these are the main steps that have to be followed:

1. attenuation and multiple scattering corrections. In GudrunN and GudrunX, the attenuation and multiple scattering corrections are calculated in two distinct ways that depend from the sample geometry (cylindrical or flat). For these calculations it is necessary to specify the beam size and position, and the sample chemical composition;

2. deadtime corrections. A τ interval is generally present for each type of detector; this is the time required to resolve two events as two distinct events;

3. data need to be corrected as a function of the number of incident units (neutron or photons). This terms is indicated by $\langle\Phi(\lambda, t)\rangle_t\Delta t$ in Equations 4.6, 4.7 and 4.8 and it is monitored by a detector (monitor) placed in the incident beam which counts for exactly the same time that each sample is counted for. This normalization term is defined as:

$$RAWMON_s(\lambda) = \langle\Phi(\lambda, t)\rangle_t E_m(\lambda)\Delta\lambda\Delta t_s \tag{4.9}$$

where E_m is the monitor detector efficiency. Thus, all collected intensities ($CNT_b(\lambda,2\theta)$, $CNT_c(\lambda,2\theta)$ and $CNT_{c+s}(\lambda,2\theta)$) must be divided by the correspondent RAWMON (λ) measurements. In the case of background, the resultant normalisation is:

$$\begin{aligned} NORMMON_b(\lambda, 2\theta) &= \frac{CNT_b(\lambda, 2\theta)}{RAWMON_b(\lambda)} \\ &= B(\lambda, 2\theta)\frac{E_d(\lambda)}{E_m(\lambda)}\Delta\Omega(2\theta) \end{aligned} \tag{4.10}$$

The same procedure of Equation 4.10 must be applied also for sample container measurement and for sample in container measurement, whose resultant normalization are represented by following Equations:

$$\begin{aligned} NORMMON_s(\lambda, 2\theta) &= \frac{CNT_s(\lambda, 2\theta)}{RAWMON_s(\lambda)} \\ &= A_{s,s}N_s\Sigma_s(\lambda, 2\theta) + M_s + B(\lambda, 2\theta)\frac{E_d(\lambda)}{E_m(\lambda)}\Delta\Omega(2\theta) \end{aligned} \tag{4.11}$$

$$\begin{aligned} NORMMON_{s+c}(\lambda, 2\theta) &= \frac{CNT_{s+c}(\lambda, 2\theta)}{RAWMON_{s+c}(\lambda)} \\ &= A_{s,sc}N_s\Sigma_s(\lambda, 2\theta) + A_{c,sc}N_c\Sigma_c(\lambda, 2\theta) + M_{sc} + B(\lambda, 2\theta)\frac{E_d(\lambda)}{E_m(\lambda)}\Delta\Omega(2\theta) \end{aligned} \tag{4.12}$$

4. normalized data (NORMMON$_s$(λ,2θ) and NORMMON$_{s+c}$(λ,2θ)) are background subtracted following Equation 4.13:

$$SUBBACK_s(\lambda, 2\theta) = NORMMON_s(\lambda, 2\theta) - NORMMON_b(\lambda, 2\theta) \tag{4.13}$$

and Equation 4.14:

$$\begin{aligned} SUBBACK_{s+c}(\lambda, 2\theta) &= NORMMON_{s+c}(\lambda, 2\theta) - NORMMON_b(\lambda, 2\theta) \\ &= (A_{s,sc}N_s\Sigma_s(\lambda, 2\theta) + A_{c,sc}N_c\Sigma_c(\lambda, 2\theta) + M_{sc})\frac{E_d(\lambda)}{E_m(\lambda)\Delta\Omega(2\theta)} \end{aligned} \tag{4.14}$$

5. put the data on an absolute scale. Independently from the adopted radiation, there is a constant that must be determined. In the case of neutrons such constant C (λ, 2θ) is:

$$C(\lambda, 2\theta) = \frac{E_d(\lambda)}{E_m(\lambda)}\Delta\Omega(2\theta) \tag{4.15}$$

For neutrons, there is a material (vanadium) which has a small coherent scattering length and consequently its Bragg peaks are very weak if compared with the single atom scattering. Vanadium is a metal with a known density, is stable, and can be formed into cylinders or flat plates as required. Furthermore, vanadium multiple scattering and attenuation are well defined (so they can be easily calculated from the tabulated values) and it does not require a container. At this point an additional experiment must be performed with the same conditions of the sample one, so the quantity CTN$_v$(λ, 2θ) is measured and it is:

$$CTN_v(\lambda, 2\theta) = (A_{v,v}N_v\Sigma_v(\lambda, 2\theta) + M_v + B(\lambda, 2\theta))\langle\Phi(\lambda, t)\rangle_t E_d(\lambda)\Delta\lambda\Delta\Omega(2\theta)\Delta t_v \tag{4.16}$$

Afterwards, $CTN_v(\lambda, 2\theta)$ is normalized and background subtracted. So, NORMMON$_v$(λ, 2θ) and SUBBAK$_v$(λ, 2θ) are obtained following Equations 4.17 and 4.18:

$$\begin{aligned} NORMMON_v(\lambda, 2\theta) &= \frac{CTN_v(\lambda, 2\theta)}{RAWMON_v(\lambda, 2\theta)} \\ &= (A_{v,v}N_v\Sigma_v(\lambda, 2\theta) + M_v + B(\lambda, 2\theta))\langle\Phi(\lambda, t)\rangle_t E_d(\lambda)\Delta\lambda\Delta\Omega(2\theta)\Delta t_v \end{aligned} \tag{4.17}$$

$$\begin{aligned} SUBBACK_v(\lambda, 2\theta) &= NORMMON_v(\lambda, 2\theta) - NORMMON_b(\lambda, 2\theta) \\ &= (A_{v,v}N_v\Sigma_v(\lambda, 2\theta) + M_v)C_n(\lambda, 2\theta) \end{aligned} \tag{4.18}$$

The term ($A_{v,v}N_v\Sigma_v(\lambda, 2\theta) + M_v$) can be estimated with numerical simulations and divided into the vanadium data:

$$C_n(\lambda, 2\theta)_{estimated} = \frac{SUBBACK_v(\lambda, 2\theta)}{(A_{v,v}N_v\Sigma_v(\lambda, 2\theta) + M_v)_{estimated}} \tag{4.19}$$

6. application of data normalization. Once the appropriate data calibration has been determined, the data are put on an absolute scale of cross section by dividing by this constant. In the case of a sample within a container, it is:

$$\begin{aligned} NORMVAN_{s+c}(\lambda, 2\theta) &= \frac{SUBBACK_{s+c}(\lambda, 2\theta)}{C_n(\lambda, 2\theta)} \\ &= (A_{s,sc}N_s\Sigma_s(\lambda, 2\theta) + A_{c,sc}N_c\Sigma_c(\lambda, 2\theta) + M_{sc}) \end{aligned} \tag{4.20}$$

$$NORMVAN_c(\lambda, 2\theta) = \frac{SUBBACK_c(\lambda, 2\theta)}{C_n(\lambda, 2\theta)} = (A_{c,c}N_s\Sigma_s(\lambda, 2\theta) + M_s) \tag{4.21}$$

7. if multiple scattering and attenuation are present, one can remove them from NORMVAN$_s$, NORMVAN$_{s+c}$ and NORMVAN$_b$. Multiple scattering is removed following Equations 4.22, 4.23 and 4.24:

$$\begin{aligned} MULCOR_s(\lambda, 2\theta) &= NORMVAN_s(\lambda, 2\theta) - M_s \\ &= A_{s,s}N_s\Sigma_s(\lambda, 2\theta) \end{aligned} \tag{4.22}$$

$$\begin{aligned} MULCOR_{s+c}(\lambda, 2\theta) &= NORMVAN_{s+c}(\lambda, 2\theta) - M_{sc} \\ &= A_{s,sc}N_s\Sigma_s(\lambda, 2\theta) + A_{c,sc}N_c\Sigma_c(\lambda, 2\theta) \end{aligned} \tag{4.23}$$

$$\begin{aligned} MULCOR_c(\lambda, 2\theta) &= NORMVAN_c(\lambda, 2\theta) - M_c \\ &= A_{c,c}N_s\Sigma_s(\lambda, 2\theta) + A_{c,sc}N_c\Sigma_c(\lambda, 2\theta) \end{aligned} \tag{4.24}$$

Now, attenuation correction is simply applied following Equation 4.25:

$$ABSCOR_s(\lambda, 2\theta) = \Sigma_s(\lambda, 2\theta) = \frac{MULCOR_{s+c}(\lambda, 2\theta) - \frac{A_{c,sc}}{A_{c,c}} MULCOR_c(\lambda, 2\theta)}{N_s A_{s,sc}} \quad (4.25)$$

The final requirement is the introduction of N_s (i.e. the number of atoms irradiated by the beam). Due to the fact that powders are not fully packed in the container, Gudrun package gives the possibility to choose the most appropriate "tweak factor" which is the inverse of the packing fraction. For example, if the packing fraction is 0.5, the corresponding tweak factor value is 2.0. Such tweak factor is important also for application of multiple scattering and attenuation because the density value adopted in the corrections are divided by it. X-ray data require the application of some additional treatment for polarisation, Bremsstrahlung scattering and fluorescence.

8. At this time, the differential scattering cross section of the sample as a function of λ and 2θ and corrected for attenuation and multiple scattering has been obtained and put in an absolute scale, but this is not enough to start with data modeling. Data are grouped like thousands of patterns if thousands are the detector involved in the data collection (i.e. time of flight technique). Thus, detectors have to be grouped into a single spectrum and the patterns are merged with a common scale of units.

Note that, before converting structure factors to pair distribution functions by means of Fourier transform (see Equations 4.1 and 4.2), data should be cleaned of a background (incoherent and single atom scattering) that is Q dependent. In the Gudrun package, this step is based on [Soper, 2009] and is required because background i) does not provide information about distances between atoms and ii) can introduce not-physical structure (peaks or valleys) in the lower region of real space that is typically characterized by a null value of the corresponding g(r).

4.2.4 Data modeling

Data have been modeled using EPSR (Empirical Potential Structure Refinement)[Soper, 2010b; Soper, 2005]. Each glass model consisted of a cubic box, with periodic boundary conditions, containing 1700 atoms, sized to match the measured glass density of 0.0542 atoms Å^{-3}. In EPSR, the potential energy of the investigated system consists of two primary terms: the reference potential energy U_{ref} and the empirical potential energy U_{emp}. U_{ref} and U_{emp} can be split into terms related to all the possible couples of atoms in the simulating box; thus, the potential energy between two distinct atoms α and β, separated by the distance *r*, is given by:

$$U_{\alpha,\beta}(r) = U^{ref}_{\alpha,\beta}(r) + U^{emp}_{\alpha,\beta}(r) \quad (4.26)$$

EPSR starts from a standard Monte Carlo (MC) simulation that moves atoms, or molecules, by means of translations and rotations. A move consists of a small change in the (x,y,z) coordinates of atoms and molecules, and the acceptance of this move is based on the Metropolis condition: if the potential energy U of the system is decreased with the movement, such movement is always accepted, but, if the potential energy is increased, such movement is accepted with probability $\exp^{\frac{-\delta U}{kT}}$. In this step, MC runs with the reference potentials only which are based on a two bodies Lennard-Jones potential plus effective Coulomb charges as expressed in Equation 4.27:

$$U_{\alpha,\beta}^{i,j}(r) = 4\epsilon_{\alpha\beta}\left(\left(\frac{\sigma_{\alpha\beta}}{r_{ij}}\right)^{12} - \left(\frac{\sigma_{\alpha\beta}}{r_{ij}}\right)^{6}\right) + \frac{q_\alpha q_\beta}{4\pi\epsilon_0 r_{ij}} \tag{4.27}$$

where $\varepsilon_{\alpha,\beta}$ is the well depth parameter, $\sigma_{\alpha,\beta}$ is the range parameter, $r_{i,j}$ is the distance between the atoms, and $q_\alpha q_\beta$ are the formal Coulomb charges of the α and β species. $\varepsilon_{\alpha,\beta}$ and $\sigma_{\alpha,\beta}$ can be calculated from the Lorentz-Berthelot mixing rules:

$$\varepsilon_{\alpha,\beta} = \sqrt{\varepsilon_\alpha \varepsilon_\beta} \qquad \sigma_{\alpha,\beta} = \frac{1}{2}(\sigma_\alpha + \sigma_\beta) \tag{4.28}$$

Figure 4.4 show the variation of Lennard-Jones potential plus Coulomb charge between two atoms α and β if their distance *r* is increased. If $\sigma_{\alpha,\beta}$ is increased the position of the potential well moves to higher r-values, whereas if $\varepsilon_{\alpha,\beta}$ is increased the potential well is deeper.

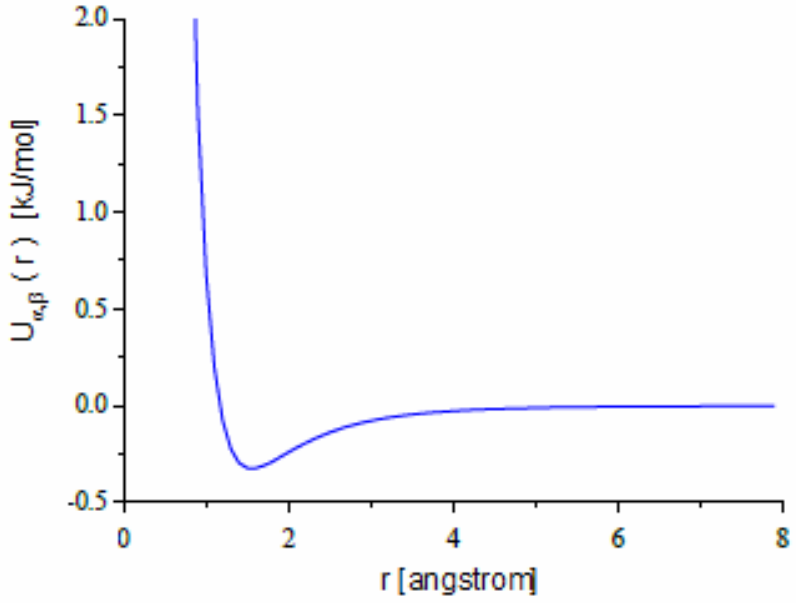

Figure 4.4: Variation of EPSR reference potential between two atoms as function of their distance.

Once the system reaches equilibrium, the structure factors of the model are calculated and compared to those obtained from scattering data. This difference between model and experiment is then used to generate a set of empirical potential perturbation functions that are added to the reference potential in the next step of EPSR, with the aim of driving the model into agreement with the experimental data. This procedure of calculating the difference between the experimental and model structure factors, generating a perturbation potential to modify the atomic interactions, is continued until, at the end of the process, the pairwise distribution of atoms in the model agrees with the experimental structure factors. The empirical potential adopted by EPSR is expressed by Equation 4.29:

$$U_{\alpha,\beta}^{emp}(r) = kT \sum_i C_i p_{n_i}(r, \sigma_r) \tag{4.29}$$

where $p_n(r, \sigma_r) = \frac{1}{4\pi\rho\sigma^3(n+2!)} \frac{r}{\sigma}^n \exp^{\frac{-r}{\sigma}}$, C_i are real number, σ_r is a width function, set by the user, and ρ is the

total atomic density of the system. The function $p_n(r, \sigma_r)$ has an exact 3-dimensional Fourier transform to Q-space as:

$$p_n(Q, \sigma_r) = 4\pi\rho \int p_n(r, \sigma) \exp^{iQr} dr \tag{4.30}$$

Therefore, in EPSR, the coefficients C_i are estimated directly from the diffraction data by fitting a series of the form:

$$U^{emp}(Q) = \sum_i C_i p_{ni}(Q, \sigma_Q) \tag{4.31}$$

Thus, at the N+1 interaction, the potential energy of the system is given by:

$$U^{N+1}(r) = \frac{1}{2} \sum_i \sum_{i \neq j} U^N_{\alpha,\beta} + kT(\ln \frac{g_{\alpha,\beta}(r)}{g^D_{\alpha,\beta}(r)}) \tag{4.32}$$

The term 1/2 is introduced to avoid double counting of pair atoms. This step is ideally continued until the simulated $S_{\alpha,\beta}(Q)$ is equal to the experimental one and, consequently, the simulated $g_{\alpha,\beta}(r)$ is equal to the experimental one. There is a parameter, named "ereq", which can be increased during this step and that let one to evaluate how largely the empirical potential can be refined. Practically, the simulation is stopped when it has converged (i.e. $U^{N+1}_{\alpha,\beta}(r)$ is equal to $U^N_{\alpha,\beta}(r)$ and then the Monte Carlo process is continued, and average structure functions are calculated. Before start running an EPSR simulation, for each chemical species, the ionic charge, the atomic weight, the well depth parameter ε, the range parameter σ must be introduced in an appropriate file. The first two parameters are easy to be defined because they are well known in literature, the last two parameters require a careful choice. In the current study, silicon and oxygen parameters were directly taken from the EPSR simulation on silica glass performed by [Bowron, 2008]. The reference parameters for the other elements (i.e. aluminum, calcium and sodium) were chosen to deliver appropriate first neighbor distance interactions and charge-balanced local stoichiometries, that were consistent with the adopted silica parameters. This is an important consideration when setting up the reference potential model of a network glass, since the empirical potential generated in the analysis is not capable of overcoming major discrepancies, if the reference potential favors first neighbor contacts at too large an interaction distance. Aluminum environments were expected to be close to those of silicon due to the similarities in the behavior of the two elements, regarding both coordination number and bond distance with oxygen [Smith & Bailey, 1963]. Things were a little more complex for sodium and calcium, as both Na-O and Ca-O distances range from 2.1 to 2.6 Å, in alumino-silicate glasses [Greaves, 1985; Benoit et al., 2005; Cormier & Neuville, 2004; Karlsson et al., 2005; Angeli et al., 2000]. The experimentally derived total pair distribution functions, g(r), show two peaks in this range (see Figure 4.5), the first one attributed to Ca-O and Na-O bond distances, and the second one to O-O bond distances.

This choice can be better explained with a comparison among the experimental g(r) of our three samples (Figure 4.5): a decrease in intensity of the 1.6 Å peak and an increase in intensity of the 2.2 Å peak in g(r) from sample A to sample C can be addressed to the variations in the samples' chemical composition. In fact, sample A, characterized by the highest content of Si and Al, has the most intense 1.6 Å peak in g(r); on the other hand, sample C, characterized by the highest content of Na, has the highest 2.2 Å intensity in g(r). After a few preliminary tries,

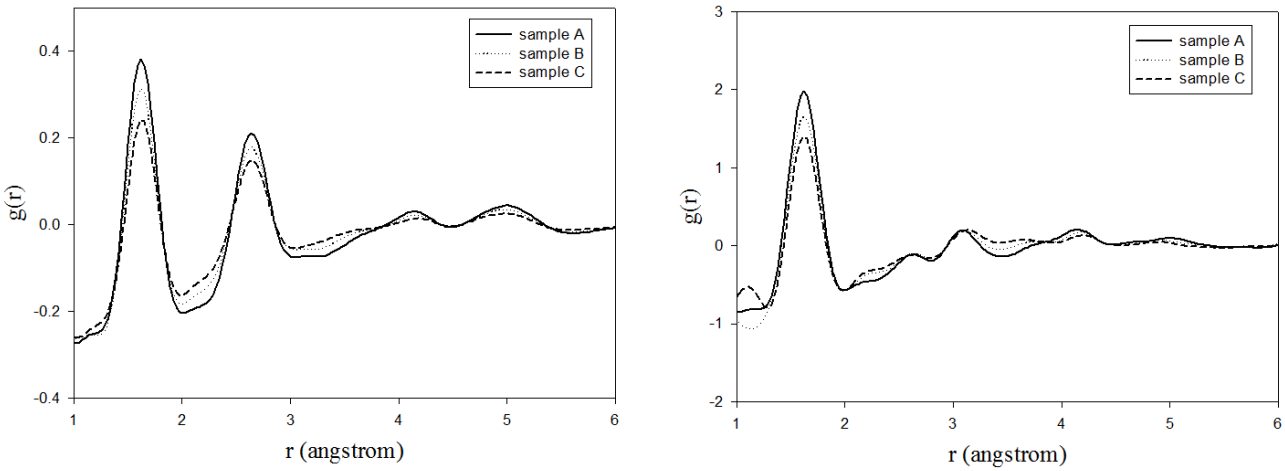

Figure 4.5: Comparison of the experimentally measured total g(r)'s for the three samples investigated. Neutron data are on the left-hand side, X-ray data on the right-hand side.

σ values for Ca and Na were fixed to 2.2 Å and 2.8 Å, respectively. Following equilibration with these parameters, sample C exhibits the graphical fit (dotted line) shown in Figure 4.6, where the left-hand panel represents the fit to the neutron data and the right-hand panel to the X-ray data.

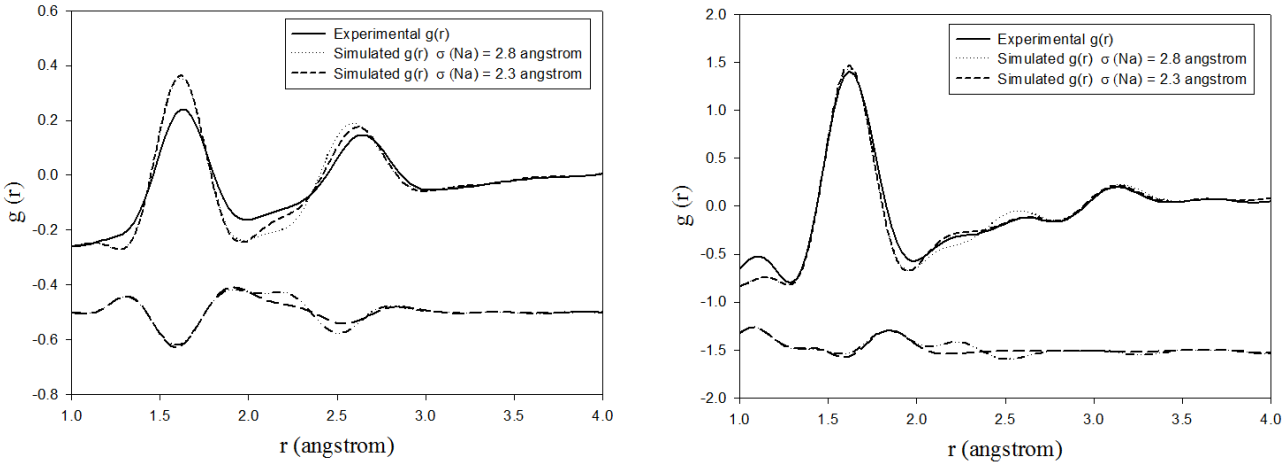

Figure 4.6: Real space illustration of the misfit at 2.2 Ågetting better as the reference potential parameters are optimized prior to EPSR refinement. Neutron data are on the left-hand side, X-ray data on the right-hand side.

By looking at the residuals, one can note that the larger differences can be found around 2.2 Å (underestimation of the calculated intensity) and around 2.6 Å(overestimation of the calculated intensity). With a σ value for sodium of 2.8 Å, its partial g(r) shows the first peak at 2.6 Å, likely producing the overestimation of the calculated intensity in this range. If we now reduce the sodium σ value to 2.3 Å, the first peak of the partial g(r) for Na-O distance moves to 2.3 Å, giving a much better fit (see dashed line in Figure 4.6) and a Na-O distance more consistent with the literature data [Cormier & Neuville, 2004; Zotov & Kepppler, 1998]. Table 4.2 reports the adopted values of ε, σ and ionic charges for the various atomic species.

The final fits of F(Q) and g(r) of all three samples are shown in Figure 4.7.

Atom	ϵ (kJ mol^{-1})	σ (Å)	q (e)
Si	0.80	0.76	+4
Al	0.80	1.20	+3
Ca	0.80	2.20	+2
Na	0.80	2.30	+1
O	0.65	3.69	-2

Table 4.2: Configuration and final Lennard-Jones parameters.

4.3 Results and Discussion

The results of EPSR modeling have been discussed into 3 distinct sections, depending on the role of the atomic species in the structure. So the first section is dedicated to network forming elements, the second to network modifying elements and the third to the typology of oxygen sharing.

4.3.1 Network forming elements

Silicon and aluminum are network-forming elements, as they confer stability to the structure because of the interconnection of their local, largely tetrahedral, structural units. Their partial pair distribution functions with oxygen, coordination numbers and bond angles are represented in Figure 4.8 (for silicon), in Figure 4.9 (for aluminum) and summarized in Table 4.3. In all three samples, the Si-O partial pair distribution function has the first peak at about 1.62 Å (see left part of Figure 4.8) without significant variations between samples.

The calculated coordination number distributions for silicon (see middle part of Figure 4.8) confirms the well-defined structural environment of silicon: in all three samples, a fraction of 0.99 of silicon atoms have a 4-fold coordination. Furthermore, in all samples, the most probable O-Si-O angular value (107°30' as shown in the right part of Figure 4.8) is close to the ideal tetrahedral value of 109°47'. Bond distances, evaluated from the maximum of the peak in the corresponding partial g(r) can be found in Table 4.3.

	Sample A	Sample B	Sample C
Si-O (Å)	1.62	1.62	1.62
Al-O (Å)	1.65	1.68	1.68
Si-O (coord nr)	3.99 ($\pm$ 0.09)	4.00 ($\pm$ 0.09)	4.00 ($\pm$ 0.08)
Al-O (coord nr)	3.64 ($\pm$ 0.48)	3.74 ($\pm$ 0.44)	3.89 ($\pm$ 0.37)
O-Si-O (angle)	107^{o}30' (14.8)	107^{o}30' (15.4)	107^{o}30' (16.5)
O-Al-O (angle)	111^{o} (23.5)	107^{o} (19.9)	109^{o}30' (16.5)

Table 4.3: Bond distances, coordination numbers, and O-M-O angles for network forming atoms. The numbers in parentheses represent the distance from the average value. The cutoff values for Si-O distances were 1.45 and 1.9 Å, while those for Al-O distances were 1.45 and 2.1 Å. The number in parentheses after the angular values represent the full width at half maximum of the peak in the probability distribution.

In the same table, the O-M-O angles are taken from the peak maximum in the probability distributions shown in the left part of Figures 4.8 and 4.9; the values in parentheses represent the full width at half-maximum (FWHM) of the probability distributions, as a measure of the disorder in the angular values. As it can be seen from Table 4.3, an increase in sodium content, from sample A to sample C, seems to sharpen the O-Al-O distribution (FWHM goes from 23.5 to 16.5 with increasing Na content) and, on the other hand, to widen, though in a less distinct way, the O-Si-O distribution (FWHM goes from 14.8 to 16.5 with increasing Na content). The coordination numbers shown in Table 4.3 are the average values of the frequency histograms shown in Figures 4.8 and 4.9, while the numbers in parentheses represent the distance from the corresponding average value. The first significant difference in the

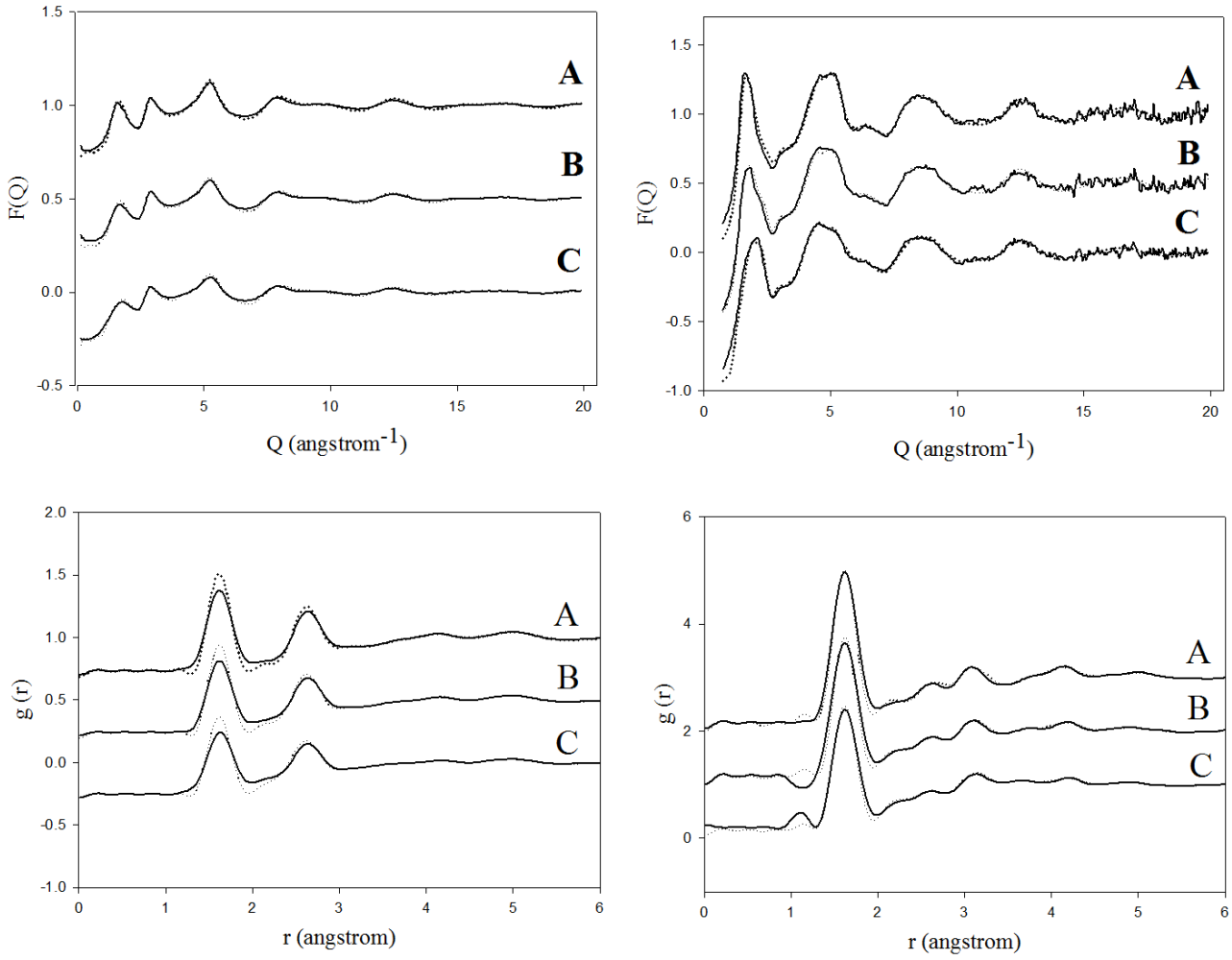

Figure 4.7: Final total F(Q) EPSR fits to the neutron (left-hand side) and X-ray (right-hand side) data. The EPSR model was only refined against the F(Q) data to avoid the risk of fitting Fourier transform artifacts in the total pair distribution functions. However, for completeness, the resulting comparison in real space is also shown in the lower panels.

short-range order can be noted in Table 4.3 for aluminum atoms, as also shown by the different position of the first peak in the partial g(r) for the Al-O bond (see left part of Figure 4.9) and by the different coordination number of aluminum (see middle part of Figure 4.9).

In fact, when the sodium content is increased from sample A to sample C, the aluminum average coordination number moves from 3.64 to 3.89, as shown in the middle part of Figure 4.9. However the distortion of the coordination polyhedra seems to be inversely related to the sodium content, as shown by the wider O-Al-O angular spread (right part of Figure 4.9). No evidence of five-coordinated Al sites has been obtained with these simulations. All of these results are in agreement with previous works on a similar glass composition [Cormier et al., 2003]. The presence of Al in tetrahedral sites with oxygen atoms at the vertices of the geometric unit produces a lack in positive charge that is compensated by mono- or bivalent ions (Ca and Na), making the Al-Ca and Al-Na distances shorter than the corresponding distances for Si, as will be seen in more detail in the next section.

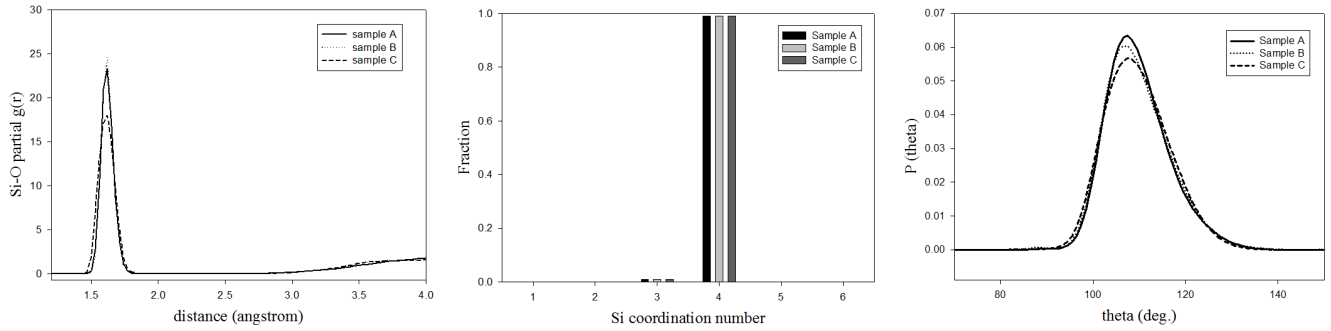

Figure 4.8: Si-O partial g(r), histogram of distribution of coordination number, and O-Si-O angle distribution. A solid line represents data for sample A; a dotted line, those for sample B; and a dashed line, those for sample C.

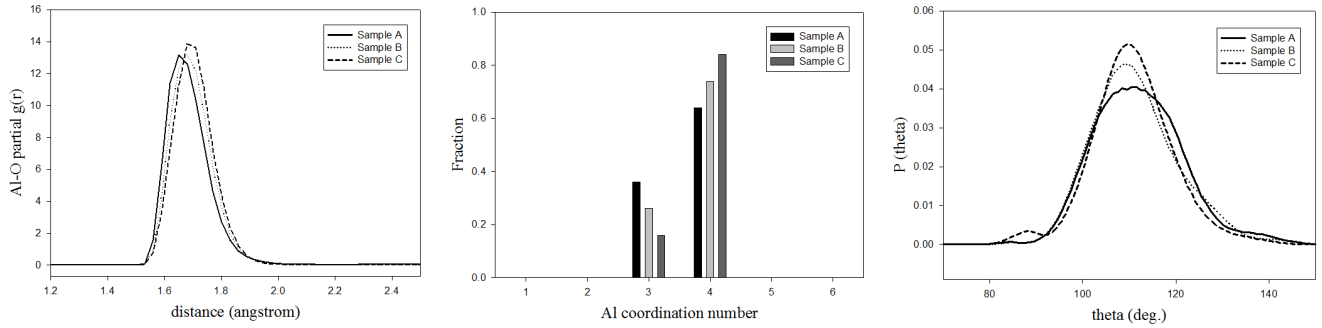

Figure 4.9: Al-O partial g(r), histogram of distribution of coordination number, and O-Al-O angle distribution. A solid line represents data for sample A; a dotted line, those for sample B; and a dashed line, those for sample C.

4.3.2 Network modifying elements

Calcium and sodium atoms can play two different roles in alumino-silicate glasses. They can be network-modifying elements that depolymerize the network, but they can also, as previously mentioned, have a charge-compensating effect when they are adjacent to AlO_4^- tetrahedra. For Ca and Na, the choice of the cutoff values to be used in order to obtain reasonable values for distances, coordination numbers, and O-M-O angular values, is crucial and particularly delicate. The results are represented in Figure 4.10 (for calcium), 4.11 (for sodium) and Table 4.4. By looking at the left part of Figures 4.10 and 4.11, one can easily see that the partial g(r) for Ca-O and Na-O is not as sharp as that for Si-O and Al-O, and the peaks show intensity spreading from the peak maximum to larger distances. Because of this, different cutoff choices may produce slightly different values for Ca-O and Na-O coordination numbers and average distances.

However, this does not produce a ”wrong” value for the parameters that are determined, but care must be taken if these values are to be compared with literature, where criteria may be different, as remarked by [Zotov & Keppler, 1998]. For this reason, in this study, we have used the same cutoff value for all the samples, in order to obtain comparable results. This criterion also applies to the quoted values for coordination numbers (see middle part of Figure 4.10) and for O-M-O angular distributions (see right part of Figure 4.10). The Ca-O bond distance observed in our structural models is around 2.2 Å in all three samples (see Table 4.4), and the Ca coordination number does not change much between samples, with mean values ranging from 5.02 to 5.08 (in agreement with [Cormier et al., 2005]), with increasing sodium content.

The large spread in coordination number (from 3 to 7, as seen in the middle part of Figure 4.10) indicates that calcium has a disordered distribution in the structure, without a well-defined coordination polyhedron. This

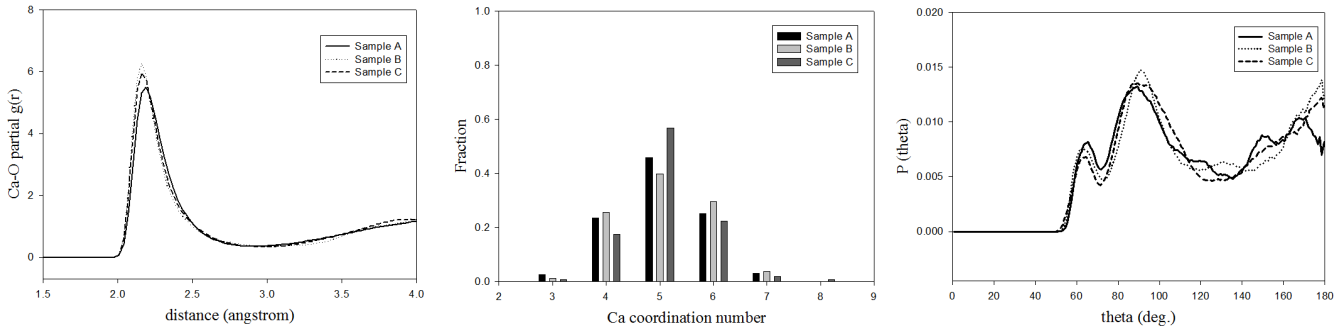

Figure 4.10: Ca-O partial g(r) on the left side, histogram of distribution of coordination number on the middle side, and O-Ca-O angle distribution on the right side. A solid line represents data for sample A; a dotted line, those for sample B; and a dashed line, those for sample C.

	Sample A	Sample B	Sample C
Ca-O (Å)	2.19	2.17	2.16
Na-O (Å)	2.40	2.34	2.29
Si-Ca (Å)	3.40	3.48	3.52
Si-Na (Å)	3.45	3.50	3.45
Al-Ca (Å)	2.88	2.90	2.90
Al-Na (Å)	3.00	2.92	2.90
Ca-O (coord nr)	5.03 (± 0.84)	5.09 (± 0.86)	5.10 (± 0.75)
Na-O (coord nr)	6.00 (± 1.17)	5.89 (± 1.05)	5.72 (± 0.99)
O-Ca-O (angle)	89°30’	91°	89°
O-Na-O (angle)	56°30’	60°	59°30’

Table 4.4: Bond distances, coordination numbers and O-M-O angles for network forming atoms. The numbers in parentheses represent the distance from the average value. The cutoff values for Ca-O distances were 1.9 and 2.9 Å, while those for Na-O distances were 2.0 and 3.2 Å.

consideration is confirmed by the O-Ca-O angular distribution, with angles varying from 60 to 180° (see right part of Figure 4.10). By looking at Table 4.4, one can easily note the charge-compensating effect of Ca and Na for aluminum in tetrahedral coordination: Al-Ca and Al-Na distances are much smaller than Si-Ca and Si-Na distances: for instance, in sample A, Al-Ca and Al-Na distances are 2.88 and 3.00 , respectively, while Si-Ca and Si-Na distances are 3.40 and 3.45 , respectively. Sodium has a behavior similar to the one of calcium. The first peak in the Na-O partial g(r) is displaced to a smaller value from sample A to sample C: with increasing Na content, it goes from 2.4 to 2.29 Å, as also shown in Table 4.4 and visually in the left part of Figure 4.11, in agreement with the literature[Zotov & Keppler, 1998].

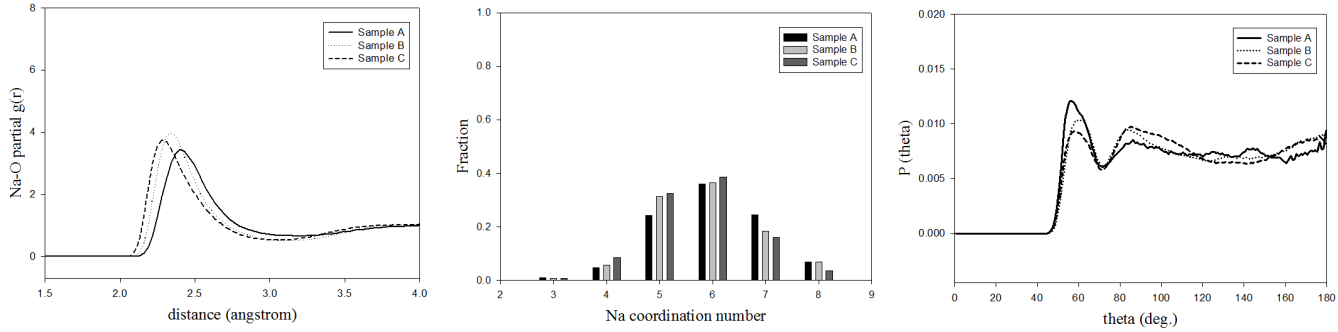

Figure 4.11: Na-O partial g(r) on the left side, histogram of distribution of coordination number on the middle side, and O-Na-O angle distribution on the right side. A solid line represents data for sample A; a dotted line, those for sample B; and a dashed line, those for sample C.

As for calcium, the comparison of sodium coordination number with other works may not be is not meaningful: our slightly different cutoff value may easily explain our larger Na coordination number with respect to [Zotov & Keppler, 1998]. As a matter of fact, sample C shows the smallest average Na coordination number (5.72), whereas a more diffuse coordination of 7-8 is present in sample A (middle part of Figure 4.11). Finally, the O-Na-O angular distribution is always wider than the O-Ca-O distribution and goes from about 45 to 180°, with two more pronounced peaks at about 55 and 85° (right part of Figure 4.11).

4.3.3 Bridging (BO) and nonbridging (NBO) oxygens

Data obtained with EPSR can also provide information about the type of oxygen bonding and sharing, such as, for example, the distribution of bridging oxygen (BO) and nonbridging oxygen (NBO). A simple computer code that interrogated the EPSR structural configurations allowed us to distinguish between the various types of chemical and geometrical environments for the oxygen atoms. Before discussing the results, a few definitions follow. A bridging oxygen (BO) is defined as an oxygen that is shared by two tetrahedra in a sphere with a defined radius (the cutoff value used in this study was 2 Å), like the red circle in Figure 4.12; bridging oxygens were distinguished, in this study, by means of the type of polyhedra surrounding them. If one oxygen is shared by only two tetrahedra, it is called a BO', whereas, if it is shared also by a different polyhedron (e.g. an octahedron), it is called BO". Examples of BO' and BO" are represented in Figure 4.12 by the green and yellow circles, respectively. Obviously, BO is equal to the sum of BO' and BO". Moreover, it was also possible to study the different arranging of Si and Al atoms, that is, the way through which they are linked with bridging oxygens (for total BO, BO', and BO"): Si-O-Si, Si-O-Al, and Al-O-Al. An NBO is an oxygen that is shared by one single tetrahedron, but it could also be connected to a different coordination polyhedron, like the blue circle in Figure 4.12.

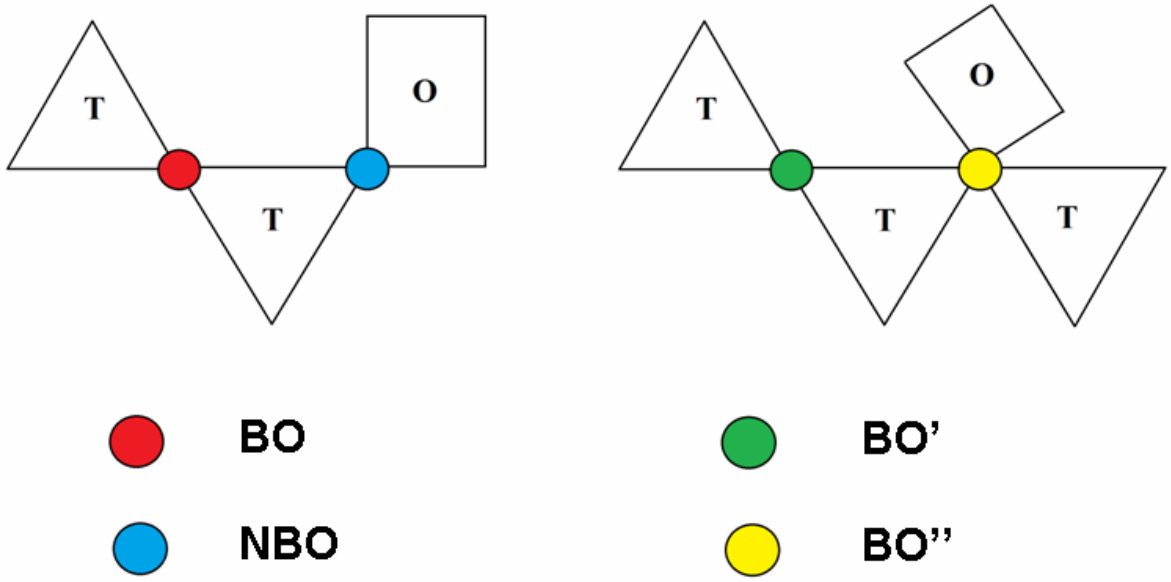

Figure 4.12: Graphical representations i) of BO (blue circle) and NBO (red circle), on the left part; ii) of BO' (green circle) and BO" (yellow circle).

Furthermore, we can also take into account oxygens shared by three tetrahedra (tricluster, TBO), by no tetrahedra (tetrahedron-free oxygen, TFO), or not bonded at all (free oxygens, here called simply FREEOX). All of these results can be found in Table 4.5, obtained in all samples by using the cutoff values for Si and Al shells fixed at 2 Å and the one for Ca and Na fixed at 3.2 Å.

	Sample A		Sample B		Sample C	
BO'	0.46		0.32		0.21	
Si-O-Si		0.74		0.79		0.80
Si-O-Al		0.25		0.20		0.19
Al-O-Al		0.01		0.01		0.01
BO"	0.26		0.34		0.40	
Si-O-Si		0.62		0.61		0.63
Si-O-Al		0.35		0.33		0.32
Al-O-Al		0.03		0.06		0.05
NBO	0.25		0.31		0.35	
FREEOX	0.01		0.00		0.00	
TBO	0.01		0.01		0.01	
TFO	0.01		0.02		0.03	
BO	0.72		0.66		0.61	
(Si-O-Si)		0.70		0.70		0.70
(Si-O-Al)		0.28		0.27		0.27
(Al-O-Al)		0.02		0.03		0.03

Table 4.5: Distribution of bridging and non-bridging oxygen atoms: BO' are oxygens shared only by 2 tetrahedra, BO" are shared also by another polyhedron, NBO belongs to a single tetrahedron, FREEOX are not bonded, TBO are shared by three tetrahedra, and TFO are not linked to any tetrahedron (but to other polyhedra). BO is the total fraction of bridging oxygens (i.e. equal to the sum of BO' and BO"). More details can be found in the text.

As mentioned in the case of coordination number and bond angles, it is important to remark that the final results are strongly affected by the cutoff value, especially for BO' and BO". The table is organized as follows: for each sample, the first column reports the number of BO', BO", NBO, FREEOX, TBO, and TFO, in terms of fractions of the total oxygen atoms. The second column reports, for BO' and BO", the different arranging of Si and Al atoms (Si-O-Si, Si-O-Al, Al-O-Al), normalized to the total number of BO' and BO", respectively. The bottom part of the table shows the same results for the total BO atoms. With the aid of the computer code, it was also possible to have a closer look at the role of Ca and Na in the glass network, by counting the number of BO" within a cutoff distance from Ca and Na. For each chemical species, then, it was possible to establish the fraction of Si-O-Si, Si-O-Al, and Al-O-Al connected with Na or Ca. These results can be found in Table 4.6, obtained with the same cutoff values as in Table 4.5. In a much similar way as in Table 4.5, for each sample, the first column shows the number of BO" connected to Na and Ca, in terms of the fraction of the total number of BO".

	Sample A		Sample B		Sample C	
Na/(Na+Ca)	0.50		0.69		0.79	
BO" (Na)	0.62		0.72		0.82	
Si-O-Si		0.67		0.59		0.64
Si-O-Al		0.30		0.34		0.31
Al-O-Al		0.03		0.07		0.05
BO" (Ca)	0.38		0.28		0.18	
Si-O-Si		0.55		0.65		0.60
Si-O-Al		0.42		0.31		0.37
Al-O-Al		0.02		0.04		0.03

Table 4.6: Distribution of bridging and non-bridging oxygen atoms: BO" are oxygens shared by two tetrahedra and by another polyhedron. More details can be found in the text.

The second column shows the different arranging of Si and Al atoms, normalized to the total number of BO" type (bonded to Na or Ca, respectively). BO" are divided in three types (i.e., those connected to Si-O-Si, to Si-

O-Al, and to Al-O-Al). For each of them, the proportion of Na and Ca atoms connected to them is also shown. The table also shows, in the first line, for an easier comparison, the ratio of Na and Ca atoms present in the simulation box for each sample. In our samples, NBO and BO are the most important oxygen classes, because they provide important information about the role of some cations involved in the structure, in particular, the role of chemical elements, such as Ca and Na. NBOs are due to the role of these elements as network modifiers and tend to depolymerize the network, whereas, on the other hand, BOs are sensitive to the charge-compensating role of these elements. This is well-known in literature [Cormier et al., 2003]. Important differences are present in the three samples. As expected, BO" and NBO fractions increase with increasing Na content (i.e., from sample A, where, for instance, the BO" fraction is equal to 0.26, to sample C, where the BO" fraction is equal to 0.40), whereas BO' and total BO decrease (in sample A, for instance, the BO' fraction is equal to 0.46; in sample B, it is equal to 0.32; and in sample C, it is equal to 0.21), though not in a strictly proportional manner. In fact, the differences are larger by going from sample A to sample B, then by going from sample B to sample C, even if the variation in Na content in exactly the same. TBO fractions (i.e., tribonded oxygens) are very small in all the samples (0.01), in agreement with the literature [Toplis et al., 1997], as their formation (as well as the formation of 5-fold aluminum) is more likely in peraluminous glasses, with a molar ratio between modifiers and Al smaller than 1 (i.e., nMOD/nAl < 1, where n is the number of moles of modifiers (MOD) and aluminum (Al)), rather than in peralkaline glasses, such as samples A, B, and C, where, instead, nMOD/nAl is 1.9, 2.7 and 3.8, respectively. Concerning Si/Al arrangements, the Si-O-Si linkage is the most diffused, because of the high Si/Al ratio in all the samples, whereas the number of Al-O-Al linkages is very small, in agreement with the so-called "avoidance rule" [Loewenstein & Wilk, 1954]. By looking more closely at Table 4.5, it can be easily noted that the Si-O-Si linkage is more diffused in BO' atoms, and this preference increases, from a fraction of 0.74 to a fraction of 0.80, with increasing Na content. On the other hand, in all three samples, the proportion of Si-O-Al linkages is larger for BO" than for BO' atoms, probably due to the decrease of ionic charge caused by the substitution of Si with Al atoms. By looking at the total number of BO atoms (bottom part of the table), one can note that the arrangement of Si and Al atoms does not change with Na content, because it is determined by the Si/Al starting ratio only: the values for Si-O-Si, Si-O-Al, and Al-O-Al fractions are about 0.70, 0.27, and 0.03, respectively. The different roles of Ca and Na can be assessed by looking at the results in Table 4.6. It is particularly interesting to look at the different arrangements of Si and Al atoms around BO" atoms linked to Na and Ca: there are no trends as a function of Na content. It should be noted that the fraction of BO" connected to sodium increases with Na content, but it is not only determined by the larger amount of Na present (Na/(Na + Ca)), as it is always larger than the fraction of Na atoms in the simulation box (cf. first line of the table). This effect is more visible for sample A with respect to the other samples (i.e., the difference between the fraction of BO" connected to Na and Na/(Na + Ca) is 0.12 for sample A, and decreases to 0.03 for samples B and C). The smaller differences in samples B and C can be explained by the simultaneous decrease, from sample A to sample C, in the number of AlO_4^- tetrahedra and the increase in the number of Na atoms: a lower number of negative charges needs to be balanced in the tetrahedra network, and the Na atoms tend to form a larger number of bonds with NBO. Moreover, the present chapter showed that, due to a preference of Na atoms for BO", well above the one due to the composition, there is a tendency for Na atoms to compensate the negative charge introduced in the tetrahedra by the presence of Al. A full comparison with the literature, such as with the papers by [Cormier & Neuville, 2004] and by [Cormack & Du, 2001] which are the closest in composition to the samples studied here, is not trivial, because there are differences in both the chemical composition and the adopted cutoff values used for bond distances and angles. However, a few comments can be made, in particular, about the role of network modifiers: both cited papers find a larger number of NBOs around Ca atoms than around Na atoms, and this is compatible to what was found in this study (a preference of Na atoms

for BO"). Furthermore, [Cormier & Neuville, 2004] showed that, if sodium is replaced by calcium, and the molar ratio nMOD/nAl is 1.33, an almost fixed ratio between BO and NBO is observed; that is, a similar polymerization degree is likely in all the samples. In the present investigation, the molar ratio nMOD/nAl is much larger, due to the lower Al amount, and a distinct decrease in the ratio between BO and NBO is observed from sample A to sample C, hence a smaller polymerization degree. Additional information about the geometry of connectivity in the network can be found by looking at the distribution of Si-O-Si angles in Figure 4.13: an increase in Na content causes a decrease of the Si-O-Si angle, that is, a decrease in the number of tetrahedra that compose the polyhedral ring, thus a less-polymerized structure[Cormier et al., 2003]. These indications about oxygen sharing are known to be strongly correlated to some properties of glasses: for example, a loss of connectivity between tetrahedra causes a decrease in viscosity, with a consequent decrease in the energy required for atomic movements, and resulting in a lower glass transition temperature[Cormier et al., 2005]. On the basis of the structural network observed after EPSR simulations, especially in terms of BO and NBO distributions, the highest glass transition and softening temperatures should be expected for sample A because of the highest tetrahedral connectivity among the investigated samples. An additional confirmation of that is given by Figure 2.15 where the higher is the SiO_2/CaO ratio, the higher are the glass transition and softening temperatures.

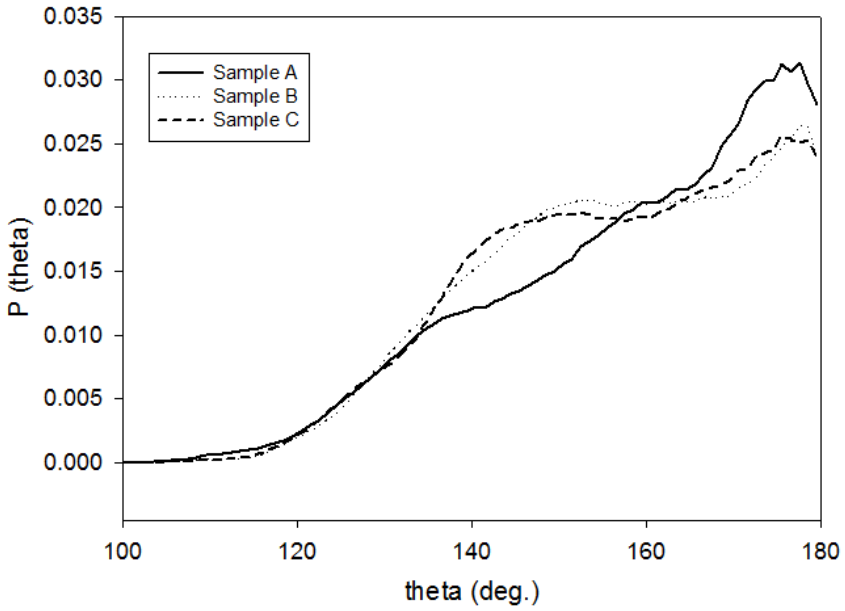

Figure 4.13: Si-O-Si angle distribution.

4.4 Conclusions

Although the presence of 5 chemical elements that correspond to 15 partial distribution functions, the combination of neutron and X-ray diffraction within the constrained EPSR modeling procedure was able to provide a reasonable and coherent structural model of these systems. Silicon and aluminum maintain their network-forming role, and their structural network is the same (for silicon) or similar (for aluminum) to their traditional behavior. Conversely, calcium and sodium, which are considered as network modifiers, are characterized by a more disordered distribution of bonding angles and coordination numbers. The increased presence of sodium in sample C corresponds to a

larger number of NBO and BO” atoms, in agreement with the charge-compensating role of sodium. As the results for these simplified glasses were more than encouraging, a more complete study is under development, introducing EXAFS measurements on Ca K-edge as a complementary technique for these same glasses, and a more complex chemical environment for the next total scattering experiments (by adding Zn and K).

Part IV

Appendix and References

Chapter 5

Appendix and References

5.1 Appendix

5.1.1 Cluster Analysis

Cluster analysis [R.O. Duda et al., 2001] is a useful data processing tool to minimize the effect of noise and allow one to extract pieces of information hidden by high scattered data. A data set is clustered into sub-sets as a function of a variable *X* by requiring that any sub-set is defined and constituted by such data as fulfil the following inequality:

$$\frac{\sigma(X)_j}{\langle X \rangle_j} < \xi \tag{5.1}$$

where $\sigma(X)_j$ and $\langle X \rangle_j$ are standard deviations and mean value of *X* over the *j*-th sub-set; ξ is an arbitrary value common to all sub-sets and that determines their dimensions (i.e. the number of data-points belonging to). We have fixed the ξs here used for clustering by seeking for those values which allow one to attain sub-set of comparable dimensions. One a data set has been partitioned into sub-sets by clustering, the values of any observable are replaced by its mean-values calculated for each sub-set.

5.1.2 Tables

t_f (min)	T_f (°C)	Quartz d_{50} μm	Mullite wt.%	Quartz wt.%	Glass wt.%	Feldspar wt.%	W.A.	(α_L) 10^{-6} (°C^{-1})
0	1200	50	14.9	28.6	10.5	46.0	9.5	5.16
20	1200	50	19.4	27.7	3.8	49.1	3.6	5.00
40	1200	50	17.5	27.2	2.4	52.9	4.1	5.04
60	1200	50	18.3	25.3	2.4	54.0	2.4	5.20
80	1200	50	17.0	25.7	2.1	55.2	2.7	5.16
0	1240	50	16.5	28.3	3.4	51.8	5.4	5.07
20	1240	50	18.0	26.7	0.0	55.3	3.7	5.56
40	1240	50	17.7	23.6	0.0	58.7	1.6	5.32
60	1240	50	18.0	22.6	0.0	59.4	1.1	5.58
80	1240	50	19.5	21.4	0.0	59.1	1.0	5.42
0	1280	50	17.4	24.2	0.0	58.4	3.6	5.24
20	1280	50	17.7	24.1	0.0	58.2	1.7	5.31
40	1280	50	17.6	22.3	0.0	60.1	1.6	5.23
60	1280	50	17.6	19.9	0.0	62.5	0.7	5.03
80	1280	50	17.6	19.5	0.0	62.9	0.5	5.01
0	1200	18	16.1	27.1	8.4	48.4	10.2	5.11
20	1200	18	17.9	24.0	2.4	55.7	3.7	5.83
40	1200	18	18.1	22.3	2.3	57.3	2.7	5.17
60	1200	18	17.2	20.3	1.5	61.0	2.0	6.24
80	1200	18	17.0	17.9	0.8	64.3	0.8	5.44
0	1240	18	17.8	24.7	3.5	54.0	5.6	5.60
20	1240	18	17.3	19.8	0.0	62.9	0.9	5.79
40	1240	18	17.6	18.7	0.0	63.7	0.8	6.17
60	1240	18	17.1	16.3	0.0	66.6	0.6	5.94
80	1240	18	17.5	15.0	0.0	67.5	0.4	5.62
0	1280	18	18.2	21.8	0.0	60.0	2.8	5.42
20	1280	18	17.6	18.5	0.0	63.9	0.7	5.49
40	1280	18	16.8	14.3	0.0	68.9	0.4	4.89
60	1280	18	16.9	13.9	0.0	69.2	0.3	5.12
80	1280	18	16.4	13.0	0.0	70.6	0.3	5.63

Table 5.1: Mineralogical composition (wt%) of the samples after firing. Estimated accuracy on the basis of repeated measures ranges from 0.5wt.% to 0.8wt.%. (α_L) is the linear expansion coefficient over the interval 30-540℃.

Sample	SiO_2	Al_2O_3	CaO	MgO	K_2O	Na_2O	ZrO_2	ZnO
F1	67.22	7.20	13.90	2.59	2.30	1.89	0.93	3.97
F2	68.16	7.20	12.90	2.61	2.31	1.90	0.93	3.99
F3	69.26	7.21	12.31	2.49	2.21	1.82	0.89	3.81
F4	70.32	7.22	11.71	2.37	2.10	1.75	0.85	3.66
F5	71.41	7.23	11.11	2.26	2.00	1.68	0.80	3.51
F6	72.51	7.25	10.52	2.14	1.89	1.61	0.76	3.32
F7	73.63	7.27	9.92	2.02	1.78	1.53	0.72	3.13
F8	74.73	7.28	9.33	1.91	1.68	1.46	0.67	2.94
F9	75.85	7.30	8.72	1.79	1.57	1.39	0.63	2.75
F10	76.97	7.31	8.12	1.67	1.46	1.31	0.59	2.56
F11	73.39	5.80	10.87	2.19	1.95	1.59	0.79	3.43
F12	75.62	5.81	9.68	1.96	1.74	1.44	0.70	3.05
F13	77.86	5.84	8.48	1.72	1.52	1.29	0.61	2.67
F14	66.70	7.02	13.73	2.77	2.46	1.99	0.99	4.34
F15	68.27	7.18	12.81	2.59	2.30	1.88	0.93	4.04
F16	69.59	7.33	12.03	2.44	2.16	1.80	0.87	3.80
F17	70.80	7.46	11.31	2.30	2.03	1.71	0.82	3.57
F18	68.89	6.56	12.83	2.59	2.30	1.86	0.93	4.05
F19	70.39	6.70	11.95	2.42	2.14	1.76	0.86	3.77
F20	71.67	6.82	11.21	2.27	2.01	1.67	0.81	3.54
F21	72.81	6.94	10.54	2.14	1.89	1.59	0.76	3.33

Table 5.2: Molar composition of raw glazes belonging to F series. Note that the compositions have been rescaled for the volatile elements as CO_2 included into calcite and OH included into kaolinite and talc.

Sample	SiO_2	Al_2O_3	CaO	MgO	K_2O	Na_2O	ZrO_2	ZnO
M1	66.69	7.02	13.87	3.61	1.94	2.00	0.52	4.37
M2	66.69	7.02	13.89	2.66	2.11	2.14	1.13	4.36
M3	66.68	7.02	14.11	2.03	2.40	2.39	1.00	4.37
M4	66.68	7.02	14.30	3.00	2.05	2.09	0.50	4.37
M5	66.71	7.02	14.34	2.31	2.05	2.08	1.15	4.34
M6	69.53	7.32	11.99	2.77	2.07	2.12	0.32	3.88
M7	69.56	7.32	12.05	1.99	2.13	2.17	0.93	3.84
M8	69.57	7.32	12.47	1.70	2.09	2.13	0.88	3.84
M9	69.61	7.33	12.44	2.30	2.11	2.15	0.27	3.79
M10	68.84	6.55	12.81	3.20	2.05	2.06	0.37	4.12
M11	68.84	6.55	12.82	2.90	2.20	2.19	0.38	4.12
M12	68.88	6.56	12.96	2.77	1.85	1.89	1.03	4.07
M13	68.80	6.55	13.31	2.31	1.92	1.95	1.00	4.15
M14	68.80	6.55	13.28	2.57	2.16	2.15	0.34	4.16
M15	68.81	6.55	13.25	2.88	2.05	2.07	0.24	4.14
M16	68.82	6.55	13.28	2.21	1.96	1.98	1.06	4.14
M17	71.63	6.82	11.30	2.61	1.86	1.91	0.28	3.60
M18	71.60	6.82	11.24	2.04	1.87	1.92	0.88	3.64
M19	71.60	6.82	11.21	2.71	1.83	1.89	0.31	3.63
M20	71.57	6.82	11.55	1.73	1.89	1.94	0.84	3.65
M21	71.61	6.82	11.57	2.20	1.90	1.94	0.34	3.62

Table 5.3: Molar composition of raw glazes belonging to M series. Note that the compositions have been rescaled for the volatile elements as CO_2 included into calcite and OH included into kaolinite and talc.

Sample	Feldspar	Quartz	Kaolin	Wollastonite	Calcite	Talc	Zincite	Zircon
F1	35.26	18.55	9.35	9.08	11.74	4.27	1.07	10.68
F2	35.68	19.33	9.26	9.19	10.33	4.32	1.08	10.81
F3	34.13	21.39	10.29	8.79	9.88	4.14	1.03	10.34
F4	32.55	23.43	11.31	8.38	9.43	3.95	0.99	9.97
F5	30.96	25.50	12.34	7.97	8.97	3.75	0.94	9.57
F6	29.37	27.62	13.41	7.57	8.51	3.56	0.89	9.08
F7	27.76	29.77	14.49	7.15	8.04	3.37	0.84	8.58
F8	26.18	31.93	15.52	6.74	7.58	3.17	0.79	8.09
F9	24.54	34.10	16.63	6.32	7.11	2.97	0.74	7.59
F10	22.90	36.30	17.73	5.90	6.63	2.78	0.69	7.08
F11	30.82	31.30	6.79	7.94	8.94	3.74	0.93	9.53
F12	27.59	35.72	8.87	7.11	8.01	3.34	0.84	8.53
F13	24.29	40.20	11.01	6.26	7.05	2.94	0.74	7.51
F14	37.89	16.77	7.15	9.76	10.97	4.59	1.15	11.72
F15	35.42	19.54	9.34	9.12	10.26	4.29	1.07	10.95
F16	33.33	21.88	11.20	8.58	9.65	4.04	1.01	10.30
F17	31.40	24.04	12.91	8.09	9.09	3.81	0.95	9.71
F18	35.74	21.50	6.74	9.21	10.35	4.33	1.08	11.05
F19	33.37	24.21	8.78	8.60	9.66	4.05	1.01	10.32
F20	31.35	26.54	10.51	8.08	9.08	3.80	0.95	9.69
F21	29.54	28.61	12.08	7.61	8.55	3.58	0.90	9.13

Table 5.4: Raw composition of glaze belonging to F series expressed as the weight % of the adopted raw materials.

Sample	Feldspar	Quartz	Kaolin	Wollastonite	Calcite	Talc	Zincite	Zircon
M1	29.31	20.59	11.14	8.19	12.52	6.07	0.60	11.58
M2	31.64	20.95	10.15	5.94	14.18	4.38	1.30	11.45
M3	36.65	17.83	8.20	9.69	11.64	3.18	1.16	11.64
M4	30.12	23.25	10.30	0.91	18.52	5.07	0.56	11.27
M5	29.89	23.97	10.62	0.06	19.17	3.86	1.29	11.14
M6	31.83	22.18	12.00	9.59	8.96	4.60	0.37	10.47
M7	32.30	23.43	11.84	6.70	11.20	3.21	1.08	10.24
M8	30.80	26.56	12.00	0.00	16.84	2.83	1.00	9.97
M9	32.33	22.19	12.00	9.85	9.38	3.71	0.32	10.22
M10	31.58	22.82	8.74	9.95	9.92	5.41	0.44	11.14
M11	34.02	22.05	7.63	9.86	9.99	4.86	0.45	11.14
M12	27.90	25.92	10.48	5.96	13.11	4.65	1.19	10.80
M13	29.17	24.48	10.17	8.54	11.61	3.75	1.17	11.10
M14	33.22	22.31	8.14	9.99	10.50	4.22	0.40	11.22
M15	31.59	22.85	8.82	9.94	10.52	4.81	0.28	11.19
M16	29.62	24.96	9.86	6.95	12.77	3.60	1.23	11.01
M17	28.70	27.13	11.92	9.55	8.20	4.36	0.33	9.81
M18	28.68	27.86	12.00	8.00	9.27	3.33	1.03	9.83
M19	28.13	27.86	12.00	7.90	9.34	4.58	0.37	9.82
M20	28.94	27.94	11.95	7.63	9.98	2.75	0.99	9.84
M21	29.19	27.35	11.74	8.65	9.24	3.61	0.40	9.81

Table 5.5: Raw composition of glaze belonging to M series expressed as the weight % of the adopted raw materials.

F series							
Cluster (n. of samples)	Mean chemical composition						
	T_{sint} (°C)	SiO_2	CaO	K_2O	Na_2O	ZnO	N.R.
A (5)	1135	68.3	12.9	2.3	1.9	0.9	3.8
B (6)	1146	70.7	11.7	2.1	1.7	0.8	4.3
C (3)	1151	72.6	10.9	2.0	1.6	0.8	4.8
D (4)	1162	72.9	10.3	1.8	1.6	0.7	5.1
E (3)	1176	76.9	8.4	1.5	1.3	0.6	6.5
	T_{soft} (°C)	SiO_2	CaO	K_2O	Na_2O	ZnO	N.R.
A (5)	1174	69.0	12.5	2.2	1.8	0.9	4.0
B (5)	1186	70.2	12.0	2.1	1.8	0.9	4.2
C (3)	1194	70.4	11.8	2.1	1.8	0.9	4.3
D (4)	1211	73.4	10.4	1.9	1.6	0.8	5.0
E (4)	1237	76.4	8.7	1.6	1.4	0.6	6.3
	T_{sphere} (°C)	SiO_2	CaO	K_2O	Na_2O	ZnO	N.R.
A (5)	1200	67.8	13.2	2.3	1.9	0.9	3.7
B (4)	1211	69.9	12.0	2.2	1.8	0.9	4.2
C (4)	1226	72.2	10.9	2.0	1.6	0.8	4.7
D (4)	1244	74.2	9.9	1.8	1.5	0.7	5.4
E (4)	1276	75.4	9.2	1.6	1.4	0.7	5.8
	$T_{\frac{1}{2}sphere}$ (°C)	SiO_2	CaO	K_2O	Na_2O	ZnO	N.R.
A (3)	1228	67.4	13.5	2.4	1.9	1.0	3.6
B (5)	1240	69.3	12.4	2.2	1.8	0.9	4.0
C (4)	1261	71.9	11.1	2.0	1.7	0.8	4.6
D (4)	1273	73.4	10.3	1.9	1.6	0.7	5.1
E (5)	1320	75.2	9.2	1.7	1.4	0.7	5.8
	T_{melt} (°C)	SiO_2	CaO	K_2O	Na_2O	ZnO	N.R.
A (4)	1258	67.8	13.2	2.3	1.9	0.9	3.7
B (4)	1273	69.8	12.0	2.2	1.8	0.9	4.1
C (4)	1296	72.4	11.1	2.0	1.6	0.8	4.7
D (5)	1317	72.8	10.4	1.9	1.6	0.8	5.0
E (4)	1370	75.4	9.2	1.6	1.4	0.7	5.8

Table 5.6: Clustering analysis results (series F) of $T_{hot-stage}$ as a function of starting molar composition.

M series							
Cluster (n. of samples)	Mean chemical composition						
	T_{sint} (°C)	SiO_2	CaO	K_2O	Na_2O	ZnO	N.R.
A (5)	1143	67.1	14.0	2.1	2.1	1.0	3.5
B (5)	1151	69.7	12.5	2.0	2.0	0.9	4.0
C (3)	1158	69.3	12.4	2.1	2.2	0.3	4.1
D (5)	1162	69.0	12.9	2.0	2.0	0.4	4.0
E (3)	1172	71.6	11.3	1.9	1.9	0.5	4.6
	T_{soft} (°C)	SiO_2	CaO	K_2O	Na_2O	ZnO	N.R.
A (6)	1181	67.9	13.6	2.1	2.1	0.9	3.6
B (5)	1190	69.7	12.5	2.0	2.0	0.7	4.0
C (4)	1195	68.5	13.1	2.0	2.1	0.7	3.8
D (3)	1199	70.0	12.0	2.0	2.0	0.5	4.2
E (3)	1207	70.7	11.8	2.0	2.0	0.3	4.4
	T_{sphere} (°C)	SiO_2	CaO	K_2O	Na_2O	ZnO	N.R.
A (5)	1201	67.1	14.0	2.1	2.1	1.0	3.5
B (4)	1210	68.5	13.0	2.0	2.0	0.9	3.8
C (4)	1214	69.0	12.8	2.1	2.1	0.5	3.9
D (4)	1221	69.9	12.3	2.0	2.1	0.4	4.2
E (4)	1231	71.6	11.3	1.9	1.9	0.5	4.6
	$T_{\frac{1}{2}sphere}$ (°C)	SiO_2	CaO	K_2O	Na_2O	ZnO	N.R.
A (4)	1221	66.7	14.2	2.2	2.2	0.9	3.4
B (4)	1239	68.3	13.2	2.0	2.1	0.6	3.8
C (5)	1247	69.0	13.0	2.0	2.0	0.7	3.9
D (4)	1256	70.6	11.9	2.0	2.0	0.6	4.3
E (4)	1274	71.1	11.5	1.9	2.0	0.4	4.5
	T_{melt} (°C)	SiO_2	CaO	K_2O	Na_2O	ZnO	N.R.
A (4)	1253	66.7	14.2	2.2	2.2	0.9	3.4
B (5)	1270	69.1	12.6	2.0	2.1	0.5	4.0
C (4)	1283	68.8	13.2	2.0	2.0	0.9	3.8
D (4)	1293	69.9	12.3	2.0	2.1	0.6	4.1
E (4)	1332	71.1	11.5	1.9	2.0	0.4	4.5

Table 5.7: Clustering analysis results (series M) of $T_{hot-stage}$ as a function of starting molar composition.

F series							
Cluster (n. of samples)	Mean chemical composition						
	T_g (°C)	SiO_2	Al_2O_3	CaO	K_2O	Na_2O	ZnO
A (10)	66.9	12.7	11.3	2.0	2.0	1.8	1.0
B (8)	68.8	12.6	10.1	1.9	1.8	1.7	1.0
C (3)	68.6	13.9	9.4	1.8	1.7	1.6	0.9
	T_s (°C)	SiO_2	Al_2O_3	CaO	K_2O	Na_2O	ZnO
A (5)	66.2	12.4	12.0	2.0	2.1	1.9	1.1
B (5)	67.0	13.1	10.9	2.0	2.0	1.8	1.0
C (8)	68.7	12.7	10.0	1.9	1.8	1.7	1.0
D (3)	70.0	13.2	9.1	1.7	1.6	1.6	0.9
M series							
Cluster (n. of samples)	Mean chemical composition						
	T_g (°C)	SiO_2	Al_2O_3	CaO	K_2O	Na_2O	ZnO
A (4)	66.1	12.5	12.3	1.8	2.0	1.9	1.0
B (7)	66.7	12.6	12.0	1.7	2.0	2.0	0.9
C (7)	67.1	13.2	11.3	1.8	2.0	1.8	0.6
D (3)	67.3	12.9	11.4	1.7	2.0	2.0	0.5
	T_s (°C)	SiO_2	Al_2O_3	CaO	K_2O	Na_2O	ZnO
A (5)	66.0	12.7	12.4	1.7	2.0	2.1	0.8
B (8)	66.7	12.8	11.8	1.7	2.1	1.7	1.0
C (5)	67.2	13.0	11.4	1.8	2.0	1.9	0.5
D (3)	67.8	13.0	11.0	1.7	1.9	2.1	0.4

Table 5.8: Clustering analysis results (series M) of $T_{hot-stage}$ as a function of starting molar composition.

NIST SRM676a α-Al_2O_3		a=4.7599 α=90°	b=4.7599 β=90°	c=12.9935 γ=120°	ICSD ref.51687 R-3c
Atom type	x coord.	y coord.	z coord.	Site occupancy	U_{iso}
Al	0.0	0.0	0.3521	1.0	0.0045
O	0.3062	0.0	0.25	1.0	0.0073

NIST SRM676a ZnO		a=3.2500 α=90°	b=3.2500 β=90°	c=5.2068 γ=120°	ICSD ref.157132 P 63 n c
Atom type	x coord.	y coord.	z coord.	Site occupancy	U_{iso}
Zn	0.3333	0.6667	-0.0018	1.0	0.0063
O	0.3333	0.6667	0.3784	1.0	0.0073

NIST SRM676a TiO_2		a=4.5937 α=90°	b=4.5937 β=90°	c=2.9586 γ=90°	ICSD ref.31322 P 42/m n m
Atom type	x coord.	y coord.	z coord.	Site occupancy	U_{iso}
Ti	0.0	0.0	0.0	1.0	0.0064
O	0.3040	0.3040	0.0	1.0	0.0091

NIST SRM676a Cr_2O_3		a=4.9591 α=90°	b=4.9591 β=90°	c=13.5970 γ=120°	ICSD ref.75577 R -3 c
Atom type	x coord.	y coord.	z coord.	Site occupancy	U_{iso}
Cr	0.0	0.0	0.3475	1.0	0.0001
O	0.3076	0.0	0.25	1.0	0.0063

Aldrich annealed α-Al_2O_3		a=4.7597 α=90°	b=4.7597 β=90°	c=12.9925 γ=120°	ICSD ref.51687 R-3c
Atom type	x coord.	y coord.	z coord.	Site occupancy	U_{iso}
Al	0.0	0.0	0.3521	1.0	0.0044
O	0.3074	0.0	0.25	1.0	0.0081

NIST SRM 640c Si		a=5.4338 α=90°	b=5.4338 β=90°	c=5.4338 γ=90°	ICSD ref.60389 F d -3 m
Atom type	x coord.	y coord.	z coord.	Site occupancy	U_{iso}
Si	0.125	0.125	0.125	1.0	0.0081

Industrial grade Zircon		a=6.6066 α=90°	b=6.6066 β=90°	c=5.9889 γ=90°	ICSD ref.15759 I 41/a m d
Atom type	x coord.	y coord.	z coord.	Site occupancy	U_{iso}
Zr	0.0	0.75	0.125	1.0	0.0035
Si	0.0	0.75	0.625	1.0	0.0022
O	0.0	0.0724	0.1978	1.0	0.0085

Table 5.9: Refined structure of all phases.

5.1.3 Figures

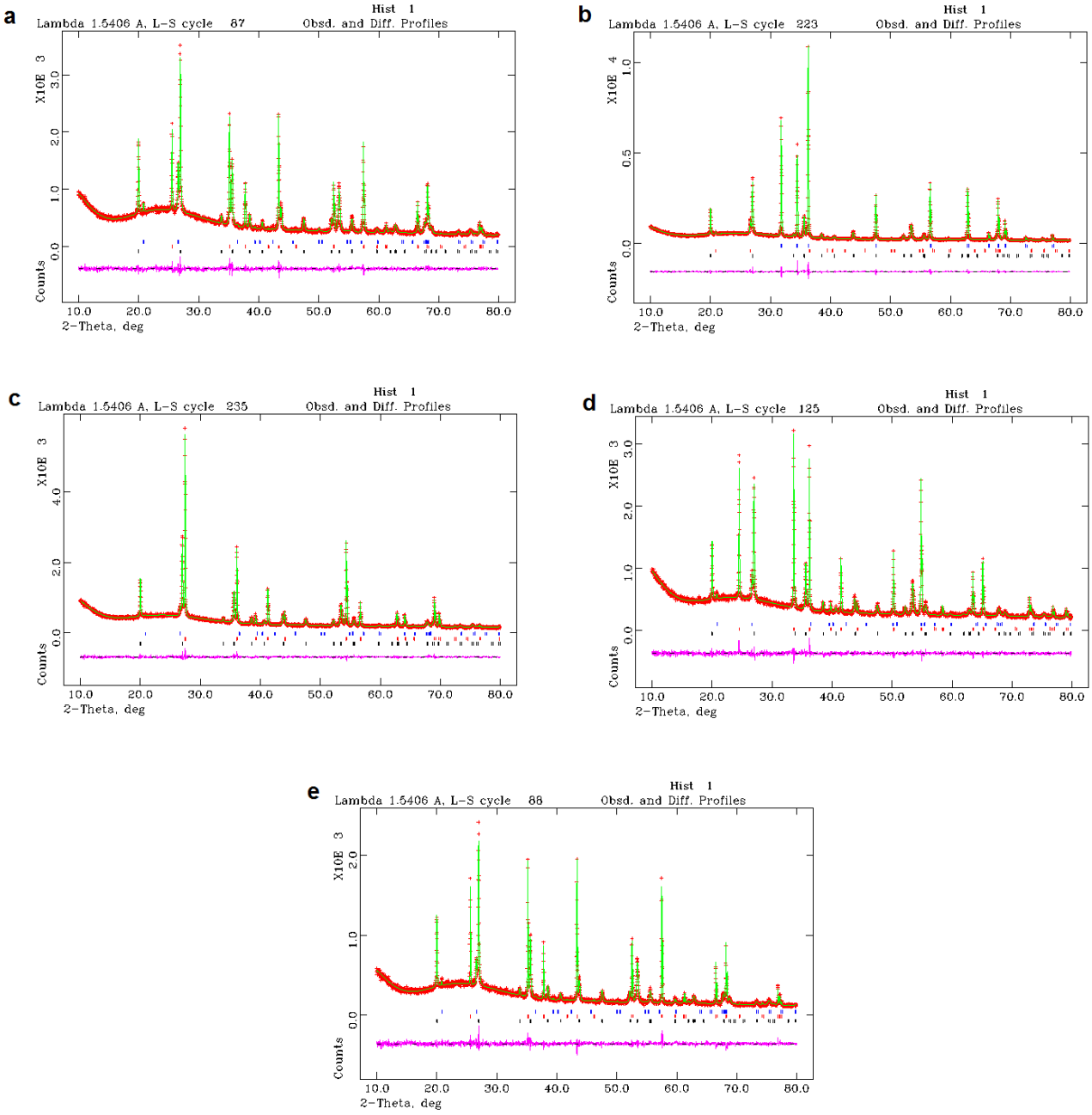

Figure 5.1: GSAS graphical fit of *adhoc* mixtures with different internal standard: NIST SRM 676a (a), NIST SRM 674a ZnO (b), NIST SRM 674a TiO_2 (c), NIST SRM 674a Cr_2O_3 (d), Aldrich annealed Al_2O_3 (e).

5.2 References

A. Abrami, F. Arfelli, R.C. Barroso, A. Bergamaschi, F. Billè, P. Bregant, F. Brizzi, K. Casarin, E. Castelli, V. Chenda, L. Dalla Palma, D. Dreossi, C. Fava, R. Longo, L. Mancini, R.H. Menk, F. Montanari, A. Olivo, S. Pani, A. Pillon, E. Quai, S. Ren Kaiser, L. Rigon, T. Rokvic, M. Tonutti, G. Tromba, A. Vascotto, C. Venanzi, F. Zanconati, A. Zanetti, F. Zanini (2005), "Medical applications of synchrotron radiation at the SYRMEP beamline of ELETTRA", *Nuclear Instruments and Methods in Physics Research A*, 548, 221-227.

R.J. Ackermann & C.A. Sorrell (1974), "Thermal expansion and the high-low transformation in quartz", *Journal of Applied Crystallography*, 7, 461-467.

F. Angeli, J. Delaye, T. Charpentier, J. Petit, D. Ghaleb & P.J. Faucon (2000), "Influence of glass chemical composition on the Na-O bond distance: a ^{23}Na 3Q-MAS NMR and molecular dynamics study", *Journal of Non-Crystalline Solids*, 276, 132-144.

G. Anger, J. Halstenberg, K. Hochgeschwender, C. Scherhag, U. Korallus, H. Knopf, P. Schmidt & M. Ohlinger (2005),"Chromium Compounds" in *Ullmann's Encyclopedia of Industrial Chemistry*, Wiley-WCH, Weinheim (Germany).

I.A. Aksay & C.H. Schilling (1984), "Mechanism of colloidal filtration" in "Advances in ceramics, Vol.9" edited by J.A. Mangels & G.L. Messing. American Ceramic Society, Columbus.

A. Assfaoui, W. Atmani, A. Daoudi, P. Moussa & P. Blanchart (2003), "Grain growth of zircon pigment in tile glaze", *British Ceramic Transactions*, 102, 57-60.

D.N. Batchelder & R.O. Simmons (1964), "Lattice Constants and Thermal Expansivities of Silicon and of Calcium Fluoride between 6 and 322 K", *Journal of Chemical Physics*, 41, 2324.

M. Benoit, M. Profeta, F. Mauri, C.J. Pickard & M.J. Tuckerman (2005), "First-principles calculation of the 17O NMR parameters of a calcium aluminosilicate glass", *Journal of Physical Chemistry B*, 109, 6052-6060.

L. Bergstrom (1994), "Rheology of concentrated suspension" in "Surface and colloid chemistry in advanced ceramic processing", edited by R.J. Pugh & L.Bergstrom. Marcel Dekker, New York.

D.L. Bish & S.A. Howard (1988), "Quantitative Phase Analysis Using the Rietveld Method", *Journal of Applied Crystallography*, 21, 86-91.

D.L. Bish & J.E. Post (1993), "Quantitative mineralogical analysis using the Rietveld full-pattern fitting method American Mineralogist", *American Mineralogist*, 78, 932-940.

D.L. Bish & R.C. Jr Reynolds (1989). "Sample preparation for X-ray diffraction", in "Modern Powder Diffraction", edited by D.L. Bish & J.E. Post. Reviews in Mineralogy and Chemistry, Vol.20. Mineralogical Society of America, USA, 73-99.

D.T. Bowron (2008), "An experimentally consistent atomistic structural model of silica glass", *Materials Science and Engineering B*, 149, 166-170.

G.W. Brindley (1945), "The Effect of Grain or Particle Size on X-ray Reflections from Mixed Powders and Alloys, considered in relation to the Quantitative Determination of Crystalline Substances by X-ray Methods", *Philophical Magazine*, 36, 347-369.

G.W. Brindley & M. Nakahira (1959), "The Kaolinite-Mullite Reaction Series: II, Metakaolin", *Journal of the American Ceramic Society*, 42 [7], 314-318.

W.L. Brown & I. Parsons (1989), "Alkali feldspars: ordering rates, phase transformations and behaviour diagrams for igneous rocks", *Mineralogical Magazine*, 53, 25-42.

W.M. Carty & Senapati U (1998), "Porcelain: raw materials, processing, phase evolution and mechanical behaviour", *Journal of the American Ceramic Society*, 81, 3-20.

R.J. Castilone, D. Sriram, W.M. Carty & R.L. Snyder (1999), "Crystallisation of zircon in stoneware glazes", *Journal of the American Ceramic Society*, 82 (19), 2819-2824.

S.J. Chipera & D.L. Bish (2002), "FULLPAT: a full-pattern quantitative analysis program for X-ray powder diffraction using measured and calculated patterns", *Journal of Applied Crystallography*, 35, 744-749.

F.H. Chung (1974), "Quantitative interpretation of X-ray diffraction patterns of mixture. I. Matrix-flushing method for quantitative multicomponent analysis", *Journal of Applied Crystallography*, 7, 519-525.

J.P. Cline, R.P. Von Dreele, R. Winburn, P.W. Stephens & J.J. Filliben (2011), "Addressing the amorphous content issue in quantitative phase analysis: the certification of NIST standard reference material 676a", *Acta Crystallographica*, A67, 357-367.

A. Cormack & J. Du (2001), "Molecular dynamics simulations of soda-lime-silicate glasses", *Journal of Non-Crystalline Solids*, 293-295, 283-289.

L. Cormier, D. Ghaleb, D.R. Neuville, J. Delaye & G.J. Calas (2003), "Chemical dependence of network topology of calcium aluminosilicate glasses: a computer simulation study", *Journal of Non-Crystalline Solids*, 332, 255-270.

L. Cormier & D.R. Neuville (2004), "Ca and Na environments in Na_2O-CaO-$Al_2O_3$3-SiO_2 glasses: influence of cation mixing and cation-network interactions", *Chemical Geology*, 213, 103-113.

L. Cormier, D.R. Neuville & G.J. Calas (2005), "Relationship Between Structure and Glass Transition Temperature in Low-silica Calcium Aluminosilicate Glasses: the Origin of the Anomaly at Low Silica Content", *Journal of the American Ceramic Society*, 88, 2292-2299.

A.G. De la Torre, S. Bruque & M.A. Aranda, M.A. (2001), "Rietveld quantitative amorphous content analysis", *Journal of Applied Crystallography*, 34, 196-202.

P.M. De Wolff (1956), "Measurement of particle absorption by X-ray fluorescence", *Acta Crystallographica*, 9, 682-683.

R.E. Dinnebier & S.J.L. Billinge (2008), "Powder Diffraction: Theory and Practice", RSC, Cambridge.

W.A. Dollase (1965), "Reinvestigation of the structure of low cristobalite", *Zeitschrift für Kristallographie*, 121 (5), 369-377.

M. Dondi, G. Guarini & I. Venturi, "Assessing the fusibility of feldspathic fluxes for ceramic tiles by hot stage microscope", *Industrial Ceramics*, 21, 67-73.

L.S. Dubrovinskii & YU.Z. Nozik (1989), "Calculation of Anisotropic Heat Parameters of alpha-Quartz Atoms", *Doklady Akademii Nauk*, 306, 1384-1386.

R.O. Duda, P.E. Hart & D.G. Stork (2001), "Pattern Classification", second edition, John Wiley & Sons, New York.

A. Escardino (2001), "Kinetic Model for Crystallization in White Ceramic Glazes", *Journal of the American Ceramic Society*, 84 (1), 23-28.

Y. Fei (1995), "Thermal expansion" in "Mineral physics and crystallography: a handbook of physical constants, Vol. 2" edited by T.J. Ahrens. AGU, Washington DC.

A.N. Fitch (2004), "The High Resolution Powder Diffraction Beam Line at ESRF", *J. Res. Natl Inst. Stand. Technol.*, 109, 133-142.

A. Fluegel (2010), "Thermal Expansion Calculation of Silicate Glasses at 210°C, Based on the Systematic Analysis of Global Databases", *European Journal of Glass Science and Technology*, 51 (5), 191-201.

L. Froberg, T. Kronberg, L. Hupa & M. Hupa (2007), "Influence of firing parameters on phase composition of raw glazes", *Journal of the European Ceramic Society*, 27, 1671-1675.

D. Giordano, J.K. Russell & D.B. Dingwell (2008), "Viscosity of magmatic liquids: a model", *Earth and*

Planetary Science Letters, 271, 123-134.

W. Gonschorek & R. Feld (1982), "Neutron diffraction study of the thermal and oxygen position parameters in rutile", *Zeitschrift für Kristallographie* , 161, 1-5.

G.J. Greaves (1985), "EXAFS and the structure of glass", *Journal of Non-Crystalline Solids*, 71, 203-217.

A.F. Gualtieri (2000), "Accuracy of XRPD-QPA using the combined Rietveld-RIR method", *Journal of Applied Crystallography*, 33, 267-278.

A.F. Gualtieri & M. Bellotto (1998), "Modelling the structure of the metastable phases in the reaction sequence kaolinite-mullite by X-ray scattering experiments", *Physics and Chemistry of Minerals*, 25[6], 442-452.

A.F. Gualtieri, A. Guagliardi & A. Iseppi (2004), "The quantitative determination of the crystalline and amorphous content by the Rietveld method: application to glass ceramics with different absorption coefficients" in "Diffraction Analysis of the Microstructure of Materials. Vol.68" Springer, 147-165.

H. Hermann & M. Ermrich (1987), "Microabsorption of X-ray Intensity in Randomly Packed Powder Specimens", *Acta Crystallographica*, A43, 401-405.

R.J. Hill (1992), "Rietveld refinement round robin. I. Analysis of standard X-ray and neutron data for $PbSO_4$" *Journal of Applied Crystallography*, 25, 589-610.

R.J. Hill & C.J.Howard (1987), "Quantitative Phase Analysis from Neutron Powder Diffraction Data Using the Rietveld Method", *Journal of Applied Crystallography*, 20, 467-474.

J. Kabel, A. Odgaard, B. Rietbergen & R. Huiskes (1999), "Connectivity and the elastic properties of cancellous bone", *Bone*, 24, 115-120.

H.P. Klug & L.E. Alexander (1974), "X-Ray Diffraction Procedures: For Polycrystalline and Amorphous Materials", Wiley-VCH, New York.

W. Konijnendijk & J. Stevels (1976), "The linear expansion of borosilicate glasses in relation to their structure", *Verres et Refractaires*, 30 (3), 371-377.

Y. Iqbal, W.E. Lee (2000), "Microstructural evolution in triaxial porcelain", *Journal of the American Ceramic Society*, 83, 3121-3127.

A.C. Larson & R.B. Von Dreele (2004), "General Structure Analysis System (GSAS)", LAUR, Los Alamos Natl. Lab. Rep., 86-748.

W.E. Lee, G.P. Souza, C.J. McConville, P. Tarvornpanich & Y. Iqbal Y. (2008), "Mullite formation in clays and clay-derived vitreous ceramics", *Journal of the European Ceramic Society*, 28, 465-471.

A.Y. Leinekugel-le-Cocq-Errien, P. Deniard, S. Jobic, E. Gautier, M. Evain, V. Aubin & F. Bart (2007), "Structural characterization of the hollandite host lattice for the confinement of radioactive cesium: Quantification of the amorphous phase taking into account the incommensurate modulated character of the crystallized part", *Journal of Solid State Chemistry*, 180, 322-330.

R. Loewenstein & G. Wilk (1954), "The distribution of aluminum in the tetrahedra of silicates and aluminates" *American Mineralogist*, 39, 92-96.

L. Mancini, E. Reinier, P. Cloetens, J. Gastaldi, J. Hartwig, M. Schlenker & J. Baruchel J (1988), "Investigation of structural defects and inhomogeneities in Al-Pd-Mn icosahedral quasicrystals by combined synchrotron X-ray topography and phase radiography", *Philosophical Magazine*, 78 (10), 1175-1194.

J. Martin-Marquez, A.G. De la Torre, M.A.G. Aranda, J.M. Rincon & M. Romero (2009), "Evolution with temperature of crystalline and amorphous phases in porcelain stoneware", *Journal of the American Ceramic Society*, 92 [1], 229-234.

J. Martin-Marquez, J.M. Rincòn & M. Romero (2010), "Mullite development on firing in porcelain stoneware bodies", *Journal of the European Ceramic Society*, 30, 1599-1607.

L.B. McCusker, R.B. Von Dreele, D.E. Cox, D. Louer & P. Scardi (1999), "Rietveld refinement guidelines", *Journal of Applied Crystallography*, 32, 36-50.

M. Moroz, G.N. Maslennikova, A.F. Mironova & Y.P. Platov (1980), "Formation of tridymite and cristobalite from quartz in porcelain" in "Glass and ceramic, Vol. 37, Springer, 147-50.

X. Orlhac, C. Fillet, P. Deniard, A.M. Dulac & R. Brec (2001), "Determination of the crystallized fractions of a largely amorphous multiphase material by the Rietveld method", *Journal of Applied Crystallography*, 34, 114-118.

M. Paganelli (1999), "Understanding the behaviour of glazes: new test possibilities using the automatic hot stage microscope "Misura"", *Industrial Ceramics*, 17, 69-73.

A. Pagani, F. Francescon , A. Pavese & V. Diella, "Sanitary-ware vitreous body characterization method by optical microscopy, elemental maps, image processing and X-ray powder diffraction", *Journal of the European Ceramic Society*, 30, 1267-1275.

P.H. Ribbe, H.D. Megaw, W.H. Taylor, R.B. Ferguson & R.J. Traill (1969), "The albite tructures", *Acta Crystallographica, Section B*, 25, 1503-1518.

H.M. Rietveld (1969), "A Profile Refinement Method for Nuclear and Magnetic Structures", *Journal of Applied Crystallography*, 2, 65-71.

A.P. Reifenstein, H. Kahraman, C.D.A. Coin, N.J. Calos, G. Miller & P. Uwins (1999), "Behaviour of selected minerals in an improved ash fusion test: quartz, potassium feldspar, sodium feldspar, kaolinite, illite, calcite, dolomite, siderite, pyrite and apatite", *Fuel*, 78, 1449-1461.

K. Robinson, G.V. Gibbs & P.H. Ribbe (1971), "The structure of zircon: a comparison with garnet", *American Mineralogist*, 56, 782-790.

H. Rozale, L. Beldi, B. Bouhafs & P. Ruterana (2007), "A theoretical investigation of $ZnO_xS_{(1-x)}$ alloy band structure", *Physica Status Solidi B*, 244 (5), 1560-1566.

H. Saalfeld, W. Guse (1981), "Structure refinement of 3:2 mullite (3 Al_2O_3 - 2 SiO_2)", *Neues Jahrbuch fur Mineralogie*, 145-150.

T.M. Sabine, R.B. Von Dreele & J.E. Jorgensen (1988), "Extinction in Time-of-Flight Neutron Powder Diffractometry", *Acta Crystallographica*, A44, 374-379.

H. Sawada (1984), "Residual electron density study of chromium sesquioxide by crystal structure and scattering factor refinement", *Materials Reasearch Bulletin*, 29(3), 239-245.

D. Sivia (2011), "Elementary Scattering Theory for X-ray and Neutron Users", edited by Oxford University Press, Oxford.

A. K. Soper (2005), "Partial structure factors from disordered materials diffraction data: An approach using empirical potential structure refinement", *Physical Review B*, 72, 104204.

A. K. Soper (2009), "Inelasticity corrections for time-of-flight and fixed wavelength neutron diffraction experiments", *Molecular Physics*, 107 (16), 1667-1684

A.K. Soper (2010a), "GudrunN and GudrunX: Programs for Correcting Raw Neutron and X-ray Diffraction Data to Differential Scattering Cross Section", edited by ISIS Disordered Material Group, Didcot (UK).

A.K. Soper (2010b), "EPSRshell: A User's Guide", edited by ISIS Disordered Material Group, Didcot (UK).

J. Smith & S. Bailey (1963), "Second review of Al-O and Si-O tetrahedral distances", *Acta Crystallographica*, 16, 801-811.

G. Stathis, A. Ekonomakou, C.J. Stournaras & C. Ftikos (2004), "Effect of firing conditions, filler grain size and quartz content on bending strength and physical properties of sanitaryware porcelain", *Journal of the European Ceramic Society*, 24, 2357-2366.

F.H. Stillinger FH (1988), "Supercooled liquids, glass transitions, and the Kauzmann paradox", *Journal of*

Chemical Physics, 88, 7818-7825.

P. Suortti (1972), "Effects of Porosity and Surface Roughness on the X-ray Intensity Reflected from a Powder Specimen", *Journal of Applied Crystallography*, 5, 325-331.

T. Suzuki-Muresan, P. Deniard, E. Gautron, V. Petricek, S. Jobic & B. Grambow, B (2010), "Minimization of absorption contrast for accurate amorphous phase quantification: application to ZrO_2 nanoparticles", *Journal of Applied Crystallography*, 43, 1092-1099.

T. Tarvornpanich, G. P. Souza & W. E. Lee (2005), "Microstructural Evolution on Firing Soda-Lime-Silica Glass Fluxed Whitewares", *Journal of the American Ceramic Society*, 88 [5], 1302-1308.

T. Tarvornpanich, G. P. Souza & W. E. Lee (2005), "Microstructural evolution in clay-based ceramics I: single components and binary mixtures of clay, flux, and quartz filler", *Journal of the American Ceramic Society*, 91 [7], 2264-2271.

T. Tarvornpanich, G. P. Souza & W. E. Lee (2005), "Microstructural Evolution in clay-based ceramics II: ternary and quaternary mixtures of clay, flux, and quart filler", *Journal of the American Ceramic Society*, 91 [7], 2272-2280.

J.C. Taylor & C.E. Matulis (1991), "Absorption Contrast Effect in the Quantitative XRD Analysis of Powders by Full Multiphase Profile Refinement", *Journal of Applied Crystallography*, 24, 14-17.

B.H. Toby (2001), "EXPGUI, a graphical user interface for GSAS", *Journal of Applied Crystallography*, 34, 210-213.

D.M. Toebbens, N. Stuesser, K. Knorr, H.M. Mayer & G. Lampert (2001), *Material Science Forum*, 378, 288Ű293.

M. Toplis, D. Dingwell & T. Lenci (1997), "Peraluminous viscosity maxima in Na_2O-Al_20_33-SiO_2 liquids: The role of triclusters in tectosilicate melts", *Geochimica et Cosmochimica Acta*, 61, 2605-2612.

J.W. Visser & P.M. De Wolff (1964), "Report N.641.109", Technisch Physische Dienst, Delft (Netherlands).

L.S. Zevin & G. Kimmel (1995), "Quantitative X-ray Diffractometry", Springer, New York.

N. Zotov & H. Keppler (1998), "The structure of sodium tetrasilicate glass from neutron diffraction, reverse Monte Carlo simulations and Raman spectroscopy", *Physical Chemistry of Minerals*, 25, 259-267.

R. Wallace & G. Wilk (2003), "High-k Dielectric Materials for Microelectronics", *Critical Reviews in Solid State and Materials Sciences*, 28 (4), 231-285.

Acknowledgments

I would like to thank all my family, which sustained and encouraged me during my scholastic and universitary walk, and also Romia, which gave me comprehension and quiet.
Many thanks to my supervisor Monica for helping me during this "PhD adventure", always.
Thanks to all the others scientific and human contributes of the University of Milan; first of all to Alessandro and then to Nicoletta, Valeria, Andrea, and Elena. And finally, many thanks to scientific contributions of Prof. Gualtieri and Dr. Daniel Bowron.